A BALANCE POINT APPROACH TO MODELING HEMODYNAMICS IN CHRONIC HEART FAILURE

A Dissertation

by

SARAH FUSAYO COQUIS-KNEZEK

Submitted to the Office of Graduate and Professional Studies of
Texas A&M University
in partial fulfillment of the requirements for the degree of

DOCTOR OF PHILOSOPHY

Chair of Committee,	Christopher Quick
Committee Members,	Randolph Stewart
	Ranjeet Dongaonkar
	John Criscione
Head of Department,	Larry Suva

December 2016

Major Subject: Biomedical Sciences

ABSTRACT

Chronic heart failure is a complex disease state that can yield reduced cardiac output, pulmonary edema, and increased peripheral resistance. Pressures, flows, and volumes in these conditions emerge from the complex interaction of multiple mechanical properties of the cardiovascular system. The shear complexity of emergent behavior poses a challenge to both basic scientists, who use reductionist approaches to study subsystems in isolation, and clinical researchers, who use inductive approaches to infer the causes of observed changes in clinical variables. This dissertation instead takes a deductive approach using mathematical models to relate three critical cardiovascular variables impacted by heart failure (cardiac output, pulmonary interstitial pressure, and microvascular resistance) to mechanical properties of three subsystems of the cardiovascular system. In contrast to common modeling approaches, three strategies are employed to reduce the complexity and generalize results. First, systems are strategically lumped into descriptions that can be characterized empirically. Second, algebraic formulas are derived to generalize results. Third, the critical interaction of physiological subsystems is represented with opposing processes in the form of "balance points."

The use of all three strategies allows us to: 1) quantify Guyton's classic cardiac output-venous return graph, 2) predict pulmonary interstitial pressure from interaction of the heart, vascular, and lymphatic systems, and 3) characterize adaptation of the microvasculature to changes in pulsatile blood flow. Cardiac output and venous return curves can now be predicted from parameters characterizing the mechanical properties

of the closed-loop system with chronic heart failure. The primary determinants of pulmonary interstitial pressure can now be identified for different phenotypes of heart failure. Finally, increased peripheral resistance, capillary rarefaction, and the formation of arteriovenous malformations are predicted with a decrease in the pulsatility of blood flow. Taken together, applying a physiological balance point approach to integrate subsystems clarifies how changes in the mechanical properties of the cardiovascular system impacts blood and interstitial pressures, volumes, and flows.

ACKNOWLEDGEMENTS

I would like to thank my committee chair, Dr. Quick, and my committee members, Dr. Criscione, Dr. Dongaonkar, and Dr. Stewart for their guidance and support throughout the course of this research.

Finally, thanks to my mother and father for their encouragement and to my husband for his patience and love.

CONTRIBUTORS AND FUNDING SOURCES

Contributors

This work was supervised by a dissertation committee consisting of Dr. Christopher Quick (advisor), Dr. Randolph Stewart, and Dr. Ranjeet Dongaonkar of the Department of Veterinary Physiology and Pharmacology and Dr. John Criscione of the Department of Biomedical Engineering.

All work conducted for the dissertation was completed by the student independently.

Funding Sources

This work was made possible in part by American Heart Association under Grant Number 10GRNT4320043 and the National Science Foundation under Grant Number CMMI-1063954. Its contents are solely the responsibility of the authors and do not necessarily represent the official views of the American Heart Association or the National Science Foundation.

TABLE OF CONTENTS

Page

LIST OF FIGURES

Page

LIST OF TABLES

Page

1. INTRODUCTION

Blood and interstitial pressures, volumes and flows arise from the interaction of mechanical components: pumps, chambers, and resistances. Although the interstitial and blood compartments differ in function, they arise from the same mechanical forces. The hemodynamics of the cardiovascular and interstitial system can be represented by the same relationships between pressure and flow. Each component in the system can be expressed as a mechanical equivalent, with vessels represented by a lumped resistance, chambers represented with a compliant pressure-volume relationship, and the heart as a pump. Expressed in a circuit as their electrical analogue components of a resistor, capacitor, and variable capacitor, compliance, pressures, flows, and volumes can be found for each component (237). Arranged as a simplified lumped system, fluid is exchanged between cardiovascular compartments with three flows: lymphatic flow, cardiac output, and microvascular flow.

Understanding of the complexity in chronic heart failure hemodynamics remains limited. Despite significant therapeutic advances, outcomes for heart failure patients remain sub-optimal (64, 219). One issue gaining significant traction is that a one-size-fits-all approach to heart failure management is not likely to be beneficial to most patients (64). It is now common to split heart failure patients into preserved and reduced ejection fraction cohorts when applying treatment protocols (24, 250). However, with numerous other underlying disorders (64), it is crucial to develop a generalized understanding of the cardiovascular properties regulating cardiac output and pressures.

Pulmonary hypertension, affecting from 25 to >50% of heart failure patients (76), may prove to be a crucial disorder to target. Clinical trials are currently underway to determine whether reducing pulmonary vascular resistance and pulmonary arterial pressure long term will help improve outcomes with heart failure (116). In addition, relating pulmonary hypertension to pulmonary congestion can be difficult, because even with invasive catheterization pressures can only indirectly suggest what pulmonary interstitial pressure and flows are (248). Therefore, an understanding of the basic mechanical mechanisms underlying the relationship of capillary and interstitial pressures and volumes to cardiac function may be helpful not only in determining phenotypes but also to suggest key variables to target.

Cardiac output is governed by complex interactions of the ventricles with the vasculature. The complexity of the interaction of cardiac output with the peripheral circulation led Guyton to run a series of experiments trying to isolate the role of the venous circulation in cardiac output (81). His analysis of the complaint-chamber experimental model produced a linear algebraic model of the relationship between cardiac function and the peripheral circulation. To enable understanding of cardiac output, Guyton introduced the cardiac output-venous return balance point, a simple analytical description of the balance of cardiac output and venous return. Commonly used to describe and teach hemodynamics with hemorrhage and heart failure (27, 126), Guyton's model led to the conclusion that right atrial pressure represents an impedance to flow from the systemic circulation (14). In Guyton's model, mean systemic filling pressure is the driving force behind pump flow. Composed of the ratio of systemic blood

volume to systemic compliance of the vascular chambers, studies have suggested that this holds true in normal cases (104, 145, 278). However, addition or removal of volume to the blood compartment does not determine the amount of fluid that will stay in the blood volume (156). Other variables are regulated, such as systemic arterial pressure or extracellular water, depending on the time scale. Guyton's work assumes that systemic blood volume is constant, while mean systemic filling pressure is the variable (14). Therefore, Guyton's description holds only while blood volume is well regulated.

Illustrative Problem 1: Quantifying Guyton's cardiac output-venous return when pressures are chronically regulated. Guyton's balance point is used as a description of heart failure (102) and in clinical discussions of cardiac output (147). However, Guyton's model includes only the systemic side of the circulation, excluding any interaction with the pulmonary system. Clinically, pulmonary hypertension is a common complication of heart failure (76), but although significant advances have been made (116), pulmonary hypertension can be difficult to measure without invasive procedures. In addition, Guyton's model allows systemic arterial pressure to vary, while chronically, systemic arterial pressure is regulated within a narrow range of values (213). Instead, blood volume, while constant under normal conditions, changes drastically with heart failure, sometimes as much as 30% (4). Hypervolemia in chronic heart failure is typically treated with diuretics; however, removal of fluid from blood volume is difficult to predict long term as volumes redistribute (156). Although others have solved venous return for the pulmonary system to solve this problem (256), the systems were not

integrated. Therefore, we need to couple the pulmonary and systemic spaces to understand how vascular properties affect cardiac output during volume shifts.

The interactions governing interstitial flow are complex. Knowledge of the fundamental properties governing flux in and out of the blood vascular compartment is necessary but not sufficient to explain changes in blood pressure and flows. The Starling-Landis equation characterizes the flux of water into the interstitial compartment from the blood compartment with a limited set of properties—the water and protein permeabilities as well as oncotic and hydrostatic pressure differences (289). Flux of water out of the interstitial compartment into the blood compartment is characterized by an even more compact set of properties. The Drake-Laine equation relates flux from the interstitial compartment to an "effective lymphatic resistance" and "effective pump pressure" and hydrostatic pressure differences (130). These two equations provide insight: for example, an increase in the microvascular filtration coefficient due to inflammation will increase flux into the interstitium, partially explaining edema. However, increased volume is ameliorated by increased lymphatic function. Experimentally quantifying the effect of the microvascular filtration coefficient on edema becomes difficult when you consider inflammatory factors also affect lymphatic function (138). Further complicating measurements, flux between compartments not only depends on capillary and venous pressures, but also helps regulate these pressures (289). In addition, capillary and venous pressures arise from the interaction of cardiac function, microvascular resistances, and venous capacitances. Because hydrostatic pressures are both a cause and effect of fluxes, blood and interstitial volumes arise from

the complex interaction of the blood and interstitial compartments. In normal physiological conditions, both capillary pressure (228) (the inlet to the interstitial spaces) and systemic venous pressure (146) (the outlet from the interstitial spaces) are fairly well regulated. Therefore, these compartments are generally functionally uncoupled.

Illustrative Problem 2: Predicting the determinants of pulmonary interstitial pressures with heart failure. During any condition where large amounts of volume are lost or gained from the blood volume, the interstitial and vascular spaces become tightly linked as volume moves from one space to another (228). For example, during heart failure, blood volume increases as blood pressures are maintained at normal levels (156). While normally a tightly regulated system, the increase in volume means that small changes in cardiac function may have an effect on interstitial pressures. Thus, cardiac function may now directly affect pulmonary interstitial pressures, and through that, pulmonary edema. However, the effect of cardiac function on forces such as lymph flow and pulmonary interstitial pressure remains unquantified.

Complex interactions govern microvascular flow. Because the microvasculature is the site of most hemodynamic resistance, it plays a vital role in controlling blood supply to the tissues as well as regulating blood pressures and cardiac output. Both the pulmonary and systemic microvasculatures play a large role in blood pressure and flow regulation. On one hand, microvascular resistance is governed by the complex parallel and series arrangement of vessels, each with its own diameter. Small changes in diameter in any one vessel redistribute both pressure and flow throughout the network. Microvascular physiologists have focused on experimental set-ups to explain the

interaction of vessel forces leading to adaptation (163, 251). Mechanobiologists have focused on explaining how the forces' effect on the vessel wall sets the diameter of a single vessel (3, 143). More recently, investigators have tried to combine approaches by using computational biomechanical models based on realistic structures to demonstrate network hemodynamics (193, 202). However, most studied only steady flow (200, 293), and because of experimental limitations, few chronic studies isolate the effect of mechanical variables (275). In addition, many computational models assume a set equilibrium point for vessel adaptation (117, 200), which has limited physiological basis (173). The interaction of mechanical forces in the microvasculature, already complex with steady flow, becomes even more complicated with the addition of adaptation to pulsatile flows and pressures.

Illustrative Problem 3: Response of arteriolar networks to decreased pulsatility commonly seen in heart failure. Although originally thought to be exposed only to steady-flow, significant pulsatility reaches the microvessels (67, 133). In addition, measurements of both the systemic and pulmonary microcirculation have shown that pulsatility transmits through the microvasculature and reaches the venous side, although at fairly small levels (233, 240). A decrease in the stroke volume reaching the microvessels alters conditions to which the vessels respond. Experiments have shown that vessels respond differently to pulsatile and steady endothelial shear stress (103, 293). Chronic exposure to decreased pulsatility, such as can be seen with heart failure (294), leads to several clinical side effects, which most notably include increased

microvascular resistance (166). The lack of integration of the effect of pulsatile cardiac output on microvascular resistance has led to a lack of knowledge about their interaction.

Conventional animal and comprehensive computational models are similar in that they yield complex, model-dependent results. Animal models allow replication of complex disease states under controlled conditions, measurement of important variables and testing of potential clinical interventions (274). However, investigators report that results from animal models are animal-specific (273), impacted by measurement techniques (274), and sensitive to the method of inducing volume shifts (162). With the inability to reliably measure critical variables (248) or selectively control interacting compensatory mechanisms (274), investigators have resorted to mathematical models. Although based on established principles such as conservation of mass and conservation of momentum, computational models nonetheless require assumption of specific parameter values that are either poorly known (248) or known to vary significantly from patient to patient (148, 221). More importantly, mathematical models that reproduce the complexity of the cardiovascular system, such as the seminal model by Guyton et al. (85), are notoriously difficult to interpret (102), let alone identify errors (122). In an effort to enhance understanding and reduce the need for curve-fitting unknown parameters, investigators have simplified models to two or three compartments (blood, interstitial, and intracellular) to understand the interaction (59, 94, 196, 220, 224). However, most models still rely on computational approaches (i.e., numerical solutions), and thus are limited in the insights they may provide. Taken together, mathematical

models of pressures and flows in the vascular system have heretofore failed to reduce the complexity of the system and generalize results.

Simplifying approach 1: Algebraic solutions. General algebraic models allow general predictions of volumes, pressures and flows. Prior to increased computational power that allowed quick assembly of complex models, algebraic approaches were ubiquitous (196). These deductive, predictive models had great promise. Analytical solutions provide a formula that explicitly relates the parameters characterizing subsystems to predicted variables of interest that arise from their interaction. Sunagawa's analytical solution to the interaction of the left ventricle with the systemic arterial system, for instance, not only provides the means to predict cardiac output (256), but also allows cardiac output to be attributed to particular mechanisms. Focused on understandability and simplicity rather than the accuracy of results, this model was able to develop indices of ventricular-arterial coupling that are expressed in terms of vascular and ventricular mechanical properties. By focusing on simplicity, they were able to reduce complexity. However, the use of analytical solutions of entire cardiovascular systems is exceedingly rare (257).

Simplifying approach 2: Graphical balance points. Graphical balance points allow prediction of the interaction of two parts of a system. Guyton characterizes cardiac output with the balance of cardiac function and venous return. By separating cardiac output into two opposing flows of cardiac function and venous return, the concept becomes easier to understand and apply. Placing the two forces in a graphical format, a simple analytical description is able to describe the slope and intercept of the two lines,

and thus easily be extended to explaining how the equilibrium, or the intersection of the two lines, changes with a change in any variable (88). Similarly, Dongaonkar applied the balance point concept to explain interstitial pressures and flows. As a balance of microvascular filtration and lymphatic return, it allows a simple explanation of forces in the interstitial space as ‘effective driving pressures’ and ‘effective resistances’, corresponding to the intercept and slope of each line (49). By representing forces as a balance point, the complexity of each part becomes easier to conceptualize and understanding of how equilibrium emerges becomes clearer.

2. CHRONIC CARDIAC OUTPUT-VENOUS RETURN BALANCE POINT

2.1 Background

Although Guyton's classic cardiac output-venous return graph describes the interaction of the heart and the systemic vasculature, it remains a conceptual model. Using an experimental preparation that included the heart and the pulmonary vasculature, Ernest Starling reported a dramatic increase in cardiac output from the heart with an increase in right atrial pressure (246). Challenging the resulting belief that the heart controlled cardiac output (118), Guyton et al. devised a complementary experiment to illustrate that the venous return from the systemic circulation decreases with increases in right atrial pressure (89). Assuming conservation of mass, simultaneously graphing cardiac output and venous return curves with respect to right atrial pressure reveals a balance point where cardiac output is equal to venous return (81). This conceptual tool helped establish the central role of the metabolic demand of tissues in controlling cardiac output (12, 18, 95). Perhaps as important, Guyton explained observed changes in cardiac output and right atrial pressure with such diverse states as hypertension (87), hemorrhage (90) and chronic heart failure (87) by manipulating the slopes and intercepts of cardiac output and venous return curves. Furthermore, Guyton et al. (89) developed a mathematical model that predicted how the mechanical properties of the systemic circulation affect the slope and intercept of the venous return curve. As a result, an increase in the "systemic filling pressure" (i.e., the zero-flow intercept of the venous return curve), is commonly invoked to explain compensation to chronic heart failure (18,

102, 214). There have since been vigorous debates about the interpretation (14, 26) and physiological relevance (51, 102, 214) of Guyton's original characterization of venous return because regulatory mechanisms were abolished and systemic blood volume was held constant. Nonetheless, Guyton's classical graph is commonly used in systemic physiology textbooks, because it provides a simple means to conceptualize the complex interaction of cardiac output and venous return (18, 95). Its use in the scientific literature has been limited, because changes in the cardiac output curve must be assumed, rather than predicted from changes in the mechanical properties of the heart.

Although the standard "minimal closed-loop model" quantitatively predicts hemodynamic variables from mechanical properties of the entire cardiovascular system, numerical solutions lack generality. The difficulty inferring mechanical properties responsible for changes in cardiac output and blood pressures has led investigators to develop predictive mathematical models (232). For instance, the very large comprehensive model developed by Guyton et al. (86) yielded the critical insight that renal control of blood volume was the primary mechanism that regulates systemic blood pressure chronically (82). Such large-scale models have given way to more modest approaches that limit the number of assumptions necessary to predict critical hemodynamic variables (237). The "minimal closed-loop model" in particular is notable, because it reduces complexity of the cardiovascular system into eight elements: two peripheral resistances, four vascular compartments, and two ventricles (99, 191). Nonetheless, it requires at least 16 parameters to characterize the mechanical properties, some of which have never been measured in humans (223) or are notoriously difficult to

measure (222). Although the equations characterizing the lumped elements are almost universally assumed to be linear, diastolic ventricular volume is typically assumed to be a nonlinear function of filling pressure (121). This single complexity requires the entire system of model equations to be solved numerically. Such numerical solutions lack generality, because predicting a single value of a variable such as cardiac output requires values for each of the 16 parameters to be assumed *a priori*. Although it is possible to graph cardiac output as a function of one parameter such as left ventricular end-systolic elastance, the resulting plot depends on particular values of the other assumed parameters (139). The number of parameter values increases with addition of explicit feedback mechanisms that characterize regulation of systemic arterial pressure (187, 270).

Although Sunagawa's algebraic solution to the minimal closed-loop model is general, it does not assume regulation of systemic arterial pressure. To overcome the inherent limitations of numerical solutions, Sunagawa and colleagues developed two seminal cardiovascular models that had algebraic solutions. First, they coupled the classic time-varying elastance model of the left ventricle (238) to a Windkessel model of the systemic arterial system. The result was a general algebraic formula for cardiac output in terms of cardiac and arterial system parameters (256). This simple formula included a ratio of "effective arterial elastance" and end-systolic ventricular elastance, which has become a critical characterization of arterio-ventricular coupling with heart failure (128). Second, they linearized the equation characterizing the ventricles in diastole, and solved the model equations of the minimal closed-loop model. The

resulting general formulas characterized cardiac output and blood pressures in terms of mechanical properties of the closed-loop system (256). Although this model was experimentally validated (255, 269), this powerful approach is limited in its ability to characterize chronic conditions, because blood volume was assumed to be a constant parameter, and systemic blood pressure was treated as a predicted variable. Therefore, the purpose of the present work is to develop general algebraic formulas that predict the interaction of cardiac output and venous return when systemic arterial pressure is chronically regulated.

2.2 Methods

Characterizing the components of the minimal closed-loop model with linear equations. Figure 1 illustrates three components of the minimal closed-loop model. Relationships between the variables of interest are assumed to be linear, as is commonly assumed for most minimal closed-loop models (99, 191, 270). Cardiac output (CO) through the peripheral vasculature is a function of the arterial-venous pressure difference (P_a-P_v), and depends on the vascular resistance (R). The cardiac ventricles are described by a time-varying elastance (254). The ventricular end-systolic pressure (P_{es}) and end-diastolic pressure (P_{ed}) both are functions of ventricular volume. The end-systolic pressure-volume relationship depends on the maximum ventricular elastance (E_{max}) and the ventricular unstressed volume in systole (V_{oes}). Although the end-diastolic pressure-volume relationship is often characterized as nonlinear (137, 191) (see *Appendix B*), it is treated in the present work as linear. End-diastolic volume, therefore, depends on the

minimum ventricular elastance (E_{min}) and the ventricular unstressed volume in diastole (V_{oed}). Blood volume (V) stored in a vascular compartment is a function of transmural pressure (P), and depends on the compliance of the compartment (C) and its unstressed volume (V_o), i.e. the volume at zero pressure.

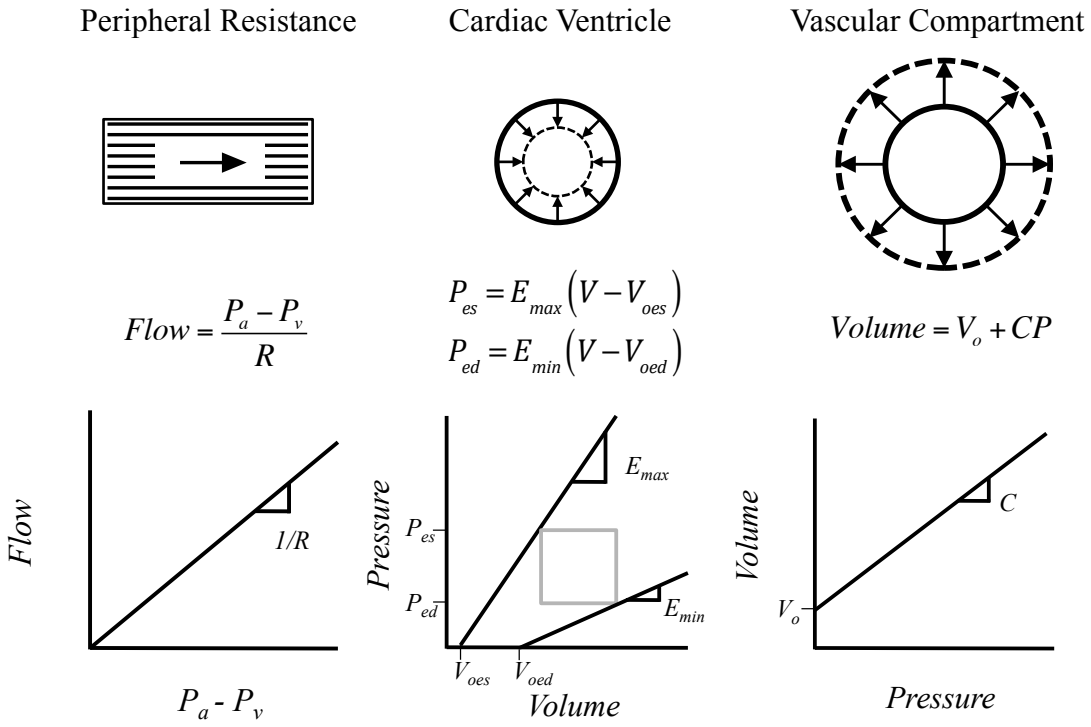

Figure 1. Description of the three components of the minimal closed-loop model. Blood flow through the peripheral vasculature is determined by the difference in arterial pressure (P_a) and venous pressure (P_v) and vascular resistance (R). Ventricular systolic (P_{es}) and diastolic pressure (P_{ed}) are determined by the unstressed ventricular volumes (V_{oes}, V_{oed}), elastances of the ventricle (E_{max}, E_{min}) and volume in the ventricle (V). Volume in the vascular compartments is determined by volume at zero pressure (V_o), total vascular compartment compliance (C), and pressure in the compartment (P).

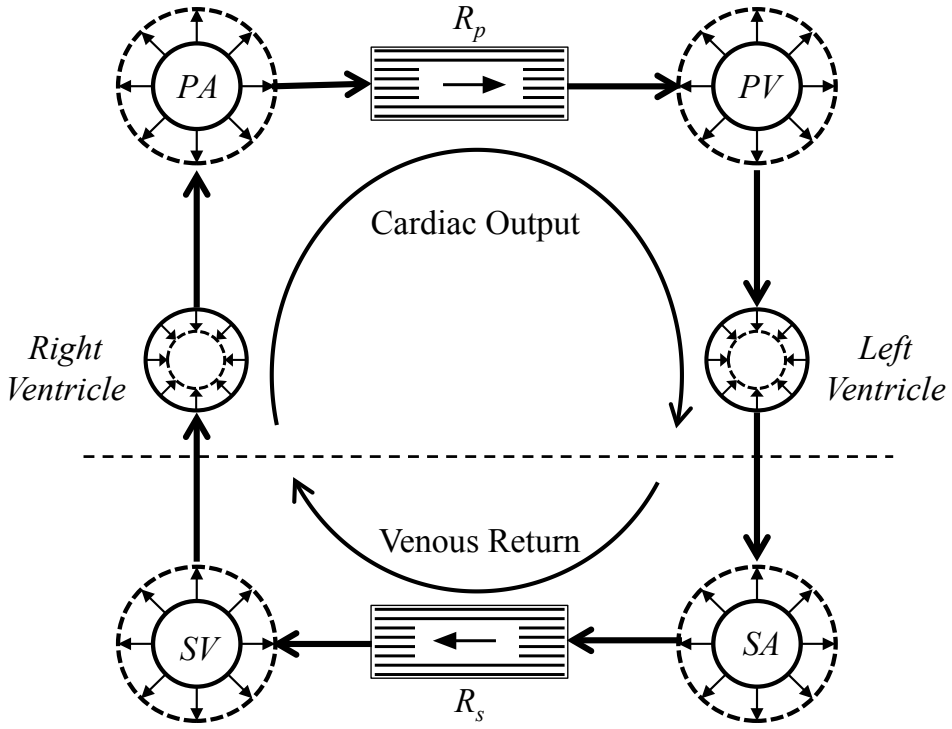

Figure 2. Illustration of standard minimal closed-loop system is composed of four vascular compartments: systemic arteries (*SA*), systemic veins (*SV*), pulmonary arteries (*PA*), and pulmonary veins (*PV*); two peripheral resistances: pulmonary resistance (R_p) and systemic resistance (R_s); and the left ventricle (*LV*) and the right ventricle (*RV*). Components described in Fig. 1. Consistent with Guyton et al. (87), the cardiovascular system is separated into two parts characterized by the cardiac output though the two ventricles and pulmonary vasculature (above dashed line) and the venous return through the systemic circulation (below dashed line).

Model equations. Figure 2 illustrates the minimal closed-loop model in terms of the three types of components described in Fig. 1. *Equations A1-A17* include subscripts for parameters illustrated in Fig. 1 to specify their particular locations. For simplicity, subscripts *a* and *v* refer to arterial and venous, *p* and *s* refer to pulmonary and systemic, and *l* and *r* refer to left and right. In addition, *Eq. A13* characterizes conservation of

mass, where blood volume (V_B) neglects the small blood volumes stored in the cardiac ventricles. *Equations A14* and *A15* specify approximations for end-systolic ventricular pressures made by Sunagawa et al. (256). Furthermore, the common assumption (100, 256) was made that the end-diastolic pressures are approximated by venous pressures (*Eqs. A16* and *A17*). Taken together, *Eqs. A1-17* are consistent with equations assumed by Sunagawa et al. (257) to derive algebraic solutions for hemodynamic variables.

Solving the equations assuming systemic arterial pressure is regulated. The equations in *Appendix A* are equivalent to the model equations assumed by Sunagawa et al. (256). However, in contrast to their solutions, we assumed that systemic arterial pressure (P_{sa}) was a constant parameter, and blood volume was a predicted variable. Therefore, *Eqs. A1-A17* were solved for five variables: *CO,* $P_{sv,}$ $P_{pa,}$ P_{pv} and V_B. As a result of explicitly solving for these five variables, all other qualities were implicitly assumed to be constant parameters (i.e., P_{sa}, R, C, V_o, E_{max}, E_{min}, V_{oed}, V_{oes}).

Separately characterizing cardiac output (*CO*) *and venous return* (*VR*) *curves*. Consistent with Guyton's original characterization of cardiac function (81), *CO* was expressed as the flow through both ventricles and the pulmonary vasculature (Fig. 2). The governing equations for these elements (*Eqs. A2-A8*) were simultaneously solved for *CO*, P_{pa}, and P_{pv}. As a result, *CO* was expressed as a function of constant parameters of the cardio-pulmonary system and systemic venous pressure (P_{sv}). In this case, P_{sv} was assumed to approximate right-atrial pressure (*Eq. A17*). The slope of the resulting cardiac function curve was found by taking the derivative with respect to P_{sv}, and intercept with the abscissa was found by setting *CO* equal to zero and solving for P_{sv}. To

simplify the expression, the resulting solutions were expressed in terms of the difference in ventricular end-diastolic and end-systolic unstressed volumes (i.e., $\Delta V_{olv}=V_{oedlv}-V_{oeslv}$ and $\Delta V_{orv}=V_{oedrv}-V_{oesrv}$). Similarly, consistent with Guyton's original characterization of "venous return" as a function of P_{sv}, *VR* was expressed as the flow through the systemic vasculature. *Equation A1* is already in the form of venous return as a function of systemic venous pressure (P_{sv}), assuming constant systemic arterial pressure (P_{sa}) and systemic resistance (R_s). Slopes and intercepts of this venous return curve were found as they were for the cardiac output curve.

Cardiac output-venous return balance point graphs. As in Guyton (81), cardiac output and venous return can be plotted on the same graph as a function of systemic venous pressure (P_{sv}). Assuming conservation of mass, the intersection of the two lines represents the equilibrium point where *CO* is equal to *VR*. The values of *CO* and P_{sv} in equilibrium are denoted as CO^* and P_{sv}^*.

Piecewise linear approximation of end-diastolic pressure-volume relationship. Although the parameters of the circulation (*HR*, V_B, *R*, *C*, V_o, E_{max}, E_{min}, V_{oed}, V_{oes}) can vary with pressure (179), to arrive at algebraic solutions, they were assumed to be constant. However, the ventricular end-diastolic elastance and unstressed volume (characterized by E_{min} and V_{oed}, respectively) are particularly sensitive to changes in ventricular filling pressure. To account for the large variation in E_{min} and V_{oed}, we characterized the end-diastolic pressure-volume relationship (*Eqs. A5* and *A6*) with a nonlinear relationship (*Eq. B1*) reported by Klotz et al. (121). As detailed in *Appendix B*, this nonlinear relationship was approximated by two contiguous lines with different

values for E_{min} and V_{oed} for low (E_{min1} and V_{oed1}) and high (E_{min2} and V_{oed2}) ventricular filling volumes.

Parameters used for plotting results. Parameter values are readily available from previously reported models (30, 99, 257, 270). We used values from the previously-published model (99) which most closely matched the description of the circulation in Fig. 2. In addition, parameter values were retrieved from a reported clinical study (57) for heart failure with preserved ejection fraction (HFpEF) and heart failure with reduced ejection fraction (HFrEF), as were values for P_{sa} (57, 75). Values for the piecewise linear approximation of E_{min} and V_{oed} were calculated from reported end-diastolic relationships for normal (121, 208) and heart failure (57) conditions as described in detail in *Appendix B*. Right ventricular values were assumed to be unchanged in heart failure. Total pulmonary and systemic resistances included their respective arterial and venous resistances. All parameter values for baseline and heart failure conditions are summarized in Table 1.

Cardiac output-venous return in heart failure. A cardiac output-venous return graph was created and compared to a classical qualitative graph presented by Guyton (87). To match Guyton's *CO* curves in baseline conditions, values of ΔV_{orv}, ΔV_{olv} and E_{minrv} were adjusted from the baseline values in Table 1. To illustrate heart failure, E_{maxlv} and E_{maxrv} were then decreased by 30%.

Validation. Predicted cardiac output and systemic vascular pressures were compared to previously measured values for normal conditions, as well as HFpEF and HFrEF conditions (Table 2).

Type	Variable	Normal	Ref	HFpEF	Ref	HFrEF	Ref
Ventricular Properties	E_{maxlv} (mmHg/mL)	2.50	(99)	2.50	(99)	0.74	(267)
	E_{minlv1} (mmHg/mL)	0.11	(121)	0.44	(57)	0.09	(57)
	E_{minlv2} (mmHg/mL)	2.28	(121)	8.00	(57)	1.80	(57)
	ΔV_{olv} (mL)	32.91	(121)	31.67	(57)	68.96	(57)
	ΔV_{olvm} (mL)	164.99	(121)	189.70	(57)	242.65	(57)
	E_{maxrv} (mmHg/mL)	0.83	(99)	0.83	(99)	0.83	(99)
	E_{minrv} (mmHg/mL)	0.05	(208)	0.05	(208)	0.05	(208)
	E_{minrv2} (mmHg/mL)	0.22	(208)	0.22	(208)	0.50	(208)
	ΔV_{orv} (mL)	32.65	(208)	32.65	(208)	32.00	(208)
	ΔV_{orvm} (mL)	63.03	(208)	30.38	(208)	62.38	(208)
	V'_{lv} (mL)	117.25	(121)	115.70	(57)	180.67	(57)
	V'_{rv} (mL)	117.67	(208)	117.67	(208)	117.67	(208)
	HR (/s)	1.20	(99)	1.72	(57)	1.33	(57)
Resistive Properties	R_s (mmHg*s/mL)	1.06	(99)	1.20	(57)	1.11	(57)
	R_p (mmHg*s/mL)	0.09	(99)	0.22	(57)	0.17	(57)
Compliant Chambers	C_{sa} (mL/mmHg)	1.60	(99)	1.60	(99)	1.60	(99)
	C_{sv} (mL/mmHg)	100.00	(99)	100.00	(99)	100.00	(99)
	C_{pa} (mL/mmHg)	4.30	(99)	4.30	(99)	4.30	(99)
	C_{pv} (mL/mmHg)	8.40	(99)	8.40	(99)	8.40	(99)
	V_{otot} (mL)	3795.00	(99)	3795.00	(99)	3795.00	(99)
	P_{sa} (mmHg)	90.00	(75)	87.00	(57)	103.00	(57)

Table 1. Parameter sets for normal and heart failure solutions (HFpEF, HFrEF) were found from previously published parameter sets (99, 208, 267) or data (57, 74, 121) as listed (Ref). A full description of parameter sources may be found in the Methods and *Appendix B*.

	Normal		HFrEF (EF<40%)		HFpEF (EF>50%)	
Variable	Predicted	Reported	Predicted	Reported	Predicted	Reported
***CO* (mL/s)**	80.58	67-133	71.05	80±23	74.47	86.67±22
P_{sv} (mmHg)	4.91	0-6	8.35	7.4±15	13.59	9.6±4.2
P_{pa} (mmHg)	14.84	10-20	21.49	28±11	39.80	34±17
P_{pv} (mmHg)	7.59	6-12	9.13	16±7	23.27	19±9

Table 2. Predicted hemodynamic values fall within range of previously-reported values. Predicted values are compared to reported values for normal subjects (75), subjects with heart failure reduced ejection fraction (HFrEF) and preserved ejection fraction (HFpEF) (57). Parameter values used for validation are illustrated in Table 1. The assumed values for systemic arterial pressure for Normal, HFrEF and HFpEF were 90, 87, and 103 mmHg to match reported mean values.

2.3 Results

Algebraic formula for equilibrium values. Solving *Eqs. A1-A17* in *Appendix A* yields algebraic solutions for CO^*, P_{sv}^*, P_{pa}^*, P_{pv}^*, and V_B^* (*Eqs. A19-A23*). Notably, because blood volume is a variable, CO^*, P_{sv}^*, P_{pa}^*, and P_{pv}^* are independent of (i.e., do not include) vascular compliances (C_{sa}, C_{sv}, C_{pa}, C_{pv}), unstressed vascular volumes (V_{osa}, V_{osv}, V_{opa}, V_{opv}), and blood volume (V_B). The variable V_B^* is much more complicated because it includes these compliances and unstressed volumes.

Characterizing cardiac output and venous return as a function of systemic venous pressure. Assuming P_{sa} is regulated, cardiac output is,

$$CO = \frac{HR\left(\Delta V_{orv}E_{maxrv}+\Delta V_{olv}E_{minlv}-\frac{E_{minlv}P_{sa}}{E_{maxlv}}+\frac{E_{maxrv}P_{sv}}{E_{minrv}}\right)}{E_{maxrv}+E_{minlv}+R_pHR}. \quad (1)$$

The corresponding equation for venous return is identical to *Eq. A1*,

$$VR = \frac{P_{sa} - P_{sv}}{R_s}. \qquad (2)$$

Both *VR* and *CO* are linear functions of P_{sv}.

Equilibrium values for cardiac output and systemic venous pressure. Simultaneously solving *Eqs. 1* and *2* results in algebraic relationships for equilibrium cardiac output (CO^*),

$$CO^* = \frac{HR\left(E_{minlv}\Delta V_{olv} + E_{maxrv}\Delta V_{orv} + P_{sa}\left(\frac{E_{maxrv}}{E_{minrv}} - \frac{E_{minlv}}{E_{maxlv}}\right)\right)}{E_{minlv} + E_{maxlv} + R_p HR + \frac{E_{maxrv} R_s HR}{E_{minrv}}}, \qquad (3)$$

and equilibrium systemic venous pressure (P_{sv}^*),

$$P_{sv}^* = \frac{P_{sa}\left(E_{maxrv} + E_{minlv} + HR\ R_p - \frac{HR\ R_s E_{minlv}}{E_{maxlv}}\right) + HRR_s(E_{minlv}\Delta V_{olv} + E_{maxrv}\Delta V_{orv})}{E_{minlv} + E_{maxlv} + R_p HR + \frac{E_{maxrv} R_s HR}{E_{minrv}}}. \qquad (4)$$

Although *Eqs. 3* and *4* do not require the assumption of model equations characterizing the vascular compartments (i.e., *Eqs. A9-A13*), they are identical to *Eqs. A19* and *A20*. It is striking that parameters ΔV_{olv} and ΔV_{orv}, often assumed to be negligible (30, 256), have a significant impact on equilibrium cardiac output and systemic venous pressure.

Graphical representation of cardiac-output and venous return. Figure 3 represents the interaction of cardiac output (*Eq. 2*) with venous return (*Eq. 1*). Figure 3A illustrates cardiac output as a function of systemic venous pressure (*Eq. 2*). The slopes and abscissa intercept are,

CO slope: $$\frac{\frac{HR}{E_{minrv}}}{\left[1 + \frac{E_{minlv}}{E_{maxlv}}\frac{E_{maxlv}}{E_{maxrv}} + \frac{R_p HR}{E_{maxrv}}\right]}, \qquad (5)$$

CO intercept: $$\left[\frac{E_{minrv}}{E_{maxrv}}\frac{E_{minlv}}{E_{maxlv}}\right](P_{sa} - E_{maxlv}\Delta V_{olv}) - E_{minrv}\Delta V_{orv}. \qquad (6)$$

Cardiac output in Fig. 3A is represented by two contiguous lines, resulting from linearizing the end-diastolic pressure-volume relationship (*Appendix B*). Both slopes are governed by *Eq. 5*, and both intercepts are governed by *Eq. 6*. However, the values of E_{minrv} and V_{orv} take on different values at low and high ventricular filling volumes. Unitless terms (i.e., non-dimensional) in *Eqs. 5* and *6* are enclosed within brackets, and include four distinct ratios. The term R_pHR/E_{maxrv} characterizes ventricular-arterial coupling, and is an approximation for the ratio of effective arterial elastance to maximum end-systolic elastance (i.e., E_a/E_{max}) (257). The terms E_{maxlv}/E_{minlv} and E_{maxrv}/E_{minrv} are relative ventricular contractilities (287). The term E_{maxlv}/E_{maxrv} is the relative contractilities of the left and right ventricles (287). Figure 3B illustrates the systemic venous return, with relatively simple slope and abscissa intercept:

VR slope: $-\frac{1}{R_s}$, *(7)*

VR intercept: P_{sa}. *(8)*

Figure 3C plots both *CO* and *VR* simultaneously, with the intersection representing equilibrium cardiac output (CO^*, *Eq. 3*) and systemic venous pressure (P_{sv}^*, *Eq. 4*).

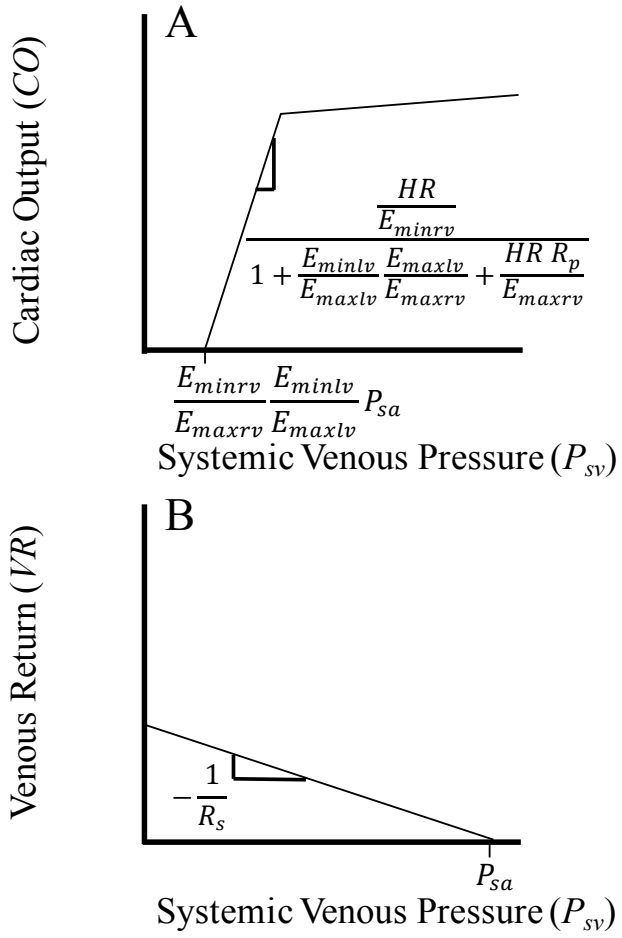

Figure 3. Representation of the chronic cardiac function-venous return balance point in terms of parameters for the minimal closed-loop model (Fig. 2). A) Cardiac output (*CO*) increases with systemic venous pressure (P_{sv}) as described by *Eq. 1*. The slope (*Eq. 5*) and intercept (*Eq. 6*) are indicated on the graph. The bend in the curve arises from changing parameters characterizing the end-diastolic pressure-volume relationship to account for increased ventricular stiffness at higher ventricular filling pressures (*Appendix B*). B) Venous return (*VR*) decreases with P_{sv} as described by *Eq. 2*. The slope (*Eq. 7*) and intercept (*Eq. 8*) are indicated on the graph. C) The intersection of the curves represents equilibrium balance points (P_{sv}^*, CO^*), where *CO* = *VR,* predicted by *Eqs. 3* and *4*.

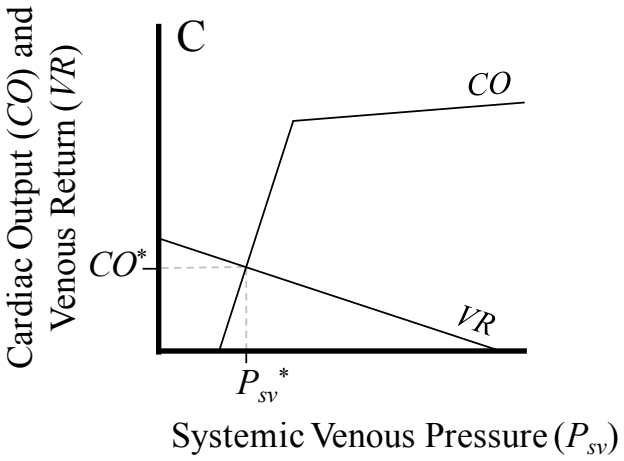

Figure 3. Continued.

Cardiac output-venous return balance point graphs. Figure 4A reproduces a standard cardiac output-venous return balance point graph from Guyton et al. (87). It illustrates equilibrium for a healthy subject (intersection of solid lines, *a*), as well as equilibrium for a subject with heart failure (intersection of dashed lines, *b*). Compensation to reduced cardiac function is represented as a shift in the systemic filling pressure from P_{sf1} to P_{sf2} caused by blood volume expansion. To compare, Fig. 4B illustrates how heart failure shifts the novel graphical balance point illustrated in Fig. 3C. Equilibrium for a healthy subject is illustrated by the intersection of solid lines (*a*). With heart failure, the decrease in cardiac contractility shifts the cardiac function curve down and to the right. However, with the assumption of chronic regulation of systemic arterial pressure, the venous return curve is unaffected. The new equilibrium (intersection of dashed lines, *b*) indicates only a small decrease in cardiac output, because the slope of the venous return ($-1/R_s$) is small.

Validation. Table 2 illustrates that pressures and cardiac output were predicted to fall within normal ranges for baseline values reported in the literature. Observed changes in pressures and cardiac output with heart failure were reproduced with parameters (Table 1) representing two types of heart failure (HFrEF and HFpEF).

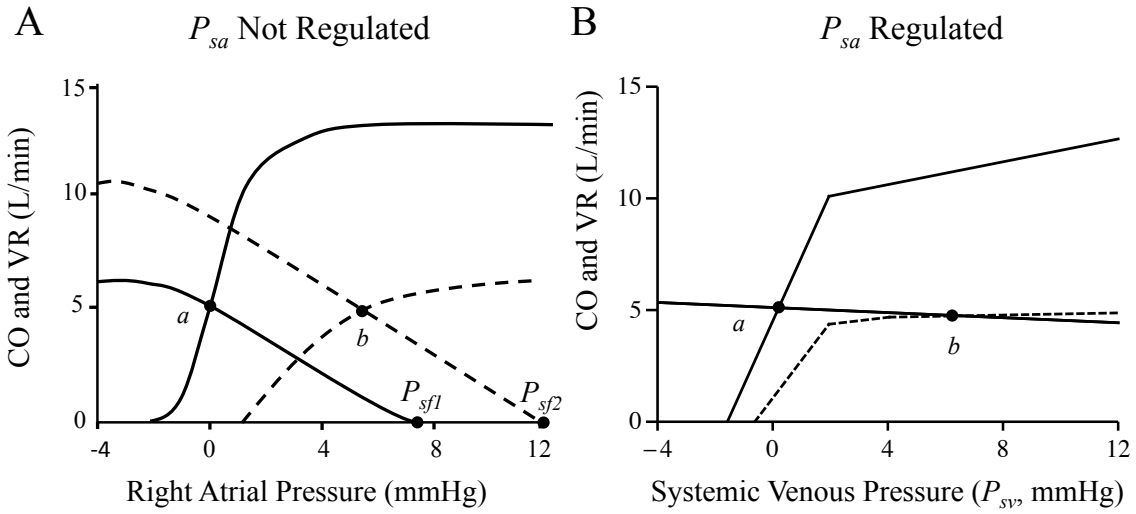

Figure 4. Graphical representations of compensation to heart failure. A) Guyton's classic graph (87) illustrates how the interaction of normal cardiac output (CO) and venous return (VR) curves (solid lines) yields a normal equilibrium (*a*). Heart failure (dashed curves) is represented by a shift of the output curve down and to the right. Compensation is achieved by increasing systemic filling pressure from P_{sf1} to P_{sf2}, resulting in a new equilibrium (*b*). B) The new balance point graph is predicted from the minimal closed-loop model assuming chronic systemic arterial pressure regulation. Intersection of normal cardiac output (*CO*, *Eq. 1*) and venous return (*VR*, *Eq. 2*) curves (solid lines) yields a normal equilibrium (*a*). Heart failure (dashed curves) represented by a decrease in parameters characterizing cardiac contractility (E_{max}), shifting the cardiac contractility down and to the right. The venous return curve does not change. Equilibrium values of cardiac output and systemic venous pressure (*b*) are predicted quantitatively by *Eqs. 3* and *4*. Curves in A digitized from Guyton (87) and replotted in a new graph.

2.4 Discussion

By managing the complexity of the mathematical model, the present work was able to develop general algebraic predictions of the interaction of cardiac output and venous return when systemic arterial pressure is chronically regulated. The vast majority of modeling studies increase complexity as a means to better reproduce specific behavior of a system characterized by a specific set of parameter values. In contrast, we rigorously constrained complexity by 1) assuming the minimal closed-loop model, 2) linearizing all model equations, and 3) assuming systemic arterial pressure is a constant parameter. As described in detail below, each of these three simplification strategies impose limitations. Nonetheless, they result in general algebraic formulas (*Eqs. A19-A23*) that extend the seminal works of Sunagawa et al. (256, 257) to chronic conditions in which systemic arterial pressure is regulated via renal function. Although simplification can lead to error (Table 2), the resulting general formulas explicitly relate mechanical properties to critical hemodynamic parameters without requiring advanced computational skills or knowledge of a large number of parameter values. The value of these general formulas is evidenced by the revelation that the most difficult parameters to measure, such as vascular compliances and unstressed volumes (221), become irrelevant to pressures and cardiac output for timescales that allow blood volume to vary. Furthermore, they provide a novel alternative to Guyton's classical cardiac output-venous return graph (Fig. 3) that is both predictive and applicable to chronic conditions such as heart failure (Fig. 4). The simplicity imposed upon the model thus yields tools that are conceptually tractable and accessible to cardiovascular investigators, clinicians,

and students. The present work was able to develop these novel tools by significantly deviating from convention by valuing the broad applicability of general solutions to a greater extent than the accuracy of specific predictions.

Limitations imposed by assuming the minimal closed-loop model. Numerous investigators have used the structure of the minimal closed-loop model illustrated in Fig. 2 as a basis to study integrative cardiovascular physiology (99, 241). Despite the difficulty in measuring all relevant mechanical properties (221), these models have achieved a high degree of acceptance because they have been repeatedly validated experimentally in animal models (185, 267) and human subjects (100, 241, 242). Because the present work also assumes the minimal closed-loop model, however, it shares the same limitations. For example, ventricles are characterized by a time-varying elastance that neglects Hill Effects (192). Vascular networks are lumped into compartments that neglect effects of pulse wave propagation and reflection (209), which particularly impacts predictions of pulsatile pressures of young, normotensive subjects (161). The effects of respiration (144) and posture (100) are similarly neglected, as well as the mechanical coupling of the ventricles (242). In addition, end-diastolic pressures are assumed equal to venous pressures, which neglects valve resistances and atrial contraction. Although expressed in terms of mean pressures and cardiac output (*Eqs. A19-A22*), the solutions are consistent with Sunagawa's (256) characterization of pulsatile arterial pressures (*Eq. A18*, *Appendix A*). To capture the effects of particular mechanical properties that are otherwise neglected or lumped within the minimal closed-loop model illustrated in Fig. 2, investigators have added a wide array of resistances and

compliant chambers in series and parallel to the elements of the minimal closed-loop model illustrated in Fig. 2 (137, 151). For conceptual clarity, the present work did not include any of the numerous possible modifications. Applying the methodology delineated in the present work, however, will also yield general algebraic formulas, provided that any additional elements are characterized by linear pressure-volume or pressure-flow relationships.

Limitations imposed by linearizing model equations. Investigators typically use linear relationships to characterize most elements of the minimal closed-loop model. In fact, with very few exceptions (144), all vascular pressure-flow, vascular pressure-volume, and ventricular end-systolic pressure-volume relationships are assumed to be linear as in Fig. 1. As a result, mechanical properties are typically characterized by a relatively small number of constant parameters (i.e., R, C, V_o, V_{oes}, and E_{max}). More accurate nonlinear equations that capture the complexity of these relationships are typically avoided because they would require a larger number of parameters (39, 132). Investigators typically justify linearization by invoking the principle that any nonlinear relationship can be approximated by a linear equation (with a slope and an intercept) within a limited range (37). In fact, modeling studies have invoked this principle to assume a linear end-diastolic pressure-volume relationship (100, 256), which is essential for the present work (i.e., *Eqs. A5* and *A6*). Because ventricular end-diastolic volume is particularly sensitive to small changes in filling pressure, however, investigators often resort to characterizing the end-diastolic pressure-volume relationship with a nonlinear function (e.g., *Eq. B1*). However, assuming nonlinear equations typically makes it

impossible to derive algebraic solutions (36). Figure 5 illustrates how linearity is maintained by treating such curvilinear relationships as "piecewise linear".

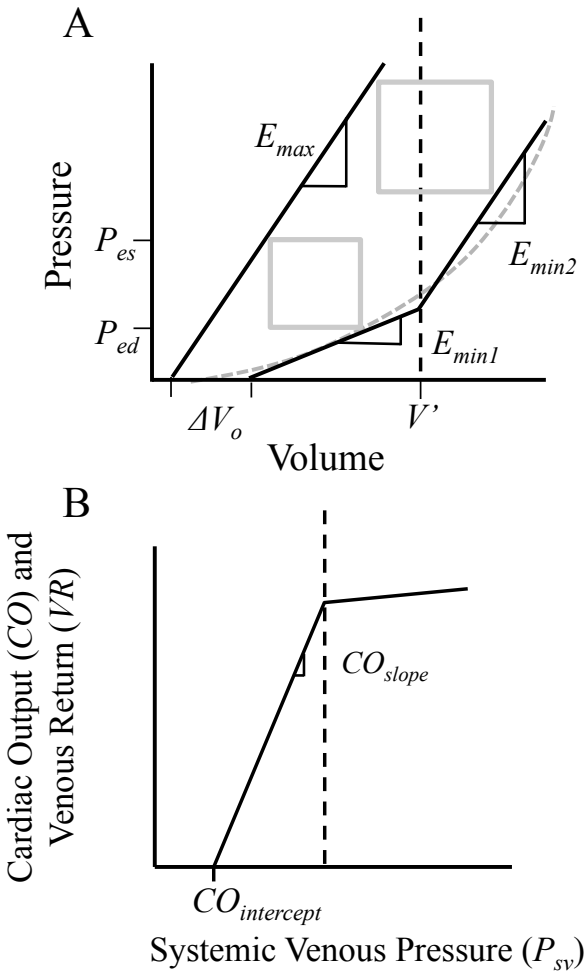

Figure 5. Effect of characterizing the nonlinear end-diastolic pressure-volume relationship by two linear relationships. A: The nonlinear end-diastolic pressure volume relationship (*Eq. B2*, dashed curve) can be approximated by two lines characterized by *Eq. B1*, but with different slopes (E_{min1} and E_{min2}). E_{min2} is a better approximation of the nonlinear relationship as ventricular volume increases above V'. B: The piecewise linear relationship results in a cardiac output that plateaus at higher systemic venous pressures. Illustrated is the special case that E_{min2} approximates E_{max}.

As a result, the general algebraic formulas are maintained, and only the values of specific parameters (e.g., E_{min} and V_{oed}) must be altered. In this illustrative case, approximating the nonlinear end-diastolic pressure-volume relationship in Fig. 5A with two contiguous lines results in a bend on the cardiac output curve in Figs. 3-5. Similarly, nonlinearity of the end-systolic pressure-volume relationship can be approximated by adjusting values of E_{max} and V_{oes} in the general algebraic formulas. A similar approach can be used to capture nonlinearities in peripheral vascular pressure-flow relationships, although new formulas must be derived (not shown) after adding a parameter representing a nonzero intercept to *Eqs. A1 and A2*. Treating relationships as "piecewise linear" is a common approach to address the fact that "constant" parameters can vary in extreme conditions (36, 59).

Limitations imposed by characterizing a systemic arterial pressure as a constant parameter. Although it is rarely acknowledged, investigators must choose which cardiovascular properties will be treated as constant parameters to solve the equations (38) characterizing the minimal closed-loop model. Universally, investigators have made this choice by solving equations for hemodynamic variables: cardiac output, vascular volumes, and blood pressures. As a direct consequence, all other cardiovascular properties have been implicitly assumed to be constant parameters, including most notably total blood volume (V_B). This ubiquitous choice may have originated in early attempts to match model predictions with highly controlled acute experiments that deliberately eliminated feedback mechanisms. It is commonly recognized (271) that many of this standard set of constant parameters are actually highly variable in

timescales exceeding 1 sec because they are affected by homeostatic mechanisms that maintain systemic arterial pressure. To address pressure homeostasis, investigators have added additional equations to the minimal closed-loop model to represent the baroreflex (144) or renal function (9). Although this approach is necessary to investigate the *mechanisms* of pressure regulation, it requires numerical solution and a significant expansion of constant parameters that must be assigned particular values (271). Although blood pressure is acutely regulated through the baroreflex, over the course of hours, pressure control is achieved primarily through changes in blood volume (142). With intact renal function, the feedback is so effective that mean systemic arterial pressure remains nearly constant, even with significant perturbations. Therefore, in the present work we take a fundamentally different approach. To capture the *effect* of pressure homeostasis, we made a novel choice to treat systemic arterial pressure as constant parameter, and treat total blood volume as a variable when solving *Eqs. A1-A17*. This choice imposes its own limitations. For instance, the resulting solutions (*Eqs. A19-A23*) would not predict effects of acute perturbations that are modulated by the baroreflex. Furthermore, our assumption that blood volume is controlled would fail in the case of renal dysfunction. The general algebraic solutions of the present work are nonetheless consistent with Guyton's assertion that normal renal function provides "infinite feedback" that eventually overrides other acute homeostatic mechanisms to maintain systemic arterial pressure. The present work therefore extends the seminal work of Sunagawa et al. (256) to provide algebraic solutions that are particularly relevant to chronic disease states.

Validity of general algebraic solutions versus validity of specific numerical results. Perhaps the greatest limitation of closed-loop models that require numerical solutions is that they must assume specific parameter values. The origin of assumed parameter values for any particular study are often obscure. Because many properties are difficult to measure, parameter values are often borrowed from other species (144), carefully curated from the clinical literature (271), or are chosen by advanced methods that minimize error of a set of predicted variables (i.e., curve fitting) (169). However, even fairly well-characterized properties such as E_{max} can exhibit wide variation amongst healthy subjects (247). It is therefore unsurprising that various modeling studies (30, 100, 144, 270) assume such divergent values for E_{max} (2-4.3 mmHg/ml) and E_{min} (0.014-0.833 mmHg/ml). To estimate model accuracy (Table 2) and produce illustrative graphs (Figs. 3-5), we also had to assume particular parameter values. However, we used the insights afforded by algebraic solutions to arrange parameters into nondimensional groups whose values have a small range of variation (e.g., E_{maxlv}/E_{minlv}, E_{maxrv}/E_{minrv}, and R_pHR/E_{maxrv}). In fact, most nondimensional terms in *Eqs. 5* and *6* are recognized as allometric invariants (165, 287) and thus the collected terms have a similar value across (healthy) mammalian species. Notably, the only difference in slope of the cardiac output curve amongst mammals is due to the term (HR/E_{minrv}), which increases with mammal size. From this, it can be inferred that $CO/(HR/E_{minrv})$ would also be an allometric invariant. Furthermore, the value of P_{sa} is similar across mammals (135), suggesting $E_{maxlv}\Delta V_{olv}$ and $E_{minrv}\Delta V_{orv}$ may also have similar values across mammalian species. Since ΔV_{olv} and ΔV_{orv} arise out of the present work, the variance across mammals has yet

to be determined. Taken together, normalizing the cardiac output axis by HR/E_{minlv} and systemic venous pressure axis by P_{sa} may transform Fig. 3 into a universal figure characterizing the cardiovascular system of all mammals. Despite the many simplifying assumptions, a standard set of parameter values results in pressures and flows that fall within normal ranges, and reproduce shifts in blood pressures and cardiac output with heart failure (Table 2). Although incorporating additional structural elements, nonlinearities, and control mechanisms into the minimal closed-loop model may further decrease apparent error, model equations may not be able to be solved algebraically. In fact, the general algebraic solutions for a simple model may paradoxically retain far more validity than specific numerical solutions of a more detailed model. Numerical results from more complex models are not valid for subjects that do not precisely match the assumed set of parameter values. Possibly even more problematic, the conclusions drawn from all previously-published modeling studies can potentially be rendered invalid if but one of the 16 or more assumed parameter values are ever found to be inaccurate (276).

In chronic conditions, vascular compliance, unstressed volumes, and total blood volume do not affect blood pressures and flow. In his seminal work (87, 89), Guyton introduced the concept of "circulatory filling pressure" (P_{cf}) to characterize the role of blood storage to the regulation of blood pressures and cardiac output. He noted that with cardiac arrest, all pressures equilibrate to P_{cf}. As in the present work, he assumed four compliant chambers to relate P_{cf} to total blood volume, total vascular unstressed volumes, and total vascular compliance,

$$P_{cf} = \frac{V_B - (V_{osa} + V_{osv} + V_{opa} + V_{opv})}{C_{sa} + C_{sv} + C_{pa} + C_{pv}}. \quad (9)$$

This concept was later refined by characterizing the blood volumes stored in pulmonary and systemic circulations separately, leading to the concept of "systemic filling pressure" P_{sf},

$$P_{sf} = \frac{V_{sa} + V_{sv} - (V_{osa} + V_{osv})}{C_{sa} + C_{sv}}. \quad (10)$$

In Guyton's original experiments characterizing venous return, systemic blood volume was set constant (89). In this case, P_{sf}, ranging from 10.2-18.76 mmHg (114, 145), became a critical parameter (87) that determines the intercept of the venous return curve (i.e., Fig. 4A). Because it is commonly believed that vascular compliances and unstressed volumes have a major impact on P_{sf} (145), it is also believed they have a critical impact on cardiac output and blood pressures in chronic conditions (84, 222). The present work, however, leads to a very different conclusion. When systemic arterial pressure is homeostatic, vascular compliances and unstressed volumes become irrelevant to chronic cardiac output and blood pressures. None of the eight parameters characterizing compliances and unstressed volumes appear in *Eqs. 1-8*. In contrast to acute models that assume a constant volume (1, 137, 245), our algebraic solutions exclude the six most problematic parameters of the standard minimal closed-loop model. Perhaps as important, the present work reveals that in chronic conditions where normal renal function leads to pressure homeostasis, the minimal closed-loop model reduces from the eight components illustrated in Fig. 2 to four (two ventricles and two peripheral resistances). Our general algebraic formula can thus be derived from just from model

Eqs. A1-A8 with approximations *A14-A17,* assuming that CO, P_{sv}, P_{pa}, and P_{pv} are variables. Because properties of vascular compartments become irrelevant, so too does the concept of systemic filling pressure in chronic conditions.

Novel alternative to Guyton's classical cardiac output-venous return graph that is applicable to chronic conditions. Figure 4A illustrates one of the most enduring examples of how Guyton's classic cardiac function-venous return graph can be used to explain clinically relevant observations. In this case, heart failure decreases the slope of the cardiac output curve, and blood volume expansion increases P_{sf}, which shifts the venous return curve to the right, ultimately restoring cardiac output. The ability to adjust slopes and intercepts to represent various disease states has led to widespread adoption of this graphical approach in standard medical physiology textbooks (18, 95). Although Guyton's classic balance point graph exemplifies integrative cardiovascular physiology, its conventional implementation engenders significant limitations. First, cardiac output curves are system-level characterizations adapted from empirical observations, and are not directly related to cardiovascular properties at the organ level (e.g., E_{max}) (81). Second, venous return curves assume a constant P_{sf}, which includes the non-physiologic assumption that systemic blood volume is constant and unaffected by changes in cardiac function (14). Third, both cardiac output and venous return curves were characterized in the absence of pressure homeostasis, and graphs lack any reference to systemic arterial pressure. Fourth, Guyton's cardiac output-venous return curves are primarily descriptive, and students, clinical investigators, and physiologists alike must resort to assuming (or memorizing) qualitative shifts in two slopes and two intercepts to reproduce known

changes in cardiac output and systemic venous pressure with particular disease states. Taken together, Guyton's classic graph can aid conceptualization of the interaction of cardiac output and venous return, yet it remains primarily descriptive. In contrast, the present work provides a novel alternative to Guyton's classic cardiac output-venous return graph that 1) quantifies slopes and intercepts in terms of standard organ-level cardiovascular parameters, 2) does not assume systemic blood volume is constant, 3) is consistent with systemic arterial pressure homeostasis that forms a simple intercept (P_{sa}), and 4) makes the quantitative, predictive power of the minimal closed-loop model accessible to those without advanced computational skills. Although applied to chronic conditions where systemic arterial pressure is regulated by renal control of blood volume, the simplifying approach presented in the present work can be applied to yield general algebraic formulas for acute conditions where systemic arterial resistance is variable, as well as during growth and development, when ventricular contractility and diastolic stiffness are variables.

3. COUPLING VASCULAR AND INTERSTITIAL COMPARTMENTS

3.1 Background

The vascular and interstitial spaces are functionally coupled during heart failure. The blood and interstitial fluid compartments are anatomically coupled. Plasma enters interstitial compartments from the capillaries, and lymph exits interstitial compartments through the lymphatic vessels that converge and empty into the great veins of the neck. For healthy individuals, regulation of blood and interstitial fluid pressures, volumes, and flows can be studied in isolation, because homeostatic mechanisms functionally uncouple blood and interstitial compartments. For instance, control of blood volume by renal function results in chronic regulation of systemic arterial pressure (142). Similarly, multiple anti-edema mechanisms, including lymphatic function, control interstitial pressures to regulate interstitial fluid volume (49). Relatively large changes in heart rate, cardiac contractility, or peripheral resistance with exercise do not appreciably alter capillary or systemic venous pressures (288). However, with compensated heart failure, blood volume expansion ensures systemic arterial pressure is maintained (119) at the cost of elevated venous and capillary pressures (107). Increased capillary pressure enhances microvascular filtration into the interstitium, and increased systemic venous pressure inhibits lymphatic drainage out of the interstitium (53). Edema results when lymphatic function cannot fully compensate for these simultaneous challenges (44). Pulmonary edema in particular is one of the most devastating consequences of left ventricular failure (74). However, the clinical tools available to study pulmonary edema

such as response to exercise (231) or chest imaging and clinical examination (150, 248) have limited use for characterizing the numerous mediators responsible for edema.

Conventional animal and computational models for heart failure yield complex, model-dependent results. The physiological relevance of animal models of heart failure has long been debated. Results from animal models are often animal-specific (273) and impacted by measurement techniques (274). With the inability to reliably measure critical variables (248) or selectively control confounding compensatory mechanisms (274), investigators have resorted to using mathematical models. Although based on established principles such as conservation of mass and momentum, computational models require assumption of specific parameter values that are often poorly characterized (248) or vary significantly amongst subjects (247). Furthermore, mathematical models that seek to reproduce the complexity of the cardiovascular system, such as the seminal 400-parameter model by Guyton et al. (85), yield results that are notoriously difficult to interpret (102) or even reproduce (122). Investigators have since gravitated to more modest models that lump the vascular and interstitial spaces into two or three compartments to study their interaction (59, 94, 196, 220, 224). The vast majority of mathematical models must nonetheless be evaluated with advanced computational techniques that require each of the parameter values to be assumed *a priori*. Taken together, even reduced computational models of the cardiovascular system thus fail to yield simple, model-independent results.

The minimal closed loop cardiovascular model can be solved in terms of general, algebraic formulas predicting pressures, volumes, and flows from mechanical properties.

Three major strategies have arisen to manage the inherent complexity when modeling the cardiovascular system. First, because all changes in blood pressures, volumes, and flows are mediated through changes in the mechanical properties of the cardiovascular system (173), mathematical models have been constrained to include only mechanical properties (99, 191). Second, because the cardiovascular system can be adequately characterized in terms of "lumped" components characterizing the ventricles, peripheral resistances, and arterial and venous compartments, the number of critical parameters have been decreased by use of a "minimal closed-loop model" (99, 191). Third, because the equations characterizing mechanical properties can be linearized, they can be solved algebraically without assuming particular parameter values *a priori* (256, 257). Sunagawa et al. (256) first solved the equations characterizing the minimal closed loop model algebraically, providing general formulas for cardiac output and blood pressures. As was common practice for computational models, they assumed that blood volume was constant and systemic arterial pressure was variable. To include the regulation of systemic arterial pressure by renal function, in Section 2.2 we instead solved the equations assuming systemic arterial pressure was constant and blood volume was variable. The resulting general, algebraic formulas were then used to characterize alterations in systemic venous pressure with compensated heart failure.

The minimal interstitial fluid balance model can be solved in terms of general, algebraic formulas predicting pressures, volumes, and flows from mechanical properties. Similar to the algebraic solutions for the minimal closed-loop model, Dongaonkar et al. (49) developed algebraic solutions for interstitial pressure, volume, and flow that emerge

from the interaction of the microvasculature, an interstitial compartment, and a lymphatic system. This "minimal interstitial fluid balance model" assumed the Starling-Landis equation (289) to predict fluid flow into interstitial space as a function of oncotic and hydrostatic pressures and water and protein permeabilities. The Drake-Laine equation (130) was then employed to predict flow of fluid out of the interstitial space as a function of hydrostatic pressures and effective lymphatic resistance and effective lymphatic pump pressure. This model resulted in an algebraic solution that yielded general algebraic formulas for interstitial pressures and volumes as a function of capillary and systemic venous pressures (49). Although these minimal blood and interstitial models arise from similar approaches and use compatible assumptions, they have yet to be integrated. Therefore, the purpose of the present work is to integrate algebraic characterizations of the minimal closed-loop and interstitial fluid balance models to identify the primary mechanical determinants of pulmonary interstitial pressures in healthy subjects and subjects with compensated heart failure.

3.2 Methods

Closed-loop circulatory system. To characterize the cardiovascular-pulmonary interstitium interaction, a composite algebraic model based on the minimal closed loop model in Section 2.2 was coupled to the minimal interstitial fluid balance model of Dongaonkar et al. (49). Figure 6 illustrates the components of the integrated model that can be characterized either as resistances, pumping ventricles, or compliant compartments.

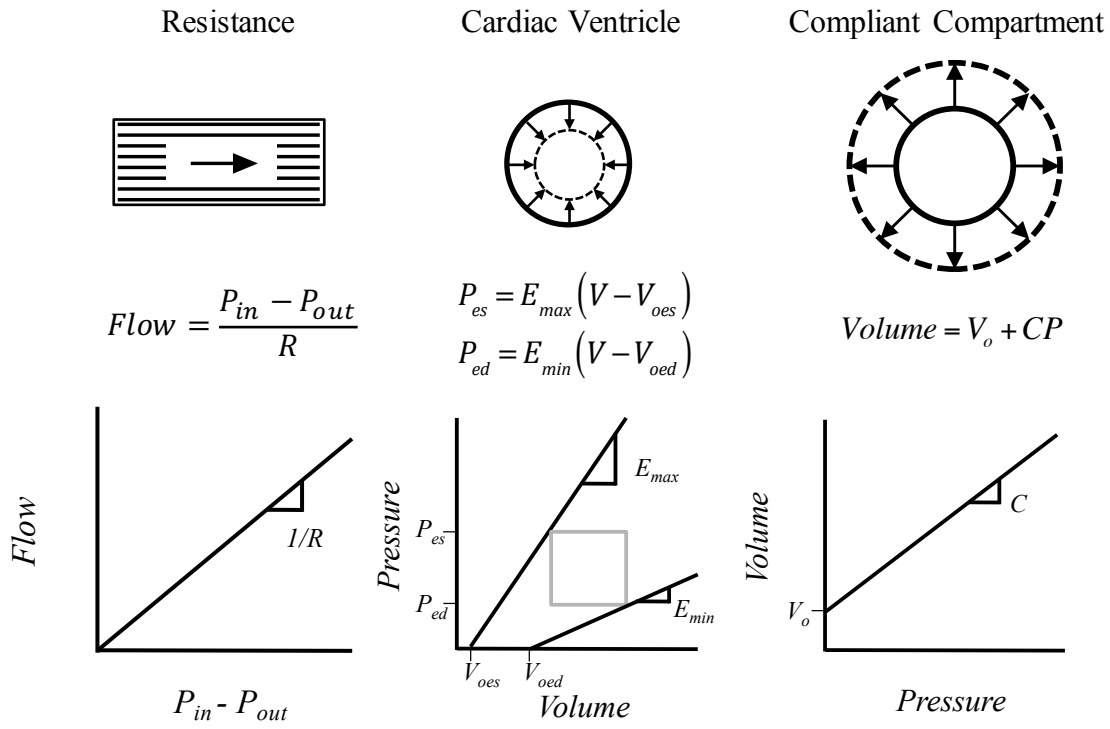

Figure 6. Components of the closed-loop and interstitial system. Flow through interstitial and vascular resistances is determined by the difference in inlet pressure (P_{in}) and outlet pressure (P_{out}) and resistance of the components (R). Microvascular filtration can be conceptualized as a resistance ($1/K_{fp}$). Ventricular end-systolic (P_{es}) and end-diastolic pressure (P_{ed}) are determined by the unstressed ventricular volumes (V_{oes}, V_{oed}), maximum and minimum elastances of the ventricle (E_{max}, E_{min}) and blood volume in the ventricle (V). Volume in the interstitial and vascular compartments is determined by the unstressed volume at zero pressure (V_o), total compartment compliance (C), and transmural pressure (P).

All equations relating variables to parameters characterizing mechanical properties were characterized with linear relationships, consistent with the previously-reported models (49). To maintain simplicity, the pulmonary and systemic vasculatures were characterized by minimal components consisting of peripheral resistances and

arterial and venous compliances. Cardiac ventricles were characterized by maximum and minimum elastances of the time-varying elastance model (254). Blood volume (V_B) was assumed to be stored only in systemic and pulmonary arterial and venous compartments. Because systemic interstitial edema is generally not critical to survival in heart failure (35) and has no significant effect on pulmonary edema when systemic mean arterial pressure (P_{sa}) is regulated, we only included the pulmonary interstitial space. For the purpose of simplicity, we assumed the pulmonary interstitium to be characterized by a single compartment.

Blood circulation model equations. The cardiovascular model was characterized previously in Section 2.2, with a full set of model equations in *Appendix C* (*Eqs. C1-C10*). Minor modifications made to *Eqs. C1* and *C3* to introduce a pulmonary capillary pressure that serves as a critical junction with the pulmonary interstitium. Specifically, the difference in pulmonary arterial pressure (P_{pa}) and pulmonary capillary pressure (P_{cp}) divided by pulmonary arterial resistance (R_{pa}) determines flow from the pulmonary arterial compartment (Q),

$$\frac{P_{pa}-P_{cp}}{R_{pa}} = Q. \qquad (11)$$

Similarly, the difference in pulmonary capillary pressure (P_{cp}) and pulmonary venous pressure (P_{pv}) divided by pulmonary venous resistance (R_{pv}) determines flow to the pulmonary venous compartment (Q),

$$\frac{P_{cp}-P_{pv}}{R_{pv}} = Q. \qquad (12)$$

To maintain simplicity, further simplifying assumptions were made. Although pulmonary lymphatic flow (Q_{ip}) contributes to cardiac output (Q), Q_{ip} was assumed to be negligible. A correction factor (κ) relating end-systolic pressures to mean systemic arterial pressures was assumed to be equal to unity (256).

Interstitial fluid balance model equations. Microvascular fluid balance was characterized with an analytical description developed by Dongaonkar et al. (49) and reproduced in *Appendix C* (*Eqs. C12-C14*). Briefly, microvascular flow out of the pulmonary capillaries (treated as a single compartment) is characterized by the Starling-Landis Equation,

$$Q_{mp} = K_{fp}\left[\left(P_{cp} - P_{ip}\right) - \Delta\Pi_p\right], \tag{13}$$

where Q_{mp} is the pulmonary microvascular filtration, K_{fp} is the pulmonary microvascular filtration coefficient, and $\Delta\Pi_p$ is the capillary-interstitial oncotic pressure difference. Pulmonary capillary pressure (P_{cp}) and interstitial pressure (P_{ip}) are assumed to be variables. Pulmonary lymphatic flow (Q_{lp}) was characterized by the Drake-Laine Equation (130),

$$Q_{lp} = \frac{P_{ip}+P_{pp}-P_{sv}}{R_{lp}}, \tag{14}$$

with P_{pp} defined as the effective pulmonary lymphatic pump pressure and R_{lp} as effective pulmonary lymphatic resistance. In equilibrium, lymphatic flow was assumed to be equal to microvascular flow, which in turn is equal to total pulmonary interstitial flow (Q_{ip}),

$$Q_{ip} = Q_{mp} = Q_{lp}. \tag{15}$$

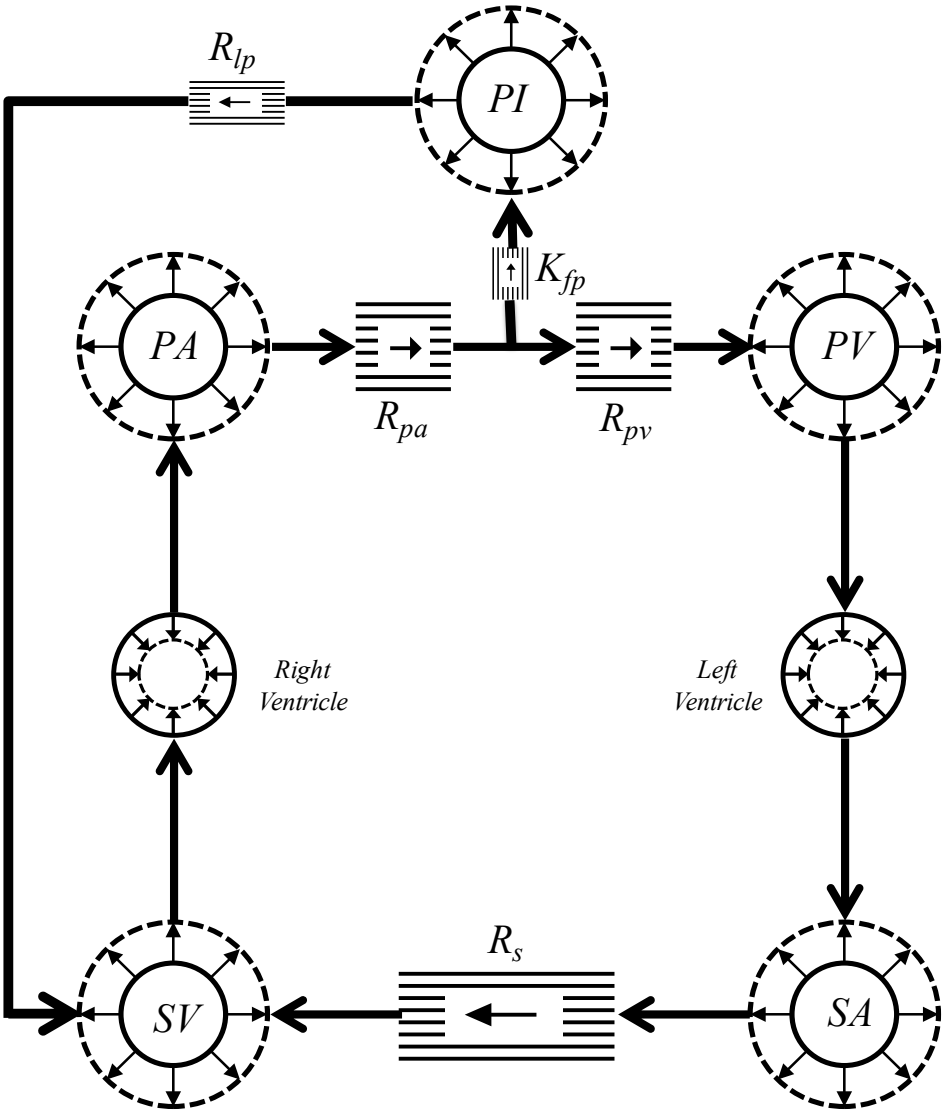

Figure 7. Lumped description of the coupled vascular and pulmonary interstitial compartments. Pulmonary arteries (*PA*), pulmonary veins (*PV*), systemic arteries (*SA*), and systemic veins (*SV*) are each represented with a compliant chamber (dotted circle) and resistance (box). The right and left ventricles are represented by a time-varying elastance. The pulmonary interstitial compartment (*PI*) is characterized by a compliant chamber (dotted circle), an effective lymphatic resistance (R_{lp}) and a microvascular permeability coefficient (K_{fp}).

Solutions for integrated model equations with regulated systemic arterial pressure. Figure 7 represents coupling of the cardiovascular and pulmonary interstitial models. In addition to these standard model equations, it was assumed that total extracellular fluid volume (V) of the integrated model was the sum of blood volume (V_B) and pulmonary interstitial volume (V_{ip}),

$$V = V_B + V_{ip}. \tag{16}$$

The variable V does not include systemic interstitial fluid volumes. The entire integrated model (Fig. 7) can thus characterized by a system of fifteen simplified linear equations (*Eqs. C1-C15*). Since renal regulation of blood volume controls systemic arterial pressure over the course of hours or days, a critical modeling choice was made to treat P_{sa} as a constant parameter and blood and interstitial volumes as variables. *Equations C1-C15* were thus solved simultaneously for nine variables (P_{pv}, P_{sv}, P_{pa}, Q, V, V_{ip}, V_B, P_{ip}, and Q_{ip}).

Characterizing cardiac output in terms of balance points to yield equilibrium values of pulmonary capillary pressure and systemic venous pressures. Although the system of equations characterized by *Eqs. C1-C10* can be solved algebraically for pulmonary capillary pressure, they can also be expressed graphically as a novel balance point. To achieve this, it was necessary to characterize blood flow with two components, much like Guyton's cardiac output and venous return (81). In this case, cardiac output is expressed as one flow through the right ventricle (Q_{rv}) and one through the left ventricle (Q_{lv}). The flow through the right ventricle (Q_{rv}) included flow from the entrance of the systemic vasculature, through the right ventricle and pulmonary arterial system to the

pulmonary capillaries. The governing equations for these elements (*Eqs. C1, C2, C9*) were simultaneously solved for Q, P_{pa}, and P_{sv}. Systemic arterial pressure (P_{sa}) was assumed constant, causing the interstitial compartments to be irrelevant to the solutions. As a result, Q_{rv} was expressed as a function of constant parameters of the right ventricle, pulmonary arterial resistance, and pulmonary capillary pressure (P_{cp}). To plot Q_{rv} versus P_{cp}, the slope of the resulting relationship was found by taking the derivative with respect to P_{cp}, and the abscissa intercept found by setting Q_{rv} equal to zero and solving for P_{cp}. The flow through the left ventricle (Q_{lv}) included flow from the pulmonary capillaries through the pulmonary veins and left ventricle. The governing equations for these elements (*Eqs. C3* and *C8*) were simultaneously solved for Q_{lv} and P_{pv}, also assuming constant systemic arterial pressure (P_{sa}). To plot Q_{lv} versus P_{cp}, the slopes and intercepts were likewise calculated. Both Q_{rv} and Q_{lv} were plotted on the same graph. The intercept represents equilibrium where Q_{rv}=Q_{lv}, indicating the equilibrium value of pulmonary capillary pressure (P_{cp}^{*}). For comparison purposes, the cardiac output-venous return balance point graph from Fig. 3 was also reproduced, indicating the equilibrium value of systemic venous pressure (P_{sv}^{*}). Likewise, the interstitial fluid balance point of Dongaonkar et al. (49) was reproduced from *Eqs. 13-15*, with intercepts expressed in terms of equilibrium values of P_{cp}^{*} and P_{sv}^{*}.

Non-dimensionalization of parameters to allow generalization. To further simplify the equations to obtain an analytical form amenable to characterizing different mammals, parameters were rearranged into non-dimensional groups (i.e., the model was "re-parameterized"). When possible, these terms were formed into recognized allometric

invariants (i.e., ratios that are nearly constant across different mammalian species). For example, the ratio of end-systolic and end-diastolic cardiac elastances (i.e., E_{max}/E_{min}) is independent of mammalian weight (287), as is the ratio of effective arterial elastance to end-systolic elastance (i.e., $HR\ R_s/E_{max}$), used as an index of ventricular-arterial coupling (23). Five sets of parameters were obtained and reformulated in these nondimensional parameter groups. The first two parameter sets included a complete set of parameters for 20 kg dogs for both normal and heart failure with reduced ejection fraction (HFrEF). Measurements of parameters governing human pulmonary interstitial fluid balance are more limited. Cardiovascular parameters for a 70 kg human were obtained from Table 1 for normal, heart failure with reduced ejection fraction (HFrEF), and heart failure with preserved ejection fraction (HFpEF) phenotypes. Because inadequate parameter measurements of the interstitium in humans exist, missing parameters were in general assumed to be similar to measurements made in animal models. A detailed description of parameters used can be found in *Appendix D*.

Primary determinants of pulmonary interstitial pressures in the coupled circulatory system. Primary mechanical determinants of pulmonary interstitial pressure were found by performing a standard sensitivity analysis and simplifying equations. First, the sensitivity of normal human pulmonary interstitial pressure to individual model parameters were quantified and graphed. The sensitivity was found by changing each parameter ±10%, and then taking the absolute value of the maximum change in P_{ip} from the original value, dividing by the original value of P_{ip} and multiplying by 100. Relative sensitivity was then found by calculating the sensitivity index (SI) for all parameters

which quantifies the change in P_{ip}. The change in P_{ip} (ΔP_i) as each parameter varied by 10% was divided by the sum of the change in all parameters to provide a representation of each parameters relative contribution to the change in P_{ip},

$$SI = \frac{\Delta P_i}{\sum_i^n \Delta P_i} * 100. \quad (17)$$

This process was repeated for each of the three human parameter sets (Normal, HFrEF, and HFpEF). The same process was used to tabulate the relative sensitivity of human pulmonary interstitial pressure to changes in nondimensional parameter groups, for normal, HFrEF and HFpEF cases. The piecewise linear relationship for end-diastolic pressure-volume relationships were neglected to simplify analysis.

Approximating algebraic formulas for human pulmonary interstitial pressure for normal and heart failure phenotypes. The algebraic solution for equilibrium pulmonary interstitial pressure was reformulated as a function of nondimensional model parameters. Terms contributing less than 15% to P_{ip} were removed from both the dimensional and nondimensional forms of the equation for equilibrium P_{ip}. Because the values for human differed for normal, HFrEF and HFpEF cases, three separate approximations emerged.

Effect of left relative contractility on pulmonary interstitial pressure. Assuming all other parameters constant and equal to normal values for human, pulmonary interstitial pressure was graphed as a function of the ratio of end-systolic elastance and end-diastolic elastance (E_{maxlv}/E_{minlv}). To illustrate the effect of E_{maxlv}/E_{minlv} in a subject with increased microvascular permeability, pulmonary interstitial pressure was also graphed with K_{fp} increased by a factor of four. Ranges of E_{maxlv}/E_{minlv} corresponding to HFrEF were indicated on the graph.

Effect of non-dimensional parameters on volumes. To illustrate how relative blood and interstitial volumes redistribute as properties of the system altered, the ratios V_{ip}/V and V_B/V were graphed as a function of P_{sa}, as well as the nondimensional groups E_{maxlv}/E_{minlv} and $K_{fp}R_{lp}$.

Validation. All pressures, flows, and volumes were compared to measured physiological values for two canine phenotypes (normal, HFrEF). Since limited measurements of pulmonary interstitial pressure and volume exist for humans, human phenotypes (normal, HFrEF, and HFpEF) were compared solely to measured vascular pressures and flows. To more accurately simulate volume shifts and pressures changes, heart failure phenotypes were assumed to be in chronic compensated heart failure without volume management.

3.3 Results

Graphical representation of cardiac output and pulmonary capillary pressure. Figure 8A represents the interaction of cardiac output through the right ventricle (Q_{rv}), with,

Q_{lv} slope: $\frac{HR}{E_{minlv}+R_{pv}HR}$, (*18*)

and,

Q_{lv} intercept: $\frac{E_{minlv}}{E_{maxlv}}(P_{sa} - E_{maxlv}\Delta V_{olv})$. (*19*)

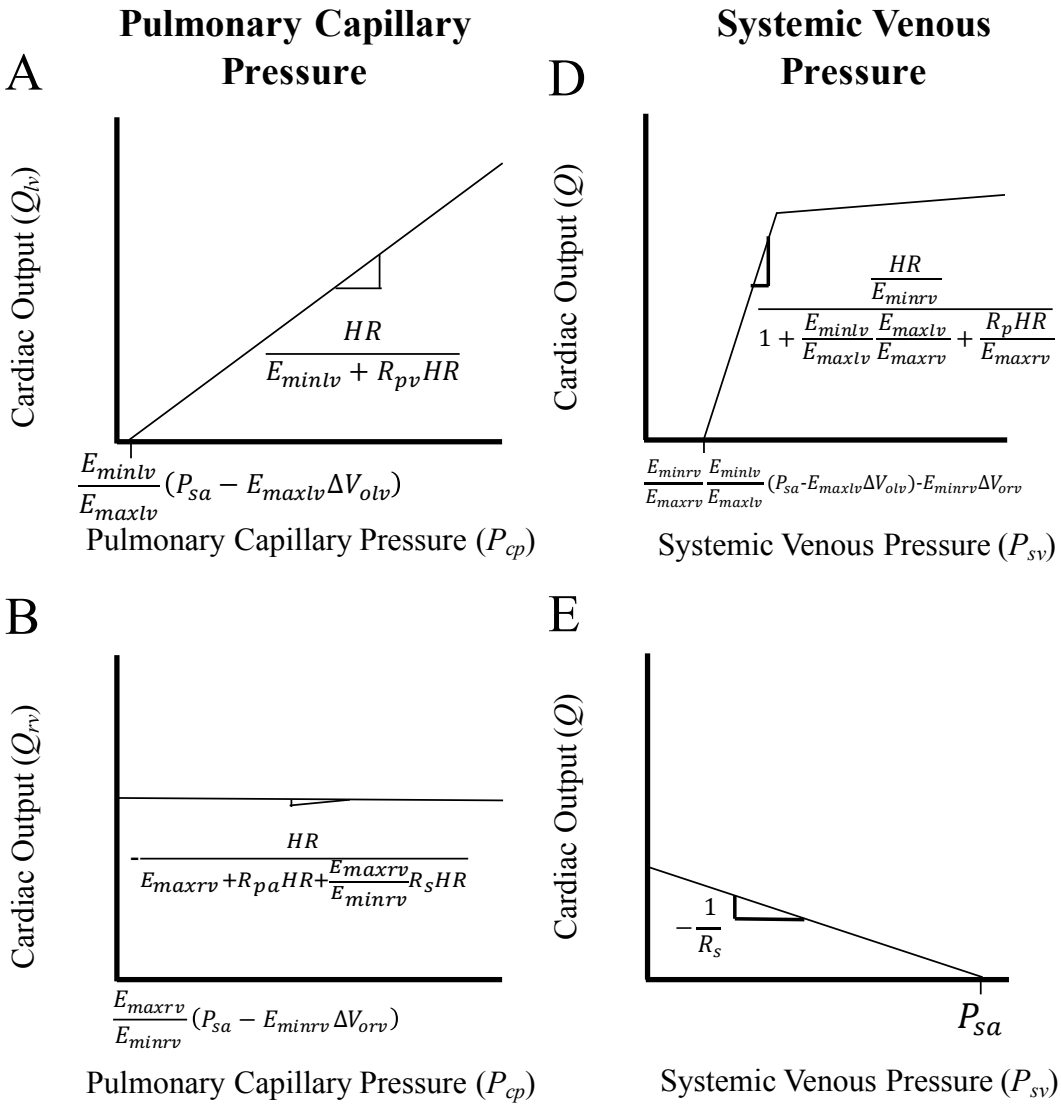

Figure 8. Equilibrium pulmonary capillary pressure (P_{cp}) and systemic venous pressure (P_{sv}) both arise from the balance of input and output flows. Slopes and intercepts determining the relationship of the variables are indicated on the graphs (*Eqs. 18-21*). Flow from the left ventricle (Q_{lv}) increases as P_{cp} increases (A). Flow from the right ventricle (Q_{rv}) decreases as P_{cp} increases (B). The balance of the two determines equilibrium Q and P_{cp} (C). Similarly, as P_{sv} increases, Q through the heart and pulmonary vasculature increases (D), while increases in P_{sv} cause a decrease in Q through the systemic vasculature (E). Equilibrium Q and P_{sv} are determined by the balance of those two opposing forces, cardiac output (CO) and venous return (VR) (F).

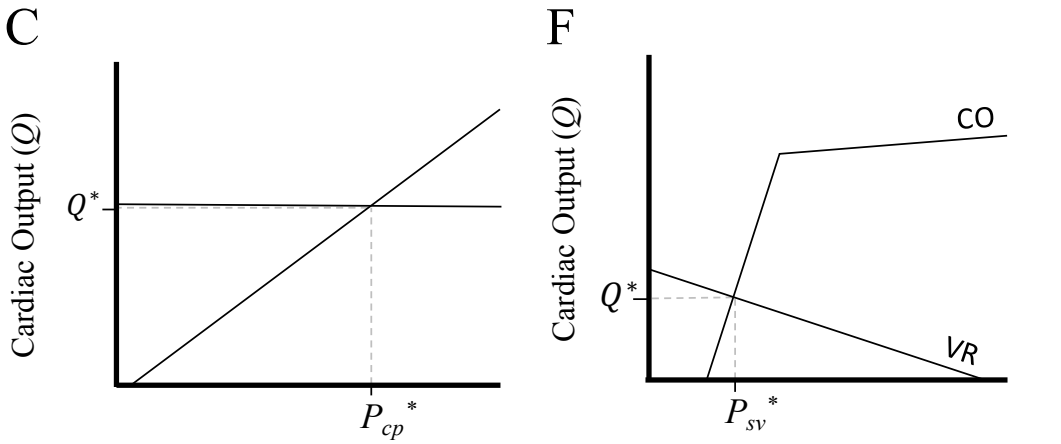

Figure 8. Continued.

Figure 8B illustrates the cardiac output through the left ventricle (Q_{lv}), with,

Q_{rv} slope: $-\frac{HR}{E_{maxrv}+R_{pa}HR+\frac{E_{maxrv}}{E_{minrv}}R_sHR}$, (*20*)

and,

Q_{rv} intercept: $\frac{E_{maxrv}}{E_{minrv}}(P_{sa}-E_{minrv}\Delta V_{orv})$. (*21*)

Figure 8C plots both Q_{rv} and Q_{lv} simultaneously, with the intersection representing equilibrium cardiac output (Q^*) and pulmonary capillary pressure (P_{cp}^*). Figures 8D-F illustrate Guyton's cardiac output (*CO*) and venous return (*VR*) balance point reformulated for chronic conditions when P_{sa} is regulated and blood volume is variable. Pulmonary resistance (R_p) is the sum of pulmonary arterial (R_{pa}) and pulmonary venous resistance (R_{pv}). The intersection represents equilibrium cardiac output (Q^*) and systemic venous pressure (P_{sv}^*). Figure 9 illustrates the interstitial fluid balance point, with intercepts expressed in terms of P_{cp}^* and P_{sv}^* (dashed boxes).

Solutions for equilibrium pulmonary capillary pressure (P_{cp}^*) and systemic venous pressure (P_{sv}^*). Equilibrium pulmonary capillary pressure (P_{cp}^*) can be represented with a combination of circulatory parameters,

$$P_{cp}^* = \frac{P_{sa}\left(E_{maxrv}+E_{minlv}+HR\,(R_{pa}+R_{pv})\right)+\frac{R_S HR}{E_{maxlv}}(E_{minlv}P_{sa})+R_S HR(E_{minlv}\Delta V_{olv}+E_{maxrv}\Delta V_{orv})}{E_{minlv}+E_{maxlv}+(R_{pa}+R_{pv})HR+\frac{E_{maxrv}R_S HR}{E_{minrv}}} \quad (22)$$

Equilibrium systemic venous pressure (P_{sv}^*) can similarly be represented,

$$P_{sv}^* = \frac{P_{sa}\left(E_{maxrv}+E_{minlv}+HR\,R_p-\frac{HR\,R_S E_{minlv}}{E_{maxlv}}\right)+HRR_S(E_{minlv}\Delta V_{olv}+E_{maxrv}\Delta V_{orv})}{E_{minlv}+E_{maxlv}+R_p HR+\frac{E_{maxrv}R_S HR}{E_{minrv}}}. \quad (23)$$

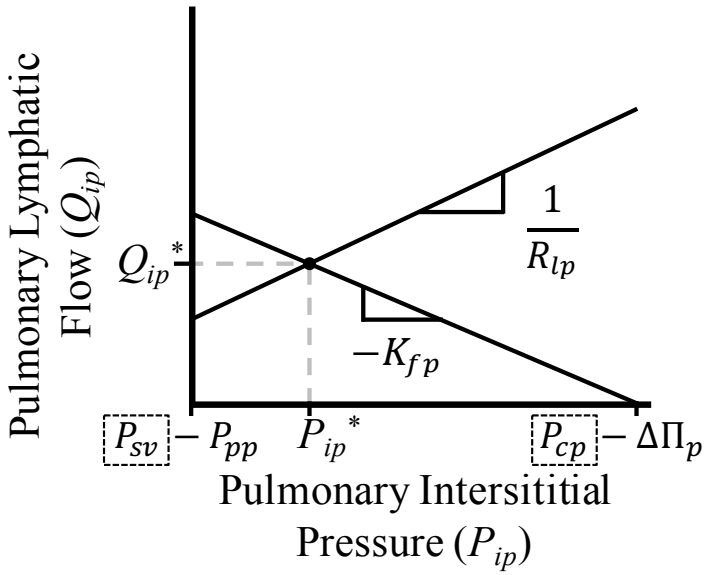

Figure 9. Pulmonary interstitial pressure (P_{ip}) arises from the balance of flow into the interstitium characterized by the Starling-Landis equation (*Eq. 13*) and flow out of the interstitium characterized by the Drake-Laine equation (*Eq. 14*), with the vascular space influencing interstitial pressure through systemic venous pressure (P_{sv}) and pulmonary capillary pressure (P_{cp}). Figure is consistent with Dongaonkar et al. (49), with parameters matching those in the present work for the pulmonary interstitium.

Analytical solution for pulmonary interstitial pressure in terms of vascular parameters. As illustrated in Fig. 9, although pulmonary interstitial pressure (P_{ip}) can be calculated solely from interstitial parameters by assuming constant values of systemic venous pressure (P_{sv}^{*}) and pulmonary capillary pressure (P_{cp}^{*}), these two pressures play a large role in pulmonary interstitial pressure (17.56% as determined by relative sensitivity analysis). Solving the system of equations (*Eqs. C1-C15*), yields pulmonary interstitial pressure (P_{ip}) expressed as a combination of vascular and interstitial mechanical parameters. Alternatively, P_{ip} can be expressed in terms of P_{cp}^{*} and P_{sv}^{*} from *Eqs. 22* and *23*,

$$P_{ip} = \frac{P_{sv}^{*} + R_{lp}(\Delta\Pi_p + P_{pp} + P_{cp}^{*} K_{fp})}{1 + R_{lp} K_{fp}}. \quad (24)$$

Sensitivity analysis. Figure 10 indicates that while P_{ip} is most sensitive to changes in interstitial parameters P_{pp}, K_{fp}, R_{lp}, and $\Delta\Pi_p$ in normal conditions, vascular parameters P_{sa}, R_s, HR, E_{minlv}, ΔV_{lv}, and E_{maxlv} also play a large role. Other parameters, including pulmonary arterial and venous resistance and right ventricular parameters, have less than a 5% effect on changes in pulmonary interstitial pressure.

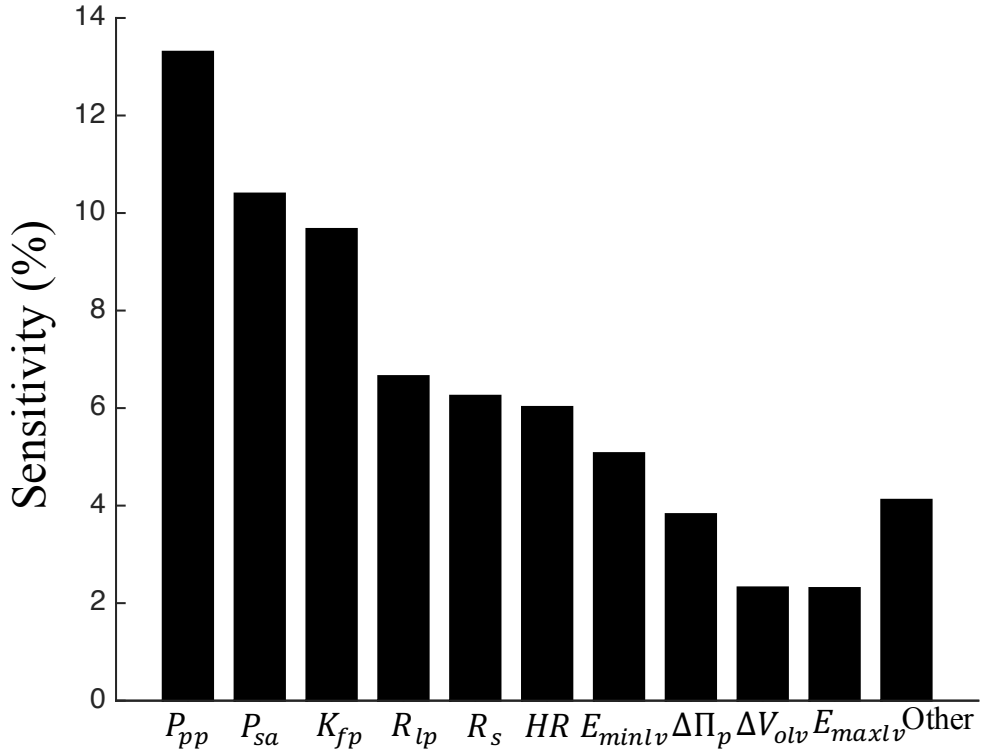

Figure 10. Sensitivity analysis of pulmonary interstitial pressure (P_{ip}) for normal human parameters. While P_{ip} depends on interstitial parameters (P_{pp}, K_{fp}, R_{lp}, $\Delta\Pi_p$), it is also very sensitive to changes in cardiovascular parameters (P_{sa}, R_s, HR, E_{minlv}, ΔV_{lv}, E_{maxlv}). Notably, pulmonary arterial and venous resistance do not play a large role. Parameters contributing less than 3% to the sensitivity were combined in "Other".

Non-dimensional Terms	Parameters	Relative Sensitivity (%)			M	Effect of increase
		Normal	HFrEF	HFpEF		
J_{pn}	$\frac{P_{pp}}{P_{sa}}$	35.43	37.50	21.42	P	↓
R_i	$K_{fp}R_{lp}$	16.03	17.51	18.69	P	↑
o_p	$\frac{\Delta\Pi_p}{P_{sa}}$	10.20	10.80	6.17	P	↓
C_{pn}	$\frac{C_p}{C_{tot}}$	0	0	0	P	-
P_{tf}	$\frac{V - V_{otot}}{C_{tot}P_{sa}}$	0	0	0	N	-
EE_{lv}	$\frac{E_{maxlv}}{E_{minlv}}$	12.30	12.99	24.23	M	↓
E_{alv}	$\frac{R_sHR}{E_{maxlv}}$	6.15	2.60	6.99	M	↓
Q_{ol}	$\frac{R_{sa}HR\Delta V_{lv}}{P_{sa}}$	6.18	3.09	14.56	P	↓
EE_{rv}	$\frac{E_{maxrv}}{E_{minrv}}$	3.83	4.19	2.50	P	↓
E_{arv}	$\frac{R_{pa}HR}{E_{maxrv}}$	2.54	2.24	0.57	M	↓
Q_{or}	$\frac{R_{pa}HR\Delta V_{rv}}{P_{sa}}$	2.51	2.71	1.30	P	↓

Figure 11. Non-dimensional parameters' effect on pulmonary interstitial pressure. Non-dimensional terms are composed of a combination of cardiovascular and interstitial parameters (Parameters). Relative sensitivities of the non-dimensional parameters for each of the three human phenotypes (Normal, HFrEF, and HFpEF) are illustrated. Normal and HRrEF conditions are largely influenced by changes in normalized lymphatic pumping pressure (J_{pn}) and interstitial resistances (R_i), while left ventricular properties (EE_{lv}) play a larger role in HFpEF. Whether measured parameter values exist for each term (M) was indicated with as measured (M), partially measured (P) for terms composed of both measured parameters and parameters with very few measurements, or not measured (N). The effect on P_{ip} of an increase in each term is indicated as either an increase (↑), decrease (↓), or no effect (-). Compliances and volumes were simplified with combined total compliance ($C_{tot} = C_{sa} + C_{sv} + C_{pa} + C_{pv} + C_p$) and total unstressed volume ($V_{otot} = V_{osa} + V_{osv} + V_{opa} + V_{opv} + V_{op}$).

Non-dimensional Terms	Parameters	Relative Sensitivity (%)			M	Effect of increase
		Normal	HFrEF	HFpEF		
R_a	$\frac{R_{pa}}{R_s}$	3.38	3.63	1.41	M	↑
R_v	$\frac{R_{pv}}{R_s}$	1.44	2.71	2.17	M	↑
C_{san}	$\frac{C_{sa}}{C_{tot}}$	0	0	0	P	-
C_{svn}	$\frac{C_{sv}}{C_{tot}}$	0	0	0	P	-
C_{pan}	$\frac{C_{pa}}{C_{tot}}$	0	0	0	P	-
C_{pvn}	$\frac{C_{pv}}{C_{tot}}$	0	0	0	P	-

Figure 11. Continued.

Primary determinants of pulmonary interstitial pressure. Figure 11 illustrates that pulmonary interstitial pressure is very sensitive to normalized lymphatic pumping pressure (P_{pp}/P_{sa}) for both the normal and HFrEF cases. For the HFpEF case, a more balanced contribution amongst parameters is apparent, with relative ventricular contractility EE_{lv} (i.e., E_{maxlv}/E_{minlv}) having the greatest effect on pulmonary interstitial pressure and J_{pn} (i.e., P_{pp}/P_{sa}) and Δo_{pn} (i.e., $-\Delta\Pi_p/P_{sa}$) each contributing more than 15% to changes in P_{ip}. These three terms comprise 75% of the relative sensitivities. Compliances, total filling pressure, and unstressed volumes of the heart play either little or no role in determining P_{ip} in chronic conditions. Normal and HFrEF conditions are largely influenced by lymphatic pumping pressure, interstitial resistances, and left

ventricular properties. However, while HFpEF is influenced by the same three parameters, left ventricular properties have a much larger effect on P_{ip}.

Pulmonary interstitial pressure can be predicted in terms of non-dimensional parameters. Approximating pulmonary interstitial pressure for the normal case ($P_{ip,norm}$) decreases the degrees of freedom (i.e., total number of independent parameters) from 22 to 17 when P_{ip} is expressed in terms of non-dimensional parameters and insignificant terms are removed. Non-dimensional parameters include four ratios previously acknowledged as non-dimensional ($R_{pa}HR/E_{maxrv}$, R_sHR/E_{maxlv}, E_{maxlv}/E_{minlv}, E_{maxrv}/E_{minrv}) (257, 287). Decreased dependence on interstitial parameters and pulmonary parameters is apparent, with an absence of interstitial osmotic pressure (Δo_{pn}) and pulmonary venous resistance (R_{vn}). In addition, normalized unstressed volumes of the ventricles (ΔV_{lvn}, ΔV_{rvn}) are absent,

$$P_{ip,norm} \approx \frac{E_{arv}EE_{rv}\left(E_{alv}EE_{lv}J_{pn}+R_i\right)}{(1+R_i)(E_{alv}EE_{lv}R_a+E_{arv}EE_{lv}E_{alv}EE_{rv})}. \quad (25)$$

Applying the same simplification to pulmonary interstitial pressure for the heart failure phenotypes, we obtain a different approximation for HFrEF,

$$P_{ip,HFrEF} \approx \frac{E_{arv}EE_{rv}E_{alv}\left(-EE_{lv}J_{pn}+R_i+EE_{lv}R_i\Delta o_{pn}\right)}{(1+R_i)(E_{arv}EE_{rv}EE_{lv}+R_aEE_{lv})}, \quad (26)$$

and for HFpEF,

$$P_{ip,HFpEF} \approx \frac{E_{alv}EE_{lv}R_i(E_{arv}EE_{rv}R_a+\Delta V_{oln})}{(1+R_i)(E_{alv}E_{arv}EE_{lv}EE_{rv}+E_{alv}EE_{lv}R_a)}. \quad (27)$$

While the solutions are similar to the normal condition, HFrEF is influenced by normalized interstitial osmotic pressure (Δo_{pn}), which not present in the normal case, and HFpEF is influenced by unstressed left ventricular volume (ΔV_{olvn}) and no longer

significantly influenced by lymphatic pumping pressure (J_{pn}). Each of the three approximations (*Eqs. 25-27*) differed by less than 32% from the full solution characterized by *Eqs. 22-24*.

Influence of left ventricular elastance ratio on pulmonary interstitial pressure. Pulmonary interstitial pressure changes from -6.76 to -4.32 as the left ventricular heart elastance ratio (EE_{lv}) decreases from normal to HFrEF conditions, even in the absence of any changes in interstitial or other vascular parameters (Fig. 12). Although initially the rate of change is smaller, as EE_{lv} decreases, pulmonary interstitial pressure becomes much more sensitive to changes. A fourfold increase in K_{fp} increases pulmonary interstitial pressure to close to zero, although as heart failure worsens, EE_{lv} has little effect on P_{ip}. Similar behavior is evident with increases in R_{lp} (not shown).

Influence of systemic arterial pressure, relative ventricular elastance ratio, and normalized interstitial pump pressure on interstitial and blood volumes. As systemic arterial pressure (P_{sa}) increases, volume is increased in the blood compartment and decreased in the interstitial compartment for both the normal and HFrEF phenotypes. With HFpEF, blood volume shifts to the interstitial compartment with increase in P_{sa} (Fig. 13A). With normal heart function, a change in the left ventricular ratio (EE_{lv}) has little effect on volume distribution. As heart failure progresses, volumes shifts to the interstitial compartment (Fig. 13B). As R_i (i.e., $R_{lp}K_{fp}$) increases, the interstitial volume increases and blood volume decreases for all phenotypes. However, an increase in R_i has a larger effect on the HFpEF phenotype (Fig. 13C).

Validation. All variables were found within normal measured ranges (Table 3, Table 4) for both normal and heart failure conditions.

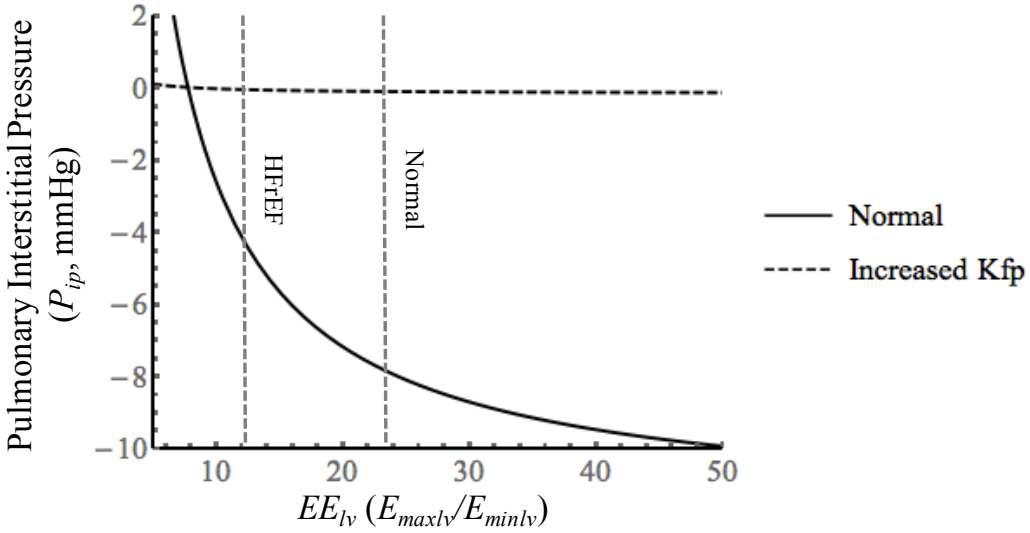

Figure 12. Pulmonary interstitial pressure (P_{ip}) is very sensitive to changes in ventricular properties, even in the absence of any changes in interstitial parameters. As heart failure progresses (illustrated with values for HFrEF), P_{ip} increases. With a fourfold increase in the pulmonary microvascular coefficient (K_{fp}), P_{ip} increases to near zero pressure, but becomes much less sensitive to changes in left ventricular elastances.

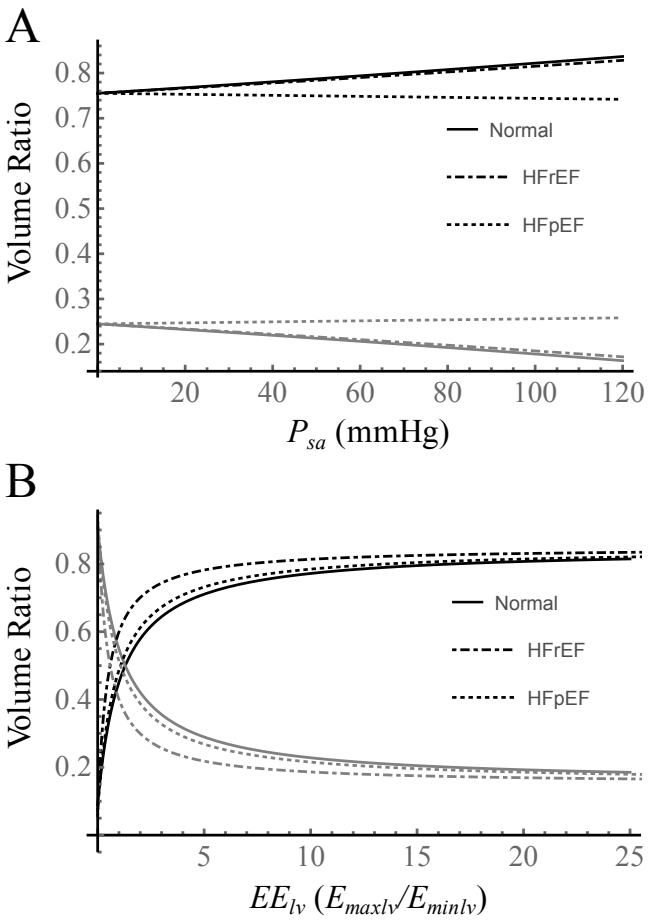

Figure 13. The interstitial volume ratio (V_{ip}/V, gray) and blood volume ratio (V_B/V, black) characterizes the change in distribution of total volume to the interstitial and blood compartments. A) As systemic arterial pressure (P_{sa}) increases, more volume is distributed to the blood compartment and less to interstitial compartment for both the normal and HFrEF phenotypes. However, with HFpEF, volume distributed to the interstitial compartment increases. B) At normal values, a change in the left ventricular ratio (EE_{lv}) has little effect on volume distribution. With lower values of EE_{lv} with progression of heart failure, fluid volume shifts to the interstitium. C) With a twofold increase in the pulmonary interstitial resistance ratio (R_i), the interstitial volume ratio increases and blood volume decreases for all phenotypes, but an increase in R_i has a larger effect on the HFpEF phenotype.

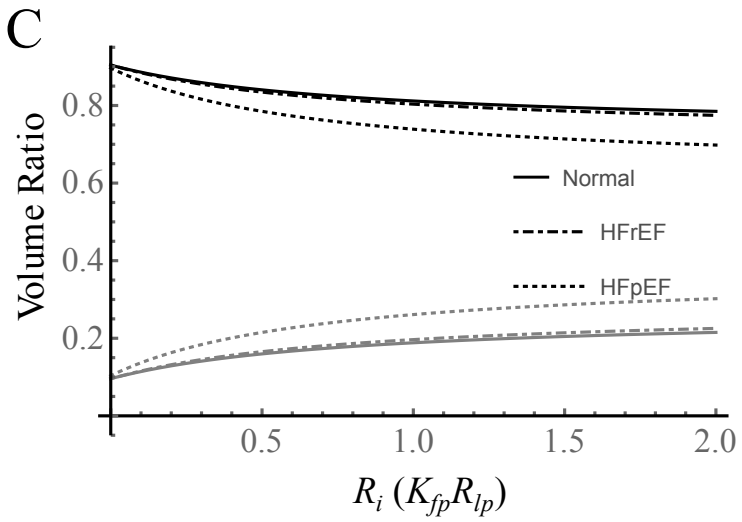

Figure 13. Continued.

20 kg dog	**Normal**			**HFrEF**		
Vascular	Sim	M	Ref	Sim	M	Ref
Q (mL/s)	36.72	41.67-66.67	(97)	21.73	18.67-22.2	(290)
P_{sv} (mmHg)	2.68	0-7.36	(97)	9.29	9-13	(290)
P_{pa} (mmHg)	16.01	10-20	(97)	44.98	36±7	(5)
P_{pv} (mmHg)	3.16	5-12	(97)	33.58	26±8	(290)
V_B (mL)	1993.06	1926.94±88	(184)	2314.24	1347-2360	(184, 281)
Interstitial	Sim	M	Ref	Sim	M	Ref
P_{ip} (mmHg)	-1.68	-2.2- -1.58	(49, 266)	-1.39	-1.67±0.97	(266)
V_{ip} (mL)	689.79	569.85±8.7	(265)	791.53	781.55±17.4	(265)

Table 3. Predicted hemodynamic values fall within (or near) range for reported values (M) for a 20 kg dog. The assumed values for systemic arterial pressure (P_{sa}) for Normal and heart failure with reduced ejection fraction (HFrEF) phenotypes were 100 and 96.4 mmHg to match reported mean values.

70kg human	Normal			HFrEF			HFpEF		
Vascular	Sim	M	Ref	Sim	M	Ref	Sim	M	Ref
Q (mL/s)	80.58	67-133	(277)	71.05	80±23	(57)	74.47	86.67 ±22	(57)
P_{sv} (mmHg)	4.90	0-6	(277)	8.35	7.4±15	(57)	13.59	9.6 ±4.2	(57)
P_{pa} (mmHg)	14.84	10-20	(277)	21.49	28±11	(57)	39.80	34±17	(57)
P_{pv} (mmHg)	7.59	6-12	(277)	9.13	16±7	(57)	23.27	19±9	(57)
V_B (mL)	5221.77	5172-5321.62	(207, 216)	5038.2	5179 ±424	(40)	5685.05	4696 ±1137	(181)

Table 4. Predicted vascular parameters (Sim) fall within range of previously-reported values (M) for a 70 kg human. Predicted values compared to reported values for normal subjects (207, 216, 248, 277) subjects with heart failure reduced ejection fraction (HFrEF) (57), preserved ejection fraction (HFpEF) (57). Calculated Normal pulmonary interstitial pressures (P_{ip}) also fell within range of reported values (-6.76 mmHg; reported -8 to -2 mmHg (95, 248)). The assumed values for systemic arterial pressure for Normal, HFrEF and HFpEF were 90, 87, and 103 mmHg, respectively, to match reported mean values. Parameter values used for validation are illustrated in Table D1.

3.4 Discussion

The present work developed general algebraic predictions of pulmonary interstitial pressure which can be applied to chronic conditions. We developed an algebraic formula from two models (49) that explicitly relates pulmonary interstitial pressure (P_{ip}) to the mechanical properties of the cardiovascular system. Furthermore, by taking the novel approach of assuming systemic arterial pressure (P_{sa}) is regulated and that extracellular volume (V) is variable, the solution is appropriate to predict chronic $P_{ip.}$ To derive an algebraic solution, we used three simplifying assumptions: 1) minimal compartment models, 2) linearized model equations, and 3) regulated systemic arterial pressure is a constant parameter. Each set of assumptions introduced error into our

approximations for P_{ip}, as well as limiting the context in which the model applies. Nonetheless, our model achieved adequate approximations for measured P_{ip} in both human and animal models. Given the limitations of current knowledge of parameter values, we nonetheless could identify the primary determinants of pulmonary interstitial pressure, including effective lymphatic pump pressure, oncotic pressure gradients across the pulmonary capillaries, and the ratio of end systolic and end-diastolic left ventricular elastances. Given the complexity of the full formula for P_{ip}, we took three approaches to better conceptualize its relationship of the mechanical properties of the system. First, we integrated three balance point graphs that yield equilibrium pulmonary capillary pressure (Fig. 8C), systemic venous pressure (Fig. 8F), and ultimately pulmonary interstitial pressure (Fig. 9). Second, we "reparameterized" the model, forming a smaller set of non-dimensional ratios that for the most part are recognized allometric invariants (nondimensional terms that are relatively constant across different mammalian species). With interstitial measurements limited in humans (289), such algebraic formulas facilitate research performed on specific animal models to be translated to clinically-relevant human research. Third, we further simplified by removing less significant terms from the general solution for P_{ip} which yielded different approximations for P_{ip} for normal subjects ($P_{ip,norm}$, *Eq. 25*), subjects with heart failure with reduced ejection fraction ($P_{ip,HFrEF}$, *Eq. 26*), and subjects with heart failure and preserved ejection fraction ($P_{ip,HFrEF}$, *Eq. 27*). This approach reveals that although interstitial fluid balance parameters dominate P_{ip}, different vascular and cardiac properties play critical roles in

the different heart failure phenotypes. Most importantly, this work helps clarify which of the many parameters merit focus of future clinically-relevant research.

Algebraic solutions enable characterization of the interaction of subsystems. Mathematical characterization of a physiological system requires a model complex enough to represent critical system behavior, yet simple enough to interpret the results (38). Although foundational equations, such as Starling-Landis, tend to be simple algebraic characterizations, complexity of reported mathematical models have increased as computational tools have become more powerful. Emergent behaviors of integrated models have been able simulate fluid and pressure shifts in the pulmonary system (33, 83, 91, 94, 152, 216, 257). Such complex models have generated critical knowledge, such as the insight that regulation of blood volume controls chronic systemic blood pressure (82) and lymphatic return plays a critical role in fluid balance (55). However, previous models were limited by focus on a specific population characterized by a specific set of parameter values, some of which included potentially extraneous mechanisms (216). Because conventional computational models have required numerical solution, all parameters must be assigned specific values (216), even if they have never been measured or have only been estimated (see Fig. 11). In addition, many characterizations of interstitial fluid balance have been incomplete, with the lymphatic system either absent (94) or characterized without active lymphatic pumping (33, 91, 216). Even with critical simplifications, our model incorporates parameters for the active transport of lymph. Our approach to modeling included arranging parameters into nondimensional groups that are relatively constant across animal species, increasing the

ability to synthesize information from multiple animal experiments. Such groupings of parameters were a specific outcome of solving model equations algebraically. Another consequence of deriving algebraic solutions is to identify parameter groups that are functionally coupled, such as E_{max}/E_{min}, $K_{fp}R_{lp}$, and R_sHR/E_{max}, that not only explicitly illustrate parameter interaction, but also have functional interpretations. For instance, E_{max}/E_{min} is a relative ventricular contractility that characterizes the ability to pump blood (287); $K_{fp}R_{lp}$ is the resistance to fluid movement out of the interstitium relative to resistance to flow into the interstitium that characterizes the potential to form edema (49); and R_sHR/E_{max} is the putative ratio of effective arterial elastance to ventricular elastance that characterizes ventricular-arterial system coupling in terms of stroke work (165). On a broader scale, combining the cardiovascular system with the pulmonary interstitial compartment yields synergistic parameter sets such as $EE_{lv} \cdot J_{pn}$ in *Eq. 26* that suggests synergy between relative cardiac contractility and relative lymphatic pumping reduces P_{ip} in HFrEF patients. By focusing on breadth and completeness, rather than depth and accuracy, our model characterizes the complex interactions of the pulmonary interstitial and vascular system with a simple, algebraic solution.

Characterizing active lymphatic pumping in the pulmonary system. Pulmonary lymphatic structure is unique, with lymphatics draining fluid from the pleural, interstitial, thoracic, and diaphragmatic spaces (229). As mentioned above, our lumped model does not distinguish between locations. Pulmonary lymphatic flow was traditionally assumed to be a passive mechanism determined by the pressure difference (33) or extrinsic mechanisms (91), but more recent studies indicate that pulmonary

lymphatic vessels actively pump (52, 56). Intrinsic active lymphatic pumping varies with location (153), and although its role during edemagenic states and heart failure has not yet been assessed experimentally, it likely plays a role in ameliorating pulmonary edema (170). However, the effect of extrinsic pumping mechanisms on the lymphatics must be considered (186, 301). There is debate whether extrinsic pumping of lymph by respiration accounts for a significant portion lymph flow (153, 229), extrinsic pumping overrides intrinsic lymphatic pumping in the plural space where spontaneous contractions are rare (172). Nonetheless, studies have also indicated that inhibition of intrinsic lymphatic pumping reduces pleural lymph flow by up to 40% (170). In addition, lymphatic pressures more subatmospheric than pleural liquid pressures have been measured, with active lymphatic pumping suspected to be the primary method of achieving this (171). Although the parameter P_{pp} and R_{lp} in *Eq. 14* can be related to pumping in single lymphangions (210) and in lymphatic vessel networks (174), they are primarily empirical parameters that can include the effect of both intrinsic and extrinsic pumping.

Changes in pulmonary interstitial pressure are primarily influenced by interstitial fluid balance parameters. Although experimental research focusing on the mechanical determinants of pulmonary interstitial pressure is limited, pulmonary congestion is a critical predictor of survival (197). Investigators have focused on vascular variables for both diagnostics and treatment, especially for heart failure (197). For example, expanded blood volume has been suggested as a non-invasive diagnostic criteria for heart failure to replace pulmonary capillary wedge pressure (119). However,

our model indicates that interstitial parameters, known to vary with high pulmonary artery blood pressure (44, 107, 264), play a significant role in modifying pulmonary interstitial pressure, irrespective of total blood volume (Fig. 11). In normal subjects, P_{ip} is far more sensitive to changes in interstitial parameters (P_{pp}, K_{fp} and R_{lp}) than vascular parameters (Fig. 10). In subjects with heart failure, interstitial parameters continue to be the primary mediators of interstitial pressure (Fig. 11, *Eqs. 26* and *27*). Although the relative contribution of ventricular function (EE_{lv}) increases with incidence in HFpEF subjects (Fig. 11), interstitial parameters nonetheless have a far larger effect. Assessment of pulmonary edema is problematic (197), because pulmonary interstitial parameters (R_{lp}, K_{fp}, and $\Delta\Pi_p$) vary greatly during heart failure (107, 249, 264), yet they are not measured in clinical settings (150, 197). Experimental expansion of blood volume to induce pulmonary edema raises pulmonary interstitial pressure without a concomitant increase in pulmonary capillary pressures (158). Clearly it is difficult to obtain accurate information about pulmonary fluid balance from vascular hemodynamic measurements. In fact, conventional treatments that focus solely on improving vascular hemodynamics may paradoxically increase morbidity and mortality (150). The present work provides justification and impetus to focus clinical research on the management of interstitial fluid balance parameters.

Limitations imposed by assuming simplified, linear, algebraic models. Although the two separate models which comprise this model have been previously validated (49), they share several limitations. First, they only include parameters that characterize mechanical properties, and exclude all feedback other than regulation of systemic

arterial pressure. Such a focus on mechanical properties is appropriate, since all regulatory feedback mechanisms that ensure homeostasis in pressures, flows, and volumes, act through changes in these model parameters. Second, although many other mechanisms impact blood pressures and flow such as left and right ventricular interaction (242), respiration (144), valve resistances (242), and posture (100), these effects were neglected to maintain model simplicity. Similarly, many other complexities can mediate pulmonary interstitial pressure and volume, such as muscular pumping of lymphatic return (210), the location of collecting lymphatics (8), and shifts of fluid from intracellular compartments (289), but these were also neglected. Third, although our model is focused on interstitial pressures in chronic timescales, we do not include adaptation of parameter values characterizing microvascular filtration or lymphatic function. Our algebraic model can accommodate chronic changes in these properties by altering parameter values when more information becomes available, much like cardiac parameter values were altered to model heart failure phenotypes (Fig. 11). Taken together, these simplifications allow linear, algebraic solutions for our model. Additions to the model could be made to increase complexity, and perhaps its accuracy. Feedback mechanisms could be introduced, the pulmonary interstitial compartment can be split into three compartments, and nonlinear equations could replace the linear equations (*Eqs. C1-C15*). However, each of these additions come at the expense of increasing complexity and decreasing clarity (216), especially if they require numerical evaluation. The assumed simple, linear model equations enable derivation of algebraic formulas that provide unique capabilities absent in numerically-evaluated computational models.

Limitations of assuming an average pulmonary interstitial pressure. It is well-established that pulmonary capillary pressures decrease vertically with lung height (260). Conventionally, pulmonary capillary pressures are characterized for three distinct three zones (195, 284). Our model assumes a single lumped pulmonary interstitial compartment. Studies of pulmonary interstitial pressures are conflicting, with some indicating that interstitial pressures vary in each zone (159, 260), while others indicate a distribution independent of height (15, 22). Detailed measurements throughout the lungs have revealed that interstitial pressure can have a slight vertical and horizontal pressure gradient as the lung expands and distance from the venules increases (129). The pulmonary interstitial compartment could be split into three or more zones to account for spatial distribution of pulmonary interstitial pressures, which could accommodate spatial variation of microvascular filtration coefficients (160). However, by assuming that interstitial pressure decreases linearly from the top of the lung to the bottom (260), we calculated that the average pulmonary interstitial pressure from the three zones closely approximates the pulmonary interstitial pressure predicted when assuming a lumped compartment (results not shown). Although pulmonary edema in humans is known to occur more commonly in the basal areas with acute onset of heart failure (157), studies in animal models indicate that pulmonary edema forms first around the small vessels of the lungs (129). Once established, cardiogenic pulmonary edema manifests with diffuse distribution throughout the lungs (41), suggesting pressure zones play little role in pulmonary edema after its initial onset.

Limitations of characterizing systemic arterial pressure as a constant for chronic conditions. Mathematical models of physiological systems must determine which properties are constant, and which variables (38). Most conventional cardiovascular models assume that systemic arterial pressure is a variable, and that all mechanical properties, including blood volume, are constant parameters (13, 100, 267, 270). With pressure homeostasis, acute feedback acts primarily through the baroreflex, while over the course of hours to days, homeostasis is achieved primarily through changes in blood volume (142). To address systemic arterial pressure regulation, investigators have added additional equations to the minimal closed-loop model to represent the effect of the baroreflex (144) or renal function (9). However, this approach requires numerical solution and expansion of parameters, many of which must be assumed since they have not been experimentally measured (271). When averaged over the time scale of days, mean systemic arterial pressure remains relatively constant compared to blood and or extracellular volumes (142). Therefore, to capture the effect of pressure homeostasis, we treat systemic arterial pressure (P_{sa}) as a constant and volume (V) is treated as a variable. This assumption imposes its own limitations. Our solutions do not characterize the effect of acute perturbations. Furthermore, although compartments in our model are coupled, perturbations to vascular or cardiac parameters affect pulmonary interstitial pressure, but perturbations of interstitial parameters do not affect the blood pressures or cardiac output. This prevents the application of our model to acute conditions in which interstitial parameters impact how interstitial fluid volume can shift into the blood compartments during hemorrhage, shock, or exercise.

Limitations of characterizing effective lymphatic resistance with a single parameter. Perhaps one of the more important limitations of the present work is that we employed a lymphatic system model (49) that assumes pulmonary lymph flow as a function of hydrostatic pressure gradient between the pulmonary interstitium (P_{ip}) and the systemic venous pressure (P_{sv}). According to the Drake-Laine equation (130), lymph flow is equally sensitive to P_{ip} and P_{sv}, although studies by Gabel et al. (54) indicate that lymph flow in unanesthetized animals is much less sensitive to outlet pressure (i.e., P_{ip}) than inlet pressure. This differential sensitivity to inlet pressure was reproduced by Nguyen et al. (174), who reported that networks of pumping lymphangions can be described by a lumped model that is a modification of *Eq. 4*. Briefly, R_{lp} represents an "outlet resistance" (R_{out}) that mediates the effect of P_{sv} on lymph flow, and a new "inlet resistance" (R_{in}) was added that that mediates the effect of P_{ip} on lymph flow. Assuming that R_{in} is much greater than R_{out} reproduces the observed differential sensitivity of lymph flow to changes in P_{ip} and P_{sv}. This modified lumped model, when fully developed, could be incorporated in the present approach to characterizing the mechanical determinants of pulmonary interstitial pressure. It was not incorporated, since parameter values have not yet been established. Nonetheless, the effects of such a modification can be identified. Because pulmonary interstitial pressure is already particularly sensitive to R_{lp} (Fig. 10) and $R_{lp}K_{fp}$ (Fig. 11), it is likely R_{lp} and the nondimensional term $R_{in}K_{fp}$ would become a dominant determinants of pulmonary interstitial pressure. This modification may also change the degree of coupling between the pulmonary interstitial space and the cardiovascular system. However, the value of

R_{out} would best be characterized by R_{lp} used in the current model, since R_{lp} was measured specifically by changing lymphatic outlet pressure.

Limitations of assuming a constant oncotic pressure difference. The oncotic pressure difference ($\Delta\Pi_p$) decreases with hemodilution (69), interstitial fluid dilution (282), or changes in the microvascular reflection coefficient (282). An increase in microvascular fluid flow with elevated capillary pressure causes decreases in interstitial protein concentration (61). The increased oncotic pressure gradient would tend towards a decrease in interstitial pressure, if all other parameters were assumed constant. If this were the case, then P_{ip} would be overestimated in our model if it interstitial oncotic pressure were not appropriately adjusted. However, studies are conflicting on whether interstitial colloid osmotic pressure is decreased as much as hypothesized because of protein "wash-down" (253). Decreasing oncotic pressure acutely has a direct effect on the pulmonary volume in isolated lung preparations (69). Although according to the Starling-Landis equation, an increase in colloid osmotic pressure should predict an increase in extravascular lung water, clinically, the correlation is low (2). In addition, studies indicate that formation of pulmonary edema is influenced by increased interstitial pressure, but not by colloid osmotic pressure (62, 198). Hara et al. reported that even large changes in the plasma colloid osmotic pressure had no significant effect on interstitial volume and caused only a modest increase in lymph flow (96). Measurements of the oncotic pressure gradient are also conflicting with chronic heart failure. In patients with HFrEF, pulmonary colloid osmotic pressures were slightly higher than normal (176), while another study found slightly lower than normal colloid osmotic pressures in

HFpEF and HFrEF phenotypes (6). Fauchald et al. reported a slight increase in the colloid osmotic pressure gradient in patients in compensated heart failure (61). Thus, colloid osmotic pressure appears to be maintained at relatively constant levels on a chronic time scale. Therefore, we assumed the oncotic pressure gradient was constant. To deal with this limitation, we could describe the oncotic pressure gradient relationship with a piecewise linear function, adjusting the value with high microvascular filtration, similar to taking a piece-wise linear relationship to characterize the end-diastolic pressure-volume relationship (Fig. 8F). However, such a treatment would introduce more unknown parameters. In more extreme situations where the oncotic pressure gradient would be expected to exhibit large changes, such as with protein losing enteropathy (259), the new protein concentrations could be numerically calculated from the lymph flow as in Dongaonkar et al. (49). The main limitation of assuming a constant oncotic pressure gradient in chronic heart failure is that the relative sensitivity to parameters in Fig. 11 may need to be adjusted if $\Delta\Pi_p$ is found to differ significantly with chronic heart failure.

Model predicts pressures within measured ranges, and reproduces clinically-observed behaviors. Although blood pressures and cardiac output have been well-characterized for normal subjects and various types of heart failure, measurements of the pulmonary interstitial pressures in humans are rare. In fact, the conventional gold standard for assessing pulmonary edema, pulmonary capillary wedge pressure, is a poor approximation of interstitial pressure (279), and has been reported to be an inadequate indicator of pulmonary congestion (158, 279). However, although we lack the data to

characterize human parameters, parameters governing interstitial fluid balance have been characterized in animal models (49). Applying analytical, non-dimensional solutions allows us to validate model predictions using canine parameters (Table 3). Although not directly validated for humans, the use of nondimensional parameters (Fig. 11), many of which are recognized as allometric invariants across mammalian species, provides a degree of generality to the validation. Furthermore, nondimensionalization had an additional benefit of decreasing the degrees of freedom (i.e., there are five fewer nondimensional parameters than the individual model parameters). Parameters that are not reported for humans, such as K_{fp} and R_{lp}, become a single unknown dimensionless parameter (R_i) that may be relatively constant mammalian species. Despite the inability to validate specific predictions for human subjects, basic clinical observations can be matched to our predictions for two heart failure phenotypes. For example, our model predicts that Δo_{pn} (i.e., $\Delta \Pi_p / P_{sa}$) becomes more significant in HFrEF (*Eq. 26*). Clinically, decreased colloid osmotic pressure has been shown to be linked to survival in patients with acute heart failure (283). Our results are supported by the fact that systolic dysfunction is frequently present without increased congestion (215), while HFpEF is much more likely to develop pulmonary congestion. Second, our model predicts unstressed left ventricular volume (ΔV_{olv}) will play a large role in HFpEF. Clinically, we find that HFpEF patients are much more likely to exhibit an increase in ventricular volume (47), and HFpEF patients are more sensitive to circulating blood volume (47). The particular strength of algebraic formula is that they can predict trends when

parameters are perturbed, even when particular parameter values are poorly characterized.

Future research can be guided by model results. Although research on pulmonary edema is recognized as vital to decrease mortality rates (73), our model results highlight a fundamental problem: little research has focused specifically on the pulmonary lymphatic function, perhaps because its impact on pulmonary interstitial pressure has not been estimated. Most studies of heart failure focus on the vascular system (80), a perspective that is becoming recognized as inadequate (150), or focus on quantifying pulmonary interstitial volume (73, 300). The few studies which do focus on interstitial parameters measure capillary permeability to proteins (249, 266) or water (262, 264), but not the parameters characterizing lymphatic pressure-flow relationships. With the lack of knowledge of such critical parameters available to create and validate models, results of numerical models of the interstitium are particularly suspect. Nonetheless, our model suggests a focus for future research must include the quantification of R_{lp}, K_{fp}, and $\Delta\Pi_p$, which are primary determinants pulmonary interstitial pressure (Fig. 11). With normal renal function, pulmonary interstitial compliance (C_p), pulmonary volume (V_p), and unstressed volume (V_{op}) do not affect pulmonary interstitial pressure in equilibrium (*Eq. 13*). Although acute changes in P_{ip} are affected by V_{op} and C_p, they are irrelevant in timescales where blood and extracellular volumes vary to regulate systemic arterial pressure (49). Furthermore, P_{ip} is the fundamental variable responsible for alveolar flooding (158). Increased fluid volume is the primary factor used to characterize pulmonary congestion (73), yet edema is

primarily a symptom of elevated interstitial pressures. Compounding the lack of critical research is the fact that K_{fp} and R_{lp} appear to be synergistic (R_i, Fig. 11), but are studied in isolation (262, 266). Perhaps measurement of edemagenic gain (50), incorporating the combined parameter ($K_{fp}R_{lp}$), would provide a novel approach. In addition, although pulmonary congestion can lead to morbidity in subjects with HFpEF and HFrEF (65), significant differences and responses to treatment exist between the two phenotypes (25, 124, 230). Effective therapies are particularly lacking for patients with HFpEF (65, 105), and research is inhibited by a lack of animal models of HFpEF (65). Application of our model may suggest new approach to focusing research in heart failure. For example, lymphatic pump pressure (P_{pp}) has little impact on P_{ip} in HFpEF (*Eq. 15*), and increases in E_{maxlv} or decreases in E_{minlv} have little effect on P_{ip} when K_{fp} is elevated. Taken together, our model highlights gaps in current knowledge which may not have been recognized as worthy of study.

4. ARTERIOLAR ADAPTATION TO PULSATILITY

4.1 Background

Complex interactions govern microvascular structure and function. Because arterioles in the microvasculature are the site of most hemodynamic resistance, they play a vital role in ensuring that the blood supply matches tissue demand. Although local microvascular blood flow is largely uncoupled from the regulation of global hemodynamics (58), two main complexities arise in arteriolar networks. First, blood pressures and flows in a particular arteriole depend on the mechanical properties of adjacent vessels in the arteriolar network. When an arteriole radius changes, it alters the pressures and flows in its neighboring vessels as well as its own. Second, any change in blood pressure or flow affects vascular wall stress and endothelial shear stress, the two main mechanical stimuli governing chronic changes in vessel wall thickness and lumen radius (239). Endothelial shear stress, the frictional force imposed by blood flowing past the endothelium, in particular is well-established as an adaptive stimulus that determines chronic baseline arteriolar radii (204, 239). Whereas the field of biomechanics has focused on how vascular structure affects vascular mechanical stresses (29, 297), the field of mechanobiology has focused on how vascular mechanical stresses affect vascular structure (3, 143). The interaction of the biomechanics and mechanobiology ultimately determines the equilibrium radii in a vessel (173). Adaptation of microvascular structure is thus quite complex, even when restricting focus to growth and remodeling of an arteriolar network.

Although arterioles are believed to adapt solely to mean blood pressures and flows, significant pulsatility reaches the microvessels. Mean and pulsatile pressures and flows are governed by different mechanical properties. Whereas mean pressures and flows are mediated by vessel geometry and blood viscosity (i.e., vascular resistance), pulsatile pressures and flows are also mediated by vascular compliance and blood density (298). Given the high resistance of the microvasculature, investigators assumed only steady flow reached the microcirculation prior to development of advanced measurement techniques (115, 225). Pulsatile pressures in the microvasculature have since been measured, ranging from 4-15 mmHg (70, 111, 240, 303). Although relatively low compared to mean pressures, pulsatility originating from cardiac contractions can be transmitted completely through the microvasculature to reach the venous side (141, 233, 240). Interest in the pulsatile component of endothelial shear stress (typically characterized by the difference in maximum and minimum values) has gained attention as it became clear that endothelial cells respond differently when exposed to pulsatile flow (293). Acute decreases in pulsatile flow in vivo cause constriction and decreased perfusion by the microvasculature (115). It is well-established that chronic exposure to different levels of mean endothelial shear stress are linked to nitric oxide expression (32), and influence vessel adaptation (123, 217). Pulsatile shear stress has been implicated as an adaptive mechanism in the large arteries (173). However, experimental reports of arteriolar responses to pulsatility are limited.

Chronic exposure to decreased pulsatility in vivo leads to changes in microvascular structure and function. Studies comparing the effect of pulsatile and mean

flow on the microvasculature are conflicting. With a decrease in pulsatility, some studies report a decrease in microvascular perfusion or end-organ function (10, 46, 125, 182, 234, 235), while others found no difference (58, 212, 280). Prolonged decreases in pulsatility, however, can increase microvascular resistance (180) and alterations in microvascular structure (46), which has been attributed to decreases in pulsatile endothelial shear stress (166). Chronic decreases in pulsatile blood flow arise in multiple conditions: implantation of continuous-flow ventricular-assist devices (92, 243), Fontan circulations (101) and heart failure (294). Although decreased pulsatility may have minimal effects in large conductance arteries (58), a number of clinically-relevant microvascular malformations are associated with decreased pulsatility (42, 46, 101, 180). Several hypotheses have been advanced to explain the microvascular abnormalities such as changes in the circulating von Willebrand factor (43) or unmasking of subclinical arteriovenous malformations (11). However, microvessels are known to adapt to mechanical forces, and pulsatile shear stress is a major component of the mechanical forces acting on vessels (239). In addition, pulsatile flow can augment peak endothelial shear stress (168).

Models of chronic adaptation of the microcirculation are limited. Although several chronic studies exist of nonpulsatile circulations (46, 263, 302), they do not report changes in microvascular mechanical stresses. Because the mechanical stresses implicated in chronic adaption are difficult to measure in vivo in the microvasculature, studies have been limited to large conductance arteries (7, 190). In addition, experimental approaches are inadequate to characterize the independent processes that

alter mechanical forces (17). Biomechanical stresses are inherently linked with mechanobiological responses in vivo (239). Just isolating the response of one stress in vivo is difficult at best (275). Chronic culture of vessels, especially of microvessels, has had limited success (17, 299). Taken together, the multiple challenges of both in vivo and in vitro approaches have led investigators to resort to using mathematical models to study microvascular networks (93, 206). Investigators have developed mathematical models based on realistic microvascular structures to demonstrate network hemodynamics (193, 202). Despite notable exceptions (29, 67, 79, 193), most studied only steady flow (45, 78, 108, 112, 141, 177, 199), and most models of adapting microvascular networks assume vascular stress set points for vessel adaptation (93, 112, 117, 200), which may have limited physiological justification (173). Nonetheless, such modeling approaches have identified a central role for shear stress in determining the radii of arterioles in a network (205). Although adaptation of the large elastic arteries to pulsatile endothelial shear stress was modeled (173), pulsatile flows and pressures behave differently in the microcirculation. Blood inertia plays a negligible role (67), and resistance plays a relatively large role (67). The effect of structural adaptation to pulsatile endothelial shear stress in the microcirculation has yet to be modeled. Therefore, our purpose is to test the hypothesis that adaptation of arterioles to pulsatile endothelial shear stress can enhance structural stability of an arteriolar network, and decreasing pulsatility can increase peripheral resistance, cause rarefaction, and lead to arteriovenous shunts.

4.2 Methods

Mean endothelial shear stress in an arterial segment. When expressed in terms of the difference in inlet and outlet pressure, endothelial shear stress is a function of lumen radius (r) and vessel length (l). Although usually derived for the special case of steady blood flow, it applies for calculation of mean shear stress ($\bar{\tau}$),

$$\bar{\tau} = (\bar{P}_{in} - \bar{P}_{out})\frac{r}{2l}, \quad (28)$$

where $\bar{P}_{in}$ and $\bar{P}_{out}$ are the mean inlet and outlet pressures, respectively (298). For a constant pressure gradient imposed in vitro, endothelial shear stress increases linearly with vessel radius. Although $\bar{P}_{in}$ can be set experimentally in vivo, $\bar{P}_{out}$ is variable depending on the "load resistance" formed by the downstream vascular network (dotted box, Fig. 14A). The downstream load resistance (R_L) can be characterized by a single parameter (Fig. 14B). As detailed elsewhere (93, 211), if the vessel segment has a resistance (R) and is terminated with a network resistance R_L, $\bar{\tau}$ depends on the total pressure difference across the vascular network ($\Delta\bar{P}$),

$$\bar{\tau} = \Delta\bar{P}\frac{r}{2l}\left(1 - \frac{R_L}{R_L+R}\right). \quad (29)$$

When R is characterized by Poiseuille's Law, the ratio of a mean pressure gradient and mean flow ($\bar{Q}$) becomes,

$$R = \frac{\bar{P}_{in}-\bar{P}_{out}}{\bar{Q}} = \frac{8\mu l}{\pi r^4}, \quad (30)$$

which is a function of r, l, and blood viscosity (μ).

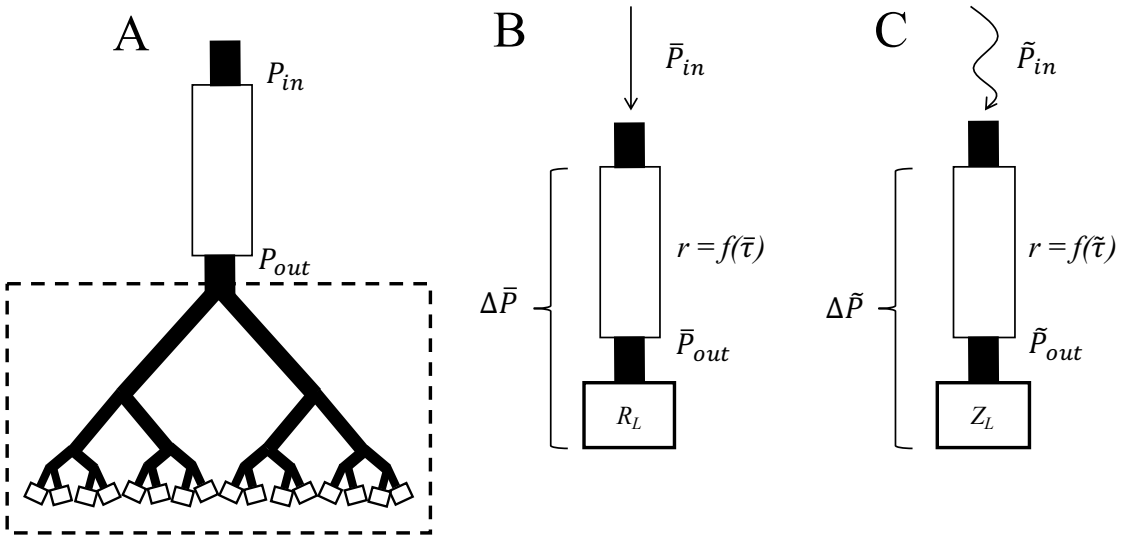

Figure 14. A single vessel adapting in a network can be represented with a network pressure gradient (ΔP) and a combined downstream load for both mean and pulsatile pressures and flows. A) Hemodynamics in a vessel can be calculated by assuming an inlet pressure (P_{in}) and calculating the output pressure (P_{out}) of a single vessel. The network vessels downstream of the vessel (dashed box) can be combined into a single terminating load (R_L). B) For mean pressures ($\bar{P}_{in}$, $\bar{P}_{out}$, $\Delta\bar{P}$), the downstream vessels can be represented by a terminating resistance (R_L). The vessel radius is assumed to adapt in response to changes in mean shear ($\bar{\tau}$). C) For pulsatile pressures ($\tilde{P}_{in}$, $\tilde{P}_{out}$, $\Delta\tilde{P}$), the downstream vessels are represented by a dynamic load (Z_L) that depends on the frequency of the pulsatile pressure. The vessel radius is assumed to adapt in response to changes in pulsatile shear ($\tilde{\tau}$).

The value of $\bar{\tau}$ then can be approximated from *Eq. 29* when R is relatively small or large:

$$\bar{\tau} \approx \begin{cases} \bar{Q}\frac{4\mu}{\pi r^3}, R \ll R_L \\ \Delta\bar{P}\frac{r}{2l}, R \gg R_L \end{cases}. \qquad (31)$$

When the radius of the vessel is large (and thus R is small), $\bar{Q}$ is relatively constant, and $\bar{\tau}$ decreases with radius. However, when the radius of the vessel is small (and thus R is large), then $\Delta\bar{P}$ becomes relatively constant, and $\bar{\tau}$ increases with radius. As described

elsewhere (211), mean endothelial shear stress exhibits a maximum $\bar{\tau}_{max}$ at a radius $\bar{r}_{max}$,

$$\bar{r}_{max} = \left(\frac{8\mu L}{3\pi R_L}\right)^{1/4} \quad \bar{\tau}_{max} = \Delta\bar{P}\left(\frac{27\mu}{512\pi l^3 R_L}\right)^{1/4} \quad . \tag{32}$$

Normalized mean shear stress ($\bar{\tau}'$), i.e. with $\bar{r}' = r/\bar{r}_{max}$ and $\bar{\tau}' = \bar{\tau}/\bar{\tau}_{max}$, can then be expressed in a very general form,

$$\bar{\tau}' = \frac{4r'}{3+r'^4} \, . \tag{33}$$

This normalized form of endothelial shear stress is particularly useful to characterize arterioles with disparate sizes within an arteriolar network, and provides a means to identify similarities in responses to changes in radii.

Approximation of endothelial shear stress in a vessel segment. In contrast to characterizing mean shear stress, characterizing the pulsatile shear stress ($\tilde{\tau}$) in a vessel is significantly more challenging (Fig. 14C). First, $\tilde{\tau}$ is a function of time, since both inlet pressure ($\tilde{P}_{in}$) and outlet pressure ($\tilde{P}_{out}$) are pulsatile. Following convention for characterizing pulsatile hemodynamics (298), pulsatile pressure and pulsatile shear stress are defined with mean values (i.e., $\bar{P}_{in}$, $\bar{P}_{out}$, $\bar{\tau}$) subtracted. The second complication arising from characterizing $\tilde{\tau}$ is that pulsatile pressures and flows are also impacted by vascular compliance (*C*), the change in volume for a given change in transmural pressure, as well as blood inertia (298). The relative contribution of blood inertia in the microvasculature, however, is small relative to the effect of resistance due to blood viscosity (67, 79). As detailed in *Appendix E*, in the special case that the effect of blood inertia is negligible, $\tilde{\tau}$ in the microvasculature degenerates into a simpler form,

$$\tilde{\tau} = \left(\tilde{P}_{in} - \tilde{P}_{out}\right)\frac{r}{2l}\,. \tag{34}$$

The third complication arising from characterizing $\tilde{\tau}$ is that $\tilde{P}_{in}$ and $\tilde{P}_{out}$ may not rise and fall simultaneously. As the heart ejects blood volume into the arterial system, it creates pulses that travel toward the peripheral vessels. There is a time delay as the pressure pulse travels from the inlet of a vessel to its outlet. Furthermore, a portion of the forward-traveling pressure pulse can be reflected back towards the heart at a branch point (298), further impacting the temporal difference between $\tilde{P}_{in}$ and $\tilde{P}_{out}$. Although pulsatile pressures and flow can be predicted with a high degree of accuracy using the full Navier-Stokes equations characterizing conservation of momentum, the standard transmission line equations (i.e., one-dimensional characterizations) are nonetheless effective approximations, and have been used to characterize hemodynamics in multiple microcirculatory networks (67, 72, 79, 193). *Appendix E* details the use of these equations to calculate of the pressure difference ($\tilde{P}_{in} - \tilde{P}_{out}$) across a vessel segment embedded in a vascular network (Fig. 14C) that incorporates the effects of pulse wave propagation and reflection. Substituting *Eq. E14* into *Eq. 34*,

$$\tilde{\tau} = \Delta\tilde{P} \cdot \frac{r}{2l}\left(1 - \frac{Z_L}{Z_L \cosh\frac{R}{Z_o} + Z_o \sinh\frac{R}{Z_o}}\right). \tag{35}$$

Unlike $\bar{\tau}$ (*Eq. 29*), $\tilde{\tau}$ depends on the *pulsatile* pressure gradient across the whole network ($\Delta\tilde{P}$), as well as two quantities that are standard for pulsatile hemodynamics—the load impedance (Z_L) and the characteristic impedance (Z_o). Unlike R_L, Z_L is the ratio of pulsatile pressure to pulsatile flow into a vascular network. The characteristic impedance, Z_o, is the ratio of pulsatile pressure to pulsatile flow in a vessel segment in

the absence of pulse wave reflection. As detailed in *Appendix E*, when the effects of blood inertia are negligible, Z_o (*Eq. E8*) becomes a function of R, C, and the frequency (ω) of the oscillatory pressures and flows,

$$Z_o = \frac{R}{\sqrt{i\omega CR}}. \quad (36)$$

Notably, the value Z_o depends on C, R and ω in microvessels (79), and is also a complex function of frequency, which contains the imaginary number i (i.e., $i = \sqrt{-1}$). This is very different from Z_o for large conductance vessels, which depend primarily on effects of blood inertia and vessel compliance (298).

Characterizing the load impedance in a microvascular network. Whereas the load impedance formed by a network of arteries can be characterized by a two- or three-element Windkessel (286), the microvasculature requires a different characterization (68). As detailed in *Appendix F*, the load impedance of a microvascular network, Z_L, can be adequately approximated by $1/\sqrt{i}$ multiplied by the magnitude of the load impedance, $|Z_L|$. Furthermore, $|Z_L|$ can be approximated by some constant k multiplied by the characteristic impedance of the subsequent downstream vessel (Z_{oL}). As a result, the load impedance formed by a microvascular network can have a relatively simple form,

$$Z_L \approx \frac{1}{\sqrt{i}}|Z_L| \approx \frac{k}{\sqrt{i}}|Z_{oL}|\,. \quad (37)$$

To illustrate the ability of *Eq. 37* to approximate the dynamic load formed by the microvascular network, it was plotted concurrently with the calculated load impedance of a distributed microvascular network (*Appendix E*).

Approximation of the magnitude of pulsatile shear stress in a vessel segment. The pulsatile shear stress characterized by *Eq. 35* is a complex function of time. Therefore, it was quantified by its magnitude ($|\tilde{\tau}|$), defined as the maximum minus the minimum value. The value of $|\tilde{\tau}|$ was calculated from *Eqs. 35-37* following standard approaches for taking the magnitude of a complex function. To simplify a rather complex result (not shown), a first-degree Taylor series polynomial was calculated for the case that the characteristic impedance (Z_o, *Eq. 36*) was high. Then the maximum shear stress $|\tilde{\tau}_{max}|$ at a particular radius $\tilde{r}_{max}$ was calculated in terms of vascular properties. To compare to mean shear stress (*Eq. 29*), pulsatile endothelial shear stress was normalized so that $|\tilde{\tau}'| = |\tilde{\tau}|/\tau_{max}$ and $\tilde{r}' = r/\tilde{r}_{max}$. To illustrate graphically, a vessel segment (vessel #23) was assumed from Salotto et al. (226) with a load and input impedance calculated for bifurcating microvascular network described below. Angular frequency (ω) was assumed to be equal to heart rate (1/sec) and dynamic viscosity equal to 0.03 g/cm-s. The magnitude of input pressure for both the pulsatile and mean solutions was assumed to be 12.5 mmHg. Both $|\tilde{\tau}|$ and $\bar{\tau}$ were plotted as a function of radius. To illustrate effects of imposed pressures and loads formed by the downstream network, $|\tilde{\tau}|$ was plotted with 30% increases in $|\Delta\tilde{P}|$ and $|Z_L|$, and $\bar{\tau}$ was plotted with 30% increases in $\Delta\bar{P}$ and R_L. Normalized shear stress ($|\tilde{\tau}'|$) was also plotted as a function of normalized radius ($\tilde{r}'$) for comparison purposes. The percent error was calculated for both the approximated magnitude of shear stress $|\tilde{\tau}|$ and normalized shear stress $|\tilde{\tau}'|$ compared to the magnitude of shear stress characterized by the full solution (*Eq. 35*) with a load calculated from the bifurcating network.

Adaptation to pulsatile endothelial shear stress. To characterize adaptation of vessel radius, it was assumed that the stimulus was sensitive to the magnitude of pulsatile shear stress ($|\tilde{\tau}|$),

$$r = r_o + \alpha|\tilde{\tau}|, \tag{38}$$

with radius being determined by the zero-intercept radius (r_o) and the sensitivity (α). As the magnitude of pulsatile shear increases, the radius increases. This assumption was similar to Nguyen et al. (173), who modeled adaptation of large conductance arteries to changes pulsatile endothelial shear stress. To better characterize adaptation in vessels in different parts of a network, this adaptive rule was expressed in terms of normalized radius (i.e., r/r_{max}),

$$r' = r_o' + \alpha'|\tilde{\tau}'|. \tag{39}$$

To maintain consistency, r_o and α were similarly normalized,

$$r_o' = \frac{r_o}{\tilde{r}_{max}} \qquad \alpha' = \frac{\alpha}{\tilde{\tau}_{max}/\tilde{r}_{max}}. \tag{40}$$

Whereas the shear-radius relationship in *Eq. 35* is a characterization of biomechanics (i.e., the effect of structure on mechanical forces), the shear-radius in *Eq. 38* is a characterization of mechanobiology (i.e., the effect of mechanical forces on structure).

Graphically characterizing the interaction of biomechanics and mechanobiology. To illustrate how the adaptation process characterized by *Eq. 39* interacts with the hemodynamics governing pulsatile endothelial shear stress in a vessel, a graphical balance point was constructed. First, an approximated value of $|\tilde{\tau}'|$ arising from hemodynamics (i.e., biomechanics) was plotted as a function of r'. Second, the adaptive response characterized by *Eq. 39* (i.e., mechanobiology) was plotted with r' on the

abscissa and $|\tilde{\tau}'|$ on the ordinate. For illustrative purposes, α' and r_o' were assigned values of 15 and -6.2, respectively. The intersection of the two plots represents equilibrium. To illustrate whether vessels grow or regress following a perturbation (e.g., by a change in inlet pressure), arrows were added in accordance with the following stability analysis.

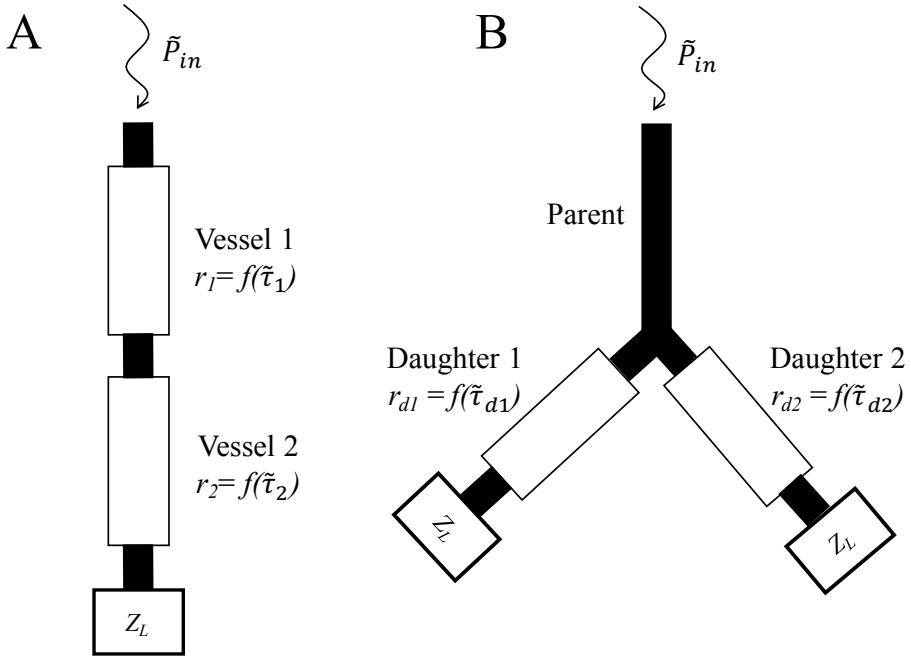

Figure 15. Vessels in series and parallel with radii adapting to pulsatile shear stress with dynamic loads (Z_L) that simulate the pulsatile pressure-flow relationships into a downstream arterial network. A) Simultaneous adaptation of the radius of vessel 1 (r_1) to pulsatile shear stress $\tilde{\tau}_1$, and the radius of vessel 2 (r_2) adapts to pulsatile shear stress $\tilde{\tau}_2$. B) Similarly, the radii (r_{d1}, r_{d2}) of two vessels in parallel (Daughter 1, Daughter 2) simultaneously adapt to shear in each vessel ($\tilde{\tau}_{d1}$, $\tilde{\tau}_{d2}$).

Endothelial shear stress in parallel and series vessels. Bifurcating networks can be assumed to be composed of multiple combinations of two vessels in series and two vessels in parallel. Therefore, two simple configurations of vessels were used to examine network behavior: 1) two vessels in series (Fig. 15A) with a terminal load (Z_{L1}), and 2) a vessel bifurcating into two vessels in parallel (Fig. 15B), each with a terminal load (Z_{L1} and Z_{L2}). The same approximations for $|\tilde{\tau}'|$ applied to the single vessel in Fig. 14C were applied to both vessel configurations.

Stability analysis. To determine stability of equilibria, both mean and pulsatile endothelial shear stress were calculated for each vessel configuration illustrated in Figs. 14 and 15: a single vessel, two vessels in series and two vessels in parallel. When a particular vessel is not in equilibrium, there is a difference in the instantaneous shear-radius relationship and the chronic shear-radius relationship. The difference between the current radius (r') and the expected radius it would have after adaptation ($r_o' + \alpha'|\tilde{\tau}'|$) can be quantified as,

$$\Delta r' = r_o' + \alpha'|\tilde{\tau}'| - r'. \quad (41)$$

Stability of each of the vessel configurations was examined in three ways. First, stability was determined mathematically using standard linear stability analysis. Assuming that $\Delta r'$ is equal to zero at equilibrium, and vessel parameters are positive and real, the Jacobian matrix (188) can be found for each system of equations for each vessel configuration (Figs. 14 and 15) by applying the partial derivative of $\Delta r'(r')$ for each radius,

$$\frac{\partial \Delta r'}{\partial r'}. \quad (42)$$

Evaluating the matrix at the equilibrium points, linear stability is assumed if the real parts of the eigenvalues of the Jacobian matrix are less than zero (93). Second, vector plots of the change in radius were graphed for $|\tilde{\tau}'|$ in the two parallel vessels (Fig. 14C) by plotting *Eq. 41* for each radius. First, a vessel segment with properties equivalent to vessel #23 from Salotto et al. (226) was assumed. All parameters were held constant except downstream load, which influences the normalized values of α' and r_o'. Two separate plots were created, one representing parallel vessels with relatively large downstream loads, and one with relatively small downstream loads. Selected α' and r_o' values for the large downstream load were 15 and -4.7, respectively, and for the small downstream load were 15 and -0.3, each chosen to permit illustrative graphs showing stability behavior. Third, the range of values of $\Delta\tilde{P}$ and Z_L that yield stable radii for both vessels in parallel (Fig. 15B) were approximated and plotted. To characterize how stability is different in two different-sized vessels, lengths and compliances of two vessels from Salotto et al. (226) were assumed (vessel #23 and #27), and each were assigned a load impedance calculated for the bifurcating microvascular network described below. Angular frequency (ω) was assumed to be equal to heart rate (1/sec) and dynamic viscosity equal to 0.03 g/cm-s. Inlet pressure magnitude was assumed to be 12.5 mmHg.

Pulsatile hemodynamics in a microvascular network model. To investigate the adaptive behavior in a spatially-distributed arteriolar network with realistic mechanical properties, a simple bifurcating tree with five levels was assumed. To simplify, no collateral vessels were included. Values used for simulation of the microvasculature are

reported in Table 5. Structural parameters for each of the vessels (C_T, R_T, l) were calculated from measured arterioles (226). Because perfectly symmetrical networks can exhibit artificial stability (203), a 10% increase in C_T and R_T for each parallel vessel pair was introduced. Density (ρ) was assumed equal to 1.05 g/cm^3.

Vessel Level	Original Radii (μm), (226)	Vessel Resistance (mmHg*s/cm^3), (226)	Vessel Compliance (cm^3/mmHg), (226)	Z_L (mmHg*s/cm^3)
A	50	$5.5*10^{7}$	$1.04*10^{-11}$	-
B	29	$3.24*10^{8}$	$7.2*10^{-12}$	-
C	18	$1.45e*10^{9}$	$7.41*10^{-12}$	-
D	10	$7.64*10^{9}$	$7.34*10^{-12}$	-
E	5	$4.89*10^{10}$	$2.5*10^{-13}$	$(1+i)*10^{2}$

Table 5. Network parameters used in simulations. Parameters were calculated with data (vessels #23-27) from Salotto et. al. (226). Asymmetry in the bifurcating tree was introduced (a 10% increase in C_T and R_T for each parallel vessel pair) to allow instabilities to manifest. Terminal load Z_L was calculated to reproduce measured mean pressures and flows.

The magnitude of inlet pulsatile and mean flow was assumed to be $1.2*10^{-5}$ and $2.59*10^{-5}$ cm^3/s respectively, in accordance with mean (79) and pulsatile (70) flows reported for vessels with radius approximately 50 μm. Vessels were terminated with a load impedance to simulate downstream capillaries and veins (68). Values of the terminal loads were adjusted to most closely replicate measured values of mean shear, flow, and pressures as determined by vessel diameter throughout the vessel tree (79). As detailed in *Appendix E*, pressures and flows were modeled using the transmission line equations for a thick-walled, linearly elastic vessel assuming Newtonian blood behavior.

Radial velocities, rotational flow, body forces, and entrance phenomena are assumed to be negligible. Mean pressures and flows throughout the network were calculated according to Poiseuille's Law (298). Dynamic viscosity (μ), which varies in arterioles due to the Fahreus-Lindqvist effect, was assumed to vary with radius according to the empirical descriptions of Pries et al. (201). The flow wave into the microcirculation was simulated based on data from a measured inlet flow wave in a mesenteric artery (252) and scaled until the mean flow and the inlet pulsatile pressure magnitude matched the measured values of $2.59*10^{-5}$ cm^3/s and 12.5 mmHg, respectively.

Adaptation to pulsatile and mean endothelial shear stress in microvascular network model. For the distributed arteriolar network, adaptation was assumed to be sensitive to both pulsatile (α) and mean shear stress (β) according to the equation below,

$$r = r_o + \alpha|\tilde{\tau}| + \beta\bar{\tau}. \quad (43)$$

Equation 43 allows adaptive responses to respond to differential changes in mean and pulsatile inlet flows.

Iteratively calculating equilibrium endothelial shears and radii in a microvascular network model. To predict hemodynamic variables, stresses, and radii in an adapting arteriolar network, *Eqs. E1-E5* were solved iteratively for $\tilde{Q}$ and $\tilde{P}$, $|\tilde{\tau}|$, and *r*. First, values of $\tilde{P}$ and $\tilde{Q}$ for initial *r* values were calculated with *Eqs. E1-E5*. Pulsatile shear was then calculated according to *Eq. 34* from radii and pressures. Then new values for radii in each vessel were then calculated according to *Eq. 43*. These steps were then repeated iteratively until radii reached a steady state, as determined by a change in of less than 0.001% from the previous iteration. Initial values for *r* were assigned to 1 mm

to limit initial parameters influence on the simulation. Adaptive parameters (α, r_o) as well as blood (ρ, μ) and vascular (l, C) parameters had constant values throughout the simulation.

Determining values for adaptive parameters. Because viable culture of vessels (especially microvessels) are difficult to sustain long enough to characterize responses to mechanical stimuli (17, 299), initial parameters characterizing adaptation of radii to endothelial shear stress (r_o, α) were first estimated from the pulsatile-shear radius relationship of the modeled network. Then parameters r_o and α were refined using a gradient descent method (66). After best-fit values were obtained, the process was then repeated with r_o and α held constant to identify an optimal β. The resulting values for α, β, and r_o were 0.105 cm^2/s^2kg, 0.004 cm^2/s^2kg, and $6.36*10^{-7}$ cm, respectively.

Effect of decreasing pulsatility on microvascular radii and peripheral resistance. To predict the effects of decreasing the pulsatile component of flow in an arteriolar network, the inlet flow (Q_{in}) was separated into two components. To maintain mean flow ($\bar{Q}$), the pulsatile flow ($\tilde{Q}$) was multiplied by a constant (δ) according to the equation below,

$$Q_{in} = \bar{Q} + \delta\tilde{Q}. \quad (44)$$

Decreases in pulsatility were simulated by decreasing (δ) from 1 to 0. Total network resistance (i.e., total peripheral resistance) was calculated according to standard methods (178) as inlet pulsatility decreased.

4.3 Results

First-order approximation of pulsatile endothelial shear in a single vessel. Approximating the magnitude of pulsatile endothelial shear stress, $|\tilde{\tau}|$, in a single vessel terminated by a load impedance (Fig. 14C),

$$|\tilde{\tau}| \approx \left|\Delta\tilde{P}\right| \frac{r}{2l} \cdot \frac{R}{\sqrt{(R+|Z_L|)^2+(\sqrt{2}-2)R\cdot|Z_L|}}, \tag{45}$$

reveals it to be function of *r*, *l*, and *R*, much like *Eq. 29*. However, unlike the formula for the mean shear stress (*Eq. 29*), $|\tilde{\tau}|$ is a function of the magnitude of the pulsatile pressure gradient, $\left|\Delta\tilde{P}\right|$, and the magnitude of the downstream load, $|Z_L|$. Approximated shear (*Eq. 45*) was found to have less than 2% error from the full solution (*Eq. 35*) when radii were less than 200 μm and vessel resistance was three orders of magnitude less than downstream load.

Comparison of pulsatile shear stress and mean shear stress in a single vessel. Figures 16A and 16B illustrate the comparison of mean and pulsatile shear stress in a single vessel as a function of radius. Both increase with the downstream load, and increase with the imposed pressure gradient. Both exhibit a peak shear at a particular radius. The peak magnitude of the pulsatile shear stress, $|\tilde{\tau}_{max}|$, at a particular radius ($\tilde{r}_{max}$), however, depends on $|Z_L|$ and $\Delta\tilde{P}$.

$$\tilde{r}_{max} \approx \left(\frac{4\sqrt{2}(\sqrt{7}-1)\mu l}{3\pi|Z_L|}\right)^{1/4} \quad |\tilde{\tau}_{max}| \approx \left|\Delta\tilde{P}\right| \left(\frac{27\mu}{8\sqrt{2}(17+7\sqrt{7})\pi l^3|Z_L|}\right)^{1/4} \tag{46}$$

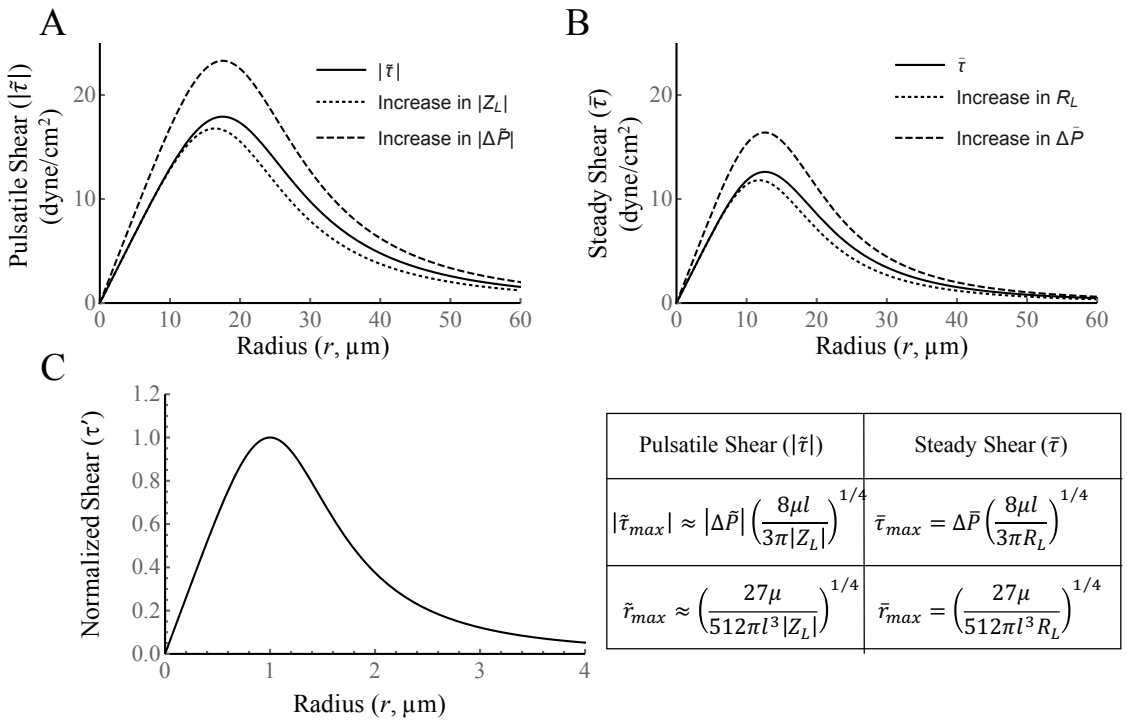

Pulsatile Shear ($\lvert\tilde{\tau}\rvert$)	Steady Shear ($\bar{\tau}$)
$\lvert\tilde{\tau}_{max}\rvert \approx \lvert\Delta\tilde{P}\rvert \left(\frac{8\mu l}{3\pi\lvert Z_L\rvert}\right)^{1/4}$	$\bar{\tau}_{max} = \Delta\bar{P}\left(\frac{8\mu l}{3\pi R_L}\right)^{1/4}$
$\tilde{r}_{max} \approx \left(\frac{27\mu}{512\pi l^3\lvert Z_L\rvert}\right)^{1/4}$	$\bar{r}_{max} = \left(\frac{27\mu}{512\pi l^3 R_L}\right)^{1/4}$

Figure 16. Effect of arteriolar network parameters on pulsatile (*Eq. 45*) and mean (*Eq. 33*) shear stress in a single vessel illustrated in Fig. 15 with parameters for vessel A in Table 3. A) Two network parameters determine the magnitude of pulsatile shear: the magnitude of pressure pulsatility ($\lvert\Delta\tilde{P}\rvert$) and the magnitude of the downstream load ($|Z_L|$). A 30% increase in $|Z_L|$ decreases pulsatile shear stress and shifts the peak to a lower radius. Increasing $\lvert\Delta\tilde{P}\rvert$ by 30% causes the curve to peak at a higher magnitude. B) Mean shear is lower in magnitude than pulsatile shear in the same vessel. However, increases in the two network parameters have the same effect, with a 30% increase in R_L decreasing shear, and a 30% increase in $\Delta\bar{P}$ increasing shear. C) Normalized pulsatile and mean endothelial shear stress approximated by *Eqs. 33* and *50* exhibit the same behavior. Formulas for maximum pulsatile and mean shear ($\lvert\tilde{\tau}_{max}\rvert, \bar{\tau}_{max}$) and radius ($\tilde{r}_{max}, \bar{r}_{max}$) are very similar, but depend on different parameters.

The differences between the pulsatile and mean shear stress become more apparent when comparing their maxima,

$$\frac{|\tilde{\tau}_{max}|}{\bar{\tau}_{max}} \approx 1.06 \frac{|\Delta\tilde{P}|}{\Delta\bar{P}} \left(\frac{R_L}{|Z_L|}\right)^{1/4} \qquad \frac{\tilde{r}_{max}}{\bar{r}_{max}} \approx 1.04 \left(\frac{R_L}{|Z_L|}\right)^{1/4}. \tag{47}$$

The ratios in *Eq. 47* imply that the term $\left(\sqrt{2}-2\right)R \cdot |Z_L|$ is relatively small, and pulsatile endothelial shear can be further simplified,

$$|\tilde{\tau}| \approx \left|\Delta\tilde{P}\right| \frac{r}{2l} \frac{R}{R+|Z_L|}, \tag{48}$$

which bears a close functional similarity to *Eq. 29*. *Equation 46* also simplifies further (illustrated in Fig. 16C). The simple approximation $|\tilde{\tau}|$ (*Eq. 48*) was found to have less than 8.75% percent error from the full solution (*Eq. 35*) at peak shear. The algebraic formula for $|\tilde{\tau}|$ approximated by the equation above becomes simpler in the extremes where the vessel resistance is either very low or very high,

$$|\tilde{\tau}| \approx \begin{cases} \frac{|\Delta\tilde{P}|}{|Z_L|} \cdot \frac{rR}{2l} \approx \left|\tilde{Q}\right| \frac{4\mu}{\pi r^3}, & R \ll |Z_L| \\ \left|\Delta\tilde{P}\right| \frac{r}{2l}, & R \gg |Z_L| \end{cases}. \tag{49}$$

Equation 49 thus recapitulates two common approximations for mean shear stress in the literature (211) when either an imposed blood flow or a pressure gradient is held constant (*Eq. 31*). Furthermore, the normalized magnitude of endothelial shear stress in *Eq. 48* simplifies to,

$$|\tilde{\tau}'| \approx \frac{\tau}{\tau_{max}} = \frac{4r'}{3+r'^4}. \tag{50}$$

Figure 16C therefore illustrates that $|\tilde{\tau}'|$ and $\bar{\tau}$ have the same functional form in terms of radius, although they are normalized by two different, independent factors ($\left|\Delta\tilde{P}\right|$ and Z_L versus $\Delta\bar{P}$ and R_L).

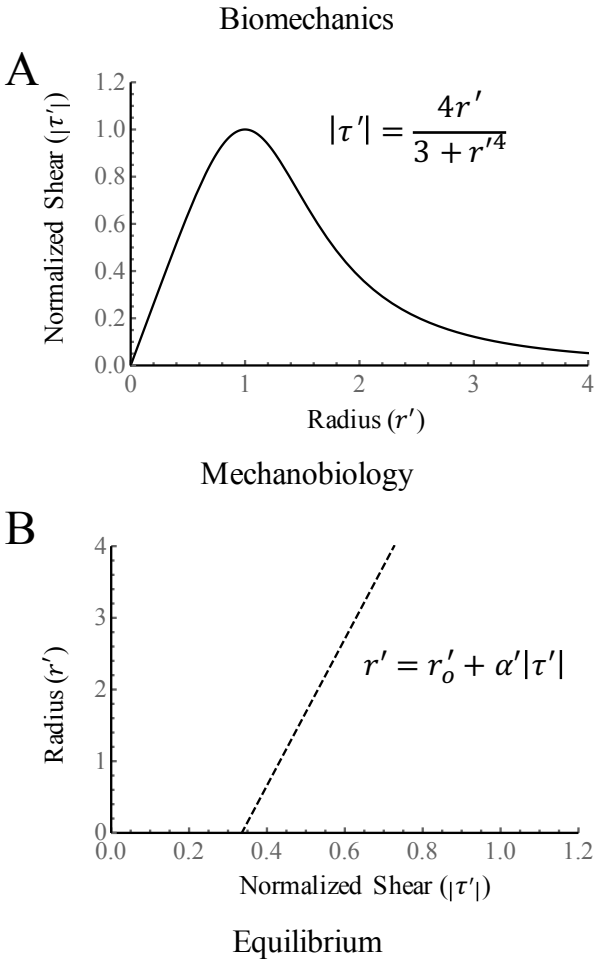

Figure 17. Balance point representation of the adaptation of radius to endothelial shear stress for a vessel terminated in a dynamic load (Fig. 1C). A) As radius increases, normalized endothelial shear stress first increases, and then decreases (*Eq. 50*). B) Adaptation of radius to pulsatile shear stress (*Eq. 39*) depends on parameters r'_o and α'. C) The balance of the two relationships determines equilibrium shear stress (τ'_{eq1}, τ'_{eq2}) and radii (r'_{eq1}, r'_{eq2}). Arrows indicate how radius will change when the vessel is not in equilibrium. The smaller equilibrium radius (open circle), is unstable; radii smaller than r'_{eq1} grow smaller and regress to zero. The larger equilibrium radius is stable; radii larger than r'_{eq1} will grow larger or smaller until equilibrium is established at r'_{eq2}.

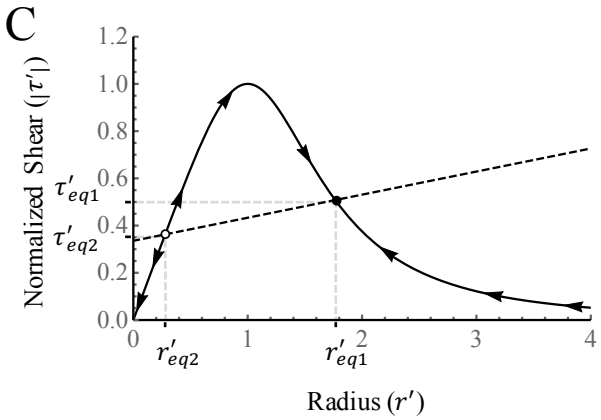

Figure 17. Continued.

Graphical illustration of balance point adaptation to pulsatile endothelial shear stress. Figure 17 characterizes the interaction of pulsatile endothelial shear stress (i.e., biomechanics) and the assumed adaptive response (i.e., mechanobiology) in a single microvessel. As radius increases, pulsatile endothelial shear stress (*Eq. 50*), exhibits a bimodal shape, first increasing and then decreasing (Fig. 17A). Following the adaptive rule characterized by *Eq. 39*, radius increases linearly with an increase in pulsatile endothelial shear stress (Fig. 17B). Equilibrium values of radii (r'_{eq1}, r'_{eq2}) and pulsatile endothelial shear stresses (τ'_{eq1}, τ'_{eq2}) result from the balance of these two opposing processes (circles, Fig. 17C). Note that although 'set points' are generally assumed for adaptation to endothelial shear stress in the microvasculature (93, 211, 236), our adaptive equation does not assume a set value of shear stress to which vessels must adapt. Instead, equilibrium values arise from the interaction of biomechanics and mechanobiology (i.e., Fig. 17C).

Stability of pulsatile endothelial shear adaptation in a single vessel in a network depends on initial radius. Two equilibrium points exist for a single vessel adapting to $|\tilde{\tau}'|$ (Fig. 17C). Stability is only possible if the change in radius with adaptation (*Eq. 41*) provides negative feedback that returns radii to equilibrium after a perturbation. Applying linear stability analysis, the real parts of the eigenvalue of the Jacobian will always be negative at r'_{eq2}, and positive at r'_{eq1}, indicating that r'_{eq2} is stable (solid circle, Fig. 17C) and r'_{eq1} is unstable (open circle, Fig. 17C). If a perturbation makes the vessel radius smaller than r'_{eq1}, the vessel will regress to zero radius. If a perturbation makes the vessel radius larger than r'_{eq1}, the vessel radius will grow to r'_{eq2}. Growth and regression are indicated by the arrows on Fig. 17C. Therefore, adaptation in a single vessel with a constant load Z_L will always be stable if initial radius is larger than r'_{eq1}.

Two vessels in series adapting to pulsatile endothelial shear maintain stability. Two vessels in series behave similarly to a single vessel, with two equilibrium points existing for the two vessels (not shown). Both vessels regress to zero if below the smaller of their equilibrium radii (i.e., r_{eq1}), and grow or decrease to the larger of their equilibrium radii (i.e., r_{eq2}) if above r_{eq1}. Applying linear stability analysis, r_{eq1} is found to always be unstable, and r_{eq2} is found to always be stable. Therefore, adaptation is stable for both vessels as long as initial radii are larger than r_{eq1}.

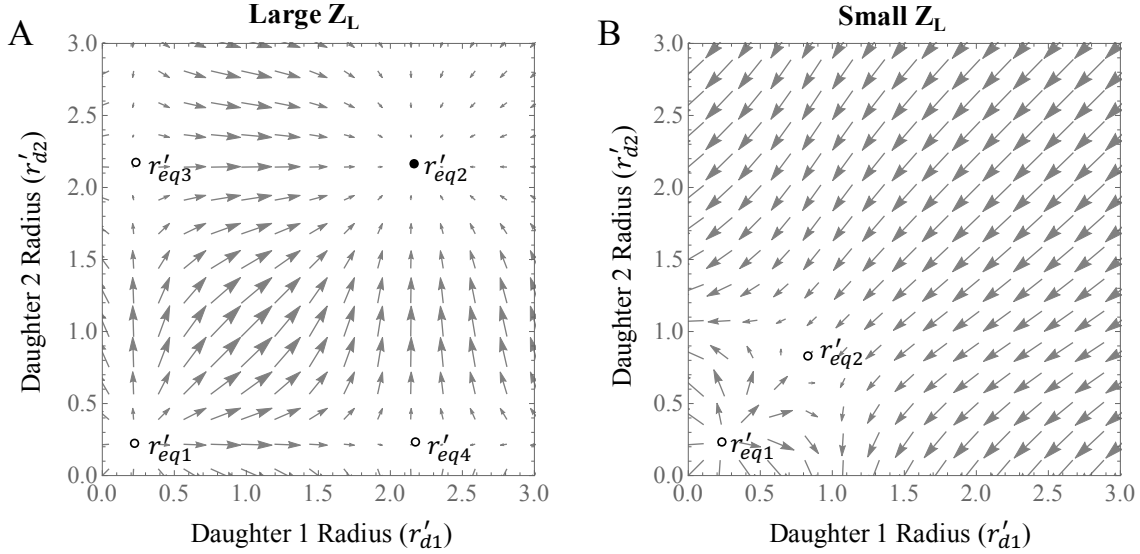

Figure 18. Simultaneous adaptation of radii to pulsatile endothelial shear stress in two parallel vessels (Fig. 2B) exhibits conditional stability. Arrows indicate how radii change when vessels are not in equilibrium. A) Adaptation of two parallel vessels to endothelial shear stress forms four equilibrium points when downstream dynamic loads are relatively large. One equilibrium point (r'_{eq2}, closed circle) is stable and three equilibria (r'_{eq1}, r'_{eq3}, and r'_{eq4}, open circles) are unstable. Therefore, when initial radii are below the unstable equilibrium point, vessels regress to zero, and when larger, they both adapt until they converge to r'_{eq2}. B) When downstream dynamic loads are relatively small, adaptation of two vessels in parallel becomes unstable. Only two equilibria are possible (r'_{eq1}, r'_{eq2}), but both are unstable, and radii regress to zero when perturbed.

Stability of adaptation of two vessels in parallel to pulsatile endothelial shear stress depends on the balance of downstream loads, inlet pressures, and adaptive parameters. Normalized shear in two parallel vessels has the same form for both mean and pulsatile shear, with shear in daughter vessel 1 (τ'_{d1}),

$$\tau'_{d1} = \frac{4r'_{d1}r'^4_1(3+r'^4_{d2})}{9r'^4_{d2}+r'^4_1(3+r'^4_{d1})(3+r'^4_{d2})+r'^4_{d3}(9+6r'^4_{d2})}, \quad (51)$$

dependent on both daughter vessels (r'_{d1}, r'_{d2}), and the upstream parent vessel (r'_1). Shear in daughter vessel 2 is of the same form. Solving for equilibrium radii results in four equilibria (Fig. 18). Linear stability analysis reveals that three of them (r'_{eq1}, r'_{eq2}, r'_{eq3}) are unstable. One equilibrium is conditionally stable (r'_{eq4}), depending on load impedances. With sufficiently high terminal loads (Fig. 18A), both radii will converge to (r'_{eq4}), as long as initial radii are greater than r'_{eq1}. As the terminal load decreases, two of those equilibrium points become equal to zero (r'_{eq2}, r'_{eq3}), and both remaining equilibrium points are found to be unstable with linear stability analysis (Fig. 18B). This is also indicated by divergence of the arrows away from the equilibrium points. The direction of the arrow indicates how each radius will incrementally change as it approaches equilibrium. The magnitude of the arrow indicates the degree of movement. Therefore, a region of stability exists where the balance of network parameters and vessel parameters creates a stable equilibrium (Fig. 19). When terminal load is too large, no equilibrium points exist, as the pulsatile shear and adaptive curves will not intersect, creating an upper bound for stable adaptation. When terminal load is too small, an increase in radius in one vessel will disproportionally decrease pulsatile shear in the parallel vessel, causing it to regress (Fig. 18B), creating a lower bound for stable adaptation. When loads are within the stable range indicated by the gray region of Fig. 19, an increase in radius of one vessel does not cause the parallel vessel to regress (Fig. 18A). Pulsatile pressure, however, increases stability of vessels in parallel. It is important to note that increases in pulsatile pressure ($\left|\Delta\tilde{P}\right|$) have identical effects as increasing the sensitivity to pulsatile shear stress (α). Also, as r_o becomes closer to zero,

the range of stability also increases (results not shown). However, the stable range also depends on the vessel parameters. For the larger arterioles (Fig. 19A), the range of terminal loads over which it is stable is much larger than for the small arterioles (Fig. 19B).

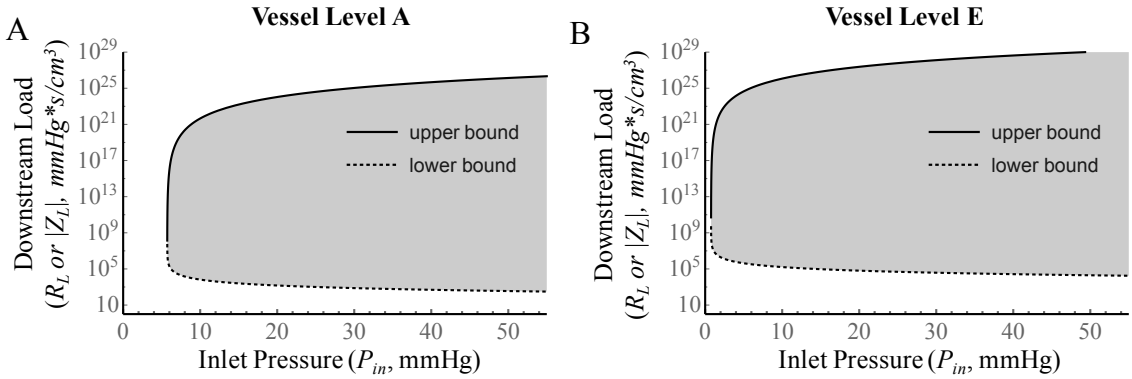

Figure 19. Parallel vessels adapting to mean or pulsatile shear stress are stable (shaded zone) when the balance of downstream dynamic loads, inlet pressures, and vessel parameters are within a specific ranges. The range of stability increases with inlet pressure. The range of stability also depends on size and compliance of vessels. For larger arterioles (A) characterized by parameters for vessel A (Table 1), the lower bound of stability (dotted line) of downstream loads is an order of magnitude larger than for smaller arterioles (B) characterized by parameters for vessel E (Table 1). Downstream vessels therefore can exhibit instabilities before upstream vessels.

Adaptation to pulsatile endothelial shear stress can result in a stable network and mean pressures, flows and shear stress similar to measured values. The distributed bifurcating network reproduces mean pressures and flows similar to measured mean pressure (140) and flows (111), averaged by vessel level (Fig. 20), following the process

outlined in Fig. 21. Assuming $\beta = 0$, adaptation to solely pulsatile endothelial shear stress results in a microvascular network with vessel architecture characterized by radii decreasing with bifurcation level and vessel radii similar to measured radii (226) (Fig. 20). Adapted vessel radii are shown scaled according to size, with the largest radius at level A equal to 25.2 μm and the smallest radius at level E equal to 9.6 μm. Adapted radii on average were found to have a 70.5% error from measured radii, with the model tending to overestimate upstream vessels and underestimate downstream vessels.

Adaptation to decreased endothelial pulsatile shear stress and mean shear stress leads to network architecture similar to low pulse circulations. With adaptation to both mean and pulsatile shear, as the pulsatile component (δ) of the inlet flow decreases, radii decrease, and thus overall resistance of the network increases (Fig. 23A). Radii adapted to both mean and pulsatile shear were found to have an average of 74.6% error from measured radii, with the model tending to overestimate upstream vessels and underestimate downstream vessels. Adaptation to steady endothelial shear stress is unstable (Fig. 23C), with vessels forming one large pathway through any given network of vessels. Once the pulsatile component reaches zero, radii form one main pathway through the network, with other vessels regressing to values close to zero (Fig. 23B). The network exhibits capillary rarefaction and an arteriovenous shunt (Fig. 23C), characteristic of arteriovenous malformations.

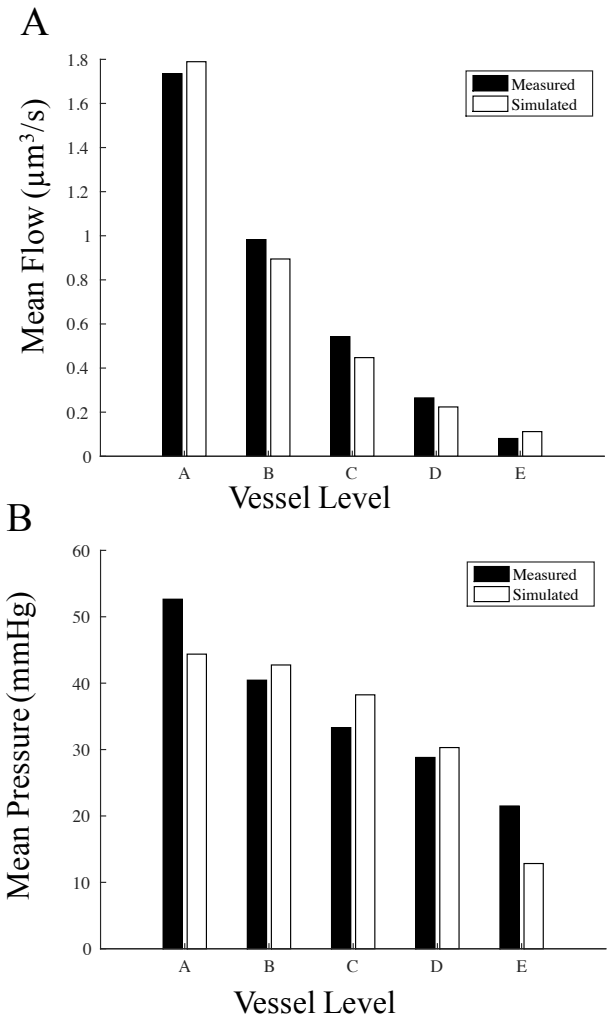

Figure 20. Arteriolar network predicts mean flows (A) and pressures (B) that are similar to measured flows and pressures (111). Predicted mean pressures and flows were averaged over each level of the bifurcating tree. Downstream vessels therefore can exhibit instabilities before upstream vessels.

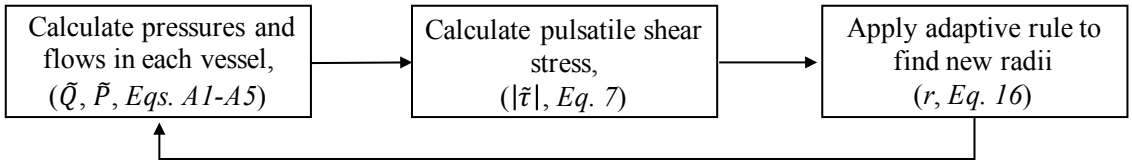

Figure 21. Schematic of iterative process used to adapt radii in response to changes in pulsatile endothelial shear stress. First, initial pressures and flows ($\tilde{Q}$ and $\tilde{P}$) are calculated from initial radii values for the network for each level. Second, pulsatile shear stress ($|\tilde{\tau}|$) is calculated from the pulsatile pressures and radii. Third, adapted radii are found by applying the adaptive equation. Adapted radii (r) are then used to calculate new pressures and flows throughout the network. This process is then repeated until difference in radii between iterations is less than 0.001%.

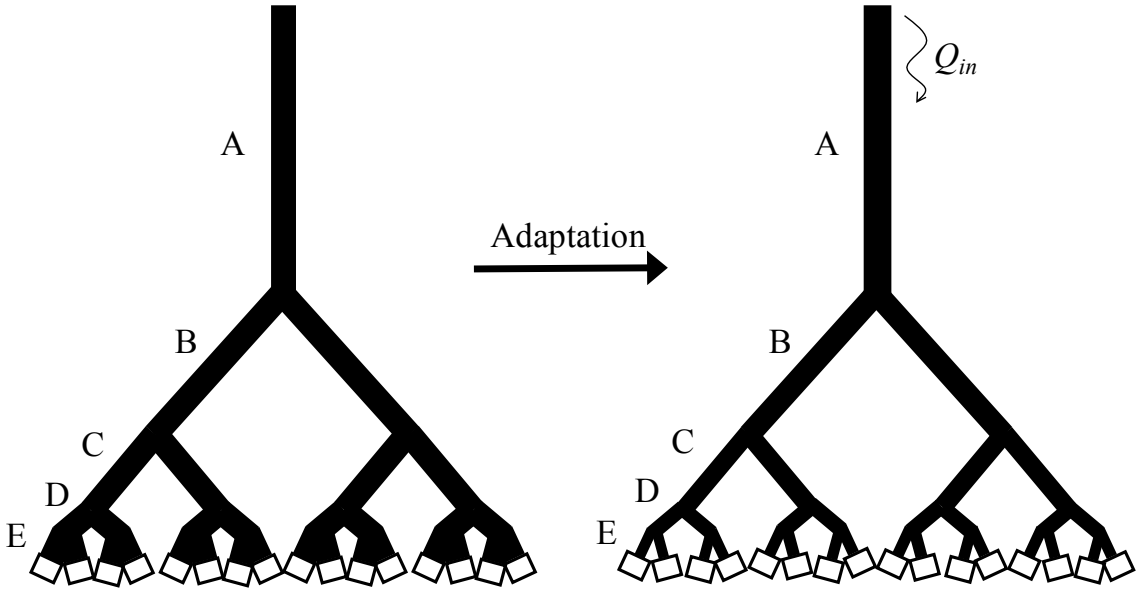

Figure 22. Representation of the simple, five-level bifurcating arteriolar network illustrating adaptation of radii to pulsatile endothelial shear stress. Vessels are labeled with bifurcation level (A-E), with each E-level vessel terminated in a complex load (box) representing a downstream load formed by capillaries and venules. Initial radii were assumed equal to 1 mm (left). Adaptation to pulsatile endothelial shear stress results in a stable network (i.e., no radii regressing to zero), reproducing normal network architecture (right) with vessels decreasing in size with each bifurcation level. Vessels drawn with radii scaled relative to the radii of the first vessel.

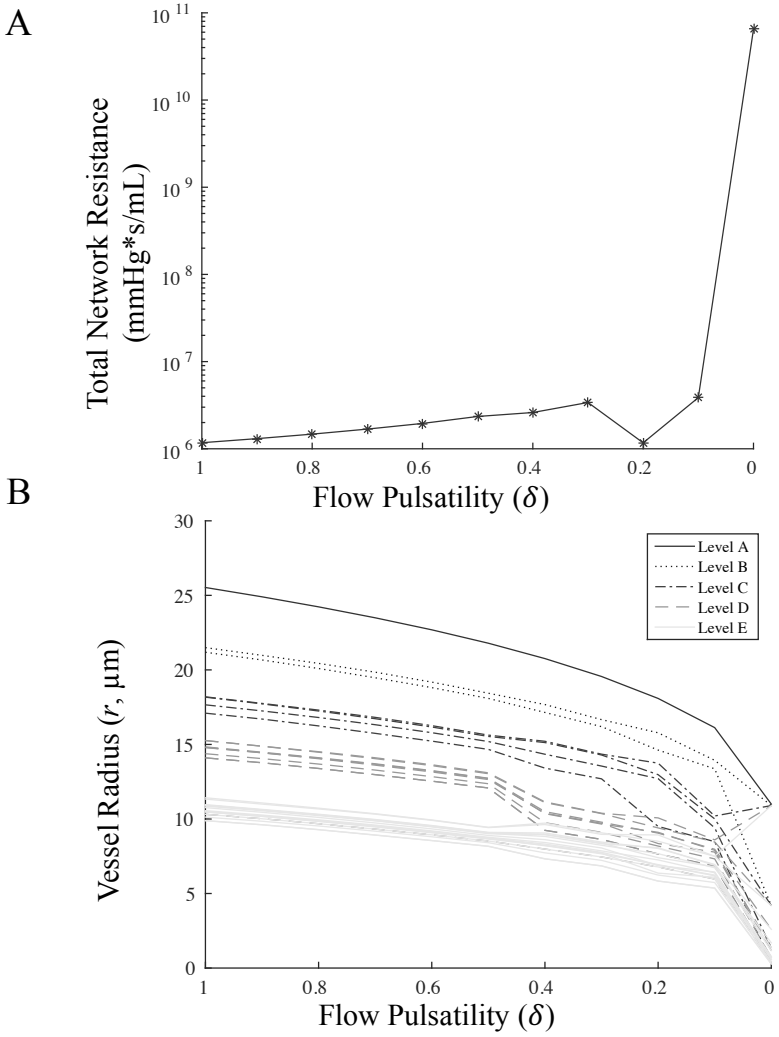

Figure 23. An arteriolar network adapting to both decreased pulsatile flow and steady flow exhibits network architecture similar to those seen in low pulsatility circulations. As pulsatile flow into the network decreases, A) total resistance of the network (R_{tot}) generally increases, with adaptation at solely steady flow ($\delta = 0$, *Eq. 44*) predicting a large increase in resistance as most vessels regress. B) Decreases in pulsatility cause vessels to remodel to smaller radii, with most radii at zero pulsatility remodeling to near zero radius. C) Decreases in pulsatility lead to the formation of network architecture with capillary rarefaction and an arteriovenous shunt, characteristic of arteriovenous malformations. At $\delta = 1$, or 100% of the inlet pulsatile flow, radii adapt to form a network with normal architecture. At 50% of inlet pulsatile flow ($\delta = 0.5$), radii decrease and begin to exhibit greater variation in parallel vessels. At $\delta = 0$ (steady flow) all radii except one pathway decrease to near zero. Radii less than 5 μm were represented with a dotted line.

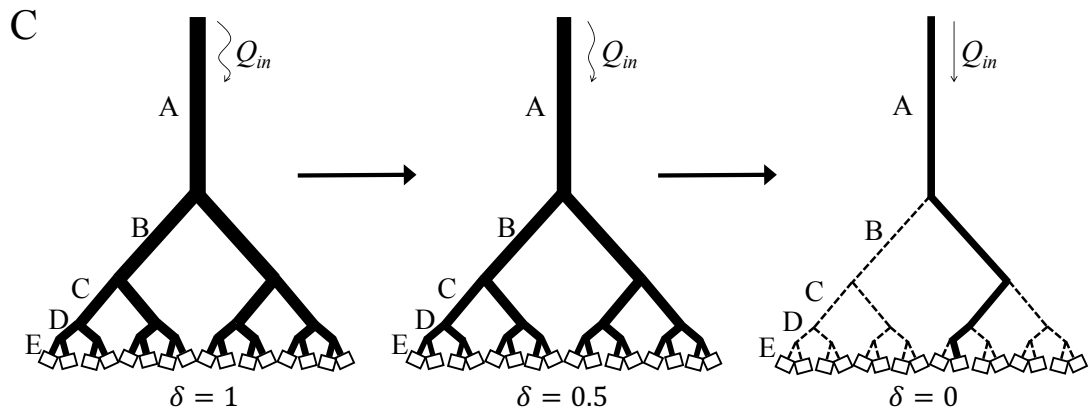

Figure 23. Continued.

4.4 Discussion

Adaptation to pulsatile endothelial shear stress can enhance stability in microvascular networks. Although the pulsatile and mean endothelial shear stress in an arteriole depend on different parameters characterizing the imposed pressure and downstream load, they exhibit surprisingly similar behavior (Fig. 16). At relatively small radii, endothelial shear increases linearly with radius (*Eqs. 31* and *49*). At relatively large radii, endothelial shear stress falls with the third power of radius (*Eqs. 31* and *49*). Because the pulsatile and mean endothelial shear stress can be approximated by similar non-dimensional equations (*Eqs. 33*, *41*, and *50*), stability of vessels adapting to mean shear stress behaves similarly to vessels adapting to pulsatile shear stress in Fig. 17. A single vessel with a non-adapting dynamic load exhibits two equilibria, with only the larger of the two equilibria stable (Fig. 17). Adaptive behavior is similar when two vessels in series adapt simultaneously. When two vessels in parallel adapt

simultaneously, however, they exhibit conditional stability. Both vessels may exhibit stable adaptation, where both remain patent (Fig. 18A), or they may exhibit unstable adaptation, with one or two vessels regressing to zero (Fig. 18B). The stability of two parallel adapting vessels is conditional, depending on the combination of downstream dynamic loads, inlet pressures, and adaptive parameter values (Fig. 19). These simple models reproduce and help clarify the complex behavior resulting from adaptation of all radii in a bifurcating arteriolar network to pulsatile shear stress (Fig. 21). With carefully-chosen parameter values characterizing adaptation to shear stress, adaptation to pulsatile endothelial shear reproduces normal network architecture (Fig. 22). When simulating an arteriolar network that includes adaptation to both mean and pulsatile endothelial shear stress, a decrease in pulsatility causes 1) an increase in peripheral resistance, 2) capillary rarefaction, and 3) a formation of an arteriovenous shunt (Fig. 23) characteristic of arteriovenous malformations. We assumed a simple arterial network structure (Fig. 22) and stimuli that affect growth and regression of radii (*Eq. 43*) to elucidate how adaptation to pulsatile shear stress differs from adaptation to mean shear stress. Very complex models have been proposed that illustrate that additional stimuli such as vascular wall stress, metabolic stimuli, and conducted stimuli (204) can be strong enough to ensure network stability when pulsatile endothelial shear stress is neglected. However, by deliberately assuming a simpler model, we were able to illustrate the particular role of pulsatile shear stress in enhancing stability of arterial network structure.

Limitations due to assuming a simple bifurcating network with imposed inlet flow and constant downstream loads. The present work limited study of structural adaptation to a simple bifurcating network of arterioles (Fig. 22) exposed to an imposed inlet flow. Previous modeling studies have included much more complexity to their structures, including venules (204, 211), collaterals (93, 211), and multiple vessels in parallel (108, 204). By applying multiple adaptive rules, Pries et al. (204) and Quick et al. (211) could reproduce arterio-venous asymmetry (i.e., venules larger than arteries) and particular responses to perturbations such as changes in arterial pressures. However, the present work deliberately limited structure to bifurcations without collaterals, with constant (non-adapting) loads, and imposed inlet flow. The purpose of this limited focus was fourfold. First, relating the complex behavior of an adapting network (Fig. 23) to that of a single vessel (Fig. 18) or vessels in parallel (Fig. 19) is simpler with an ordered arterial network. Second, we focused on peripheral resistance changes and manifestation of arteriovenous malformations, rather than the loss of collaterals. Third, pulse wave propagation and reflection in a non-bifurcating vascular network can exhibit a high level of complexity, making it difficult to relate adaptive behavior to particular hemodynamic properties. Fourth, the mechanical properties which govern propagation and reflection of pulse waves are rarely measured (226), especially in capillaries and venules (193), causing simulations of more complex networks to be particularly sensitive to assumed parameter values. As a result, our present work is limited in scope. This model cannot address adaptation and stability of collateral vessels (200), alteration of downstream loads with changes in local blood flow or oxygen levels (211), or adaptation of venules

(204). Similarly, the present work assumes an imposed inlet flow, rather than an imposed inlet pressure. Imposed inlet pressures are commonly assumed for pulsatile microvascular networks (68, 79) although autoregulation would have the effect of ensuring a constant inlet flow in a stable microvascular network. We chose to simulate adaptation to a constant inlet pulsatile flow (Figs. 22 and 23) for two reasons. First, it was simpler to interpret results when the magnitude of pulsatile blood flow was altered. Second, changes in pulsatile flow (as opposed to mean flow) would have no direct impact on clearing downstream metabolites. By choosing to limit the scope of the present work, we were able to generalize results (Figs. 16-19) and relate specific behavior of an arteriolar network (Fig. 23) to particular vascular properties.

Limitations due to assuming a system that adapts only to endothelial shear stress. The present work limits study to adaptation of radii in an arteriolar network to endothelial shear stress. However, many stimuli have been shown to have an effect on vessel adaptation in the microcirculation (155, 164, 239), and in vivo, multiple stimuli interact to maintain stability in microvascular networks. Acute experimental isolated vessel preparations have indicated that microvessel radii (and thus wall thicknesses) change in response to perturbations in mean endothelial shear stress (155), mean wall stress (164), and metabolites (239). Previously-reported mathematical models have focused on the chronic response of vessels to these stimuli, suggesting that multiple adaptive stimuli are necessary for microvascular network structure to maintain stability (113, 204). Price et al. reported networks adapting only to wall stress would exhibit rarefaction (199). Hacking et al. reported that networks adapting to mean endothelial

shear stress are not sufficient to ensure stability (93). Jacobsen et al. (112) and Godde et al. (77) reported that adaptation to both wall stress and shear stress were required for a stable network. Pries et al. (204) reported that three stimuli were required for microvascular network stability: mean flows (i.e., metabolite concentration), mean endothelial shear stress and a conducted stimulus. In addition, adaptation of radii to pressure was necessary to reproduce arterio-venous asymmetry. We chose to limit stimuli in our model to endothelial shear stress for three reasons. First, we wanted to specifically compare behaviors arising from adaptation to mean and pulsatile shear stresses. Second, differences in stability between adaptation to mean shear and pulsatile shear would be difficult to interpret with the addition of metabolic stimuli. Changes in mean flow alter both mean shear stress and metabolic stimuli, but changes in pulsatile flow have no direct effect on metabolic stimuli. Third, the effect of adaptation to mean shear stress, metabolic stimuli and mean pressures and flows has been previously clarified in multiple networks (93, 112, 204). While it is well-established that endothelial cells respond differentially to pulsatile shear (293), there is limited support for other pulsatile stimuli affecting chronic adaptation of vessel radii. However, because we focused on a simple bifurcating arteriolar network with constant downstream loads, we could not establish that adaptation to pulsatile shear stress is sufficient to yield stable structure of an entire microvascular network. Indeed, it is likely that metabolic stimuli are necessary to keep downstream loads formed by capillaries and venules from regressing (204). Model results illustrated in Fig. 19 indicate that as downstream loads decrease, the arterial network would become unstable. Therefore, adaptation to pulsatile

endothelial shear stress would not ensure stability in more complex networks. While adaptation to pulsatile endothelial shear stress may be only one contributor to stability in an arteriolar network, the present work suggests that its net effect is to enhance structural stability. Similar adaptation to mean or pulsatile wall stress (i.e., modifying *Eq. 38* so that radius increases or decreases with wall stress) does not enhance stability (results not shown).

Limitations of assuming linear adaptive processes. The present work assumed a linear radius-shear adaptive relationship (*Eqs. 38* and *43*). Biological processes often exhibit sigmoidal stimulus-response relationships, although over a small enough range, every process can be approximated with a linear relationship (37). It is probable that sensitivity to pulsatile endothelial shear exhibits nonlinear behavior. However, limited data exists of the response of microvessels to chronic endothelial shear stress, and to the best of our knowledge, no studies are reported that correlate changes in vessel radius to chronic changes in pulsatile shear stress in vivo. Therefore, to test the hypothesis that adaptation to pulsatile endothelial shear enhances network stability, we kept the adaptation equation as simple as possible. A nonlinear description would require additional parameters that must be assumed with little empirical justification. Unlike a sigmoidal response, the linear adaptive response characterized in Fig 17B allows vessels to adapt to become very large or regress until they disappear altogether. It is known that very high or very low endothelial shear stresses can cause endothelial dysfunction (60) which can lead to vascular smooth muscle proliferation and activation of clotting factors (60), which ultimately leads to thrombosis and subsequent regression. These extreme

ranges may not be relevant in the present work, since the adaptive process itself acts as a homeostatic mechanism that acts to minimize changes in shear stress.

The combination of downstream loads, inlet pressures, and adaptive parameters govern stability of vessels adapting to both mean and pulsatile shear adaptation. The present work provides the first model of adaptation of radii in an arteriolar network in response to pulsatile endothelial shear stress. Although the mechanical properties governing pulsatile shear stress are different from the mechanical properties governing mean shear stress, there is a surprising level of similarity (Fig. 16). Both pulsatile and mean shear stress are bimodal functions of radius. As radius increases, shear stress increases to a maximum value. Further increases in radius decrease shear stress. The functional form of the approximation for pulsatile shear stress (*Eq. 50*) is very similar to that of mean shear stress (*Eq. 33*). Both mean and pulsatile shear stresses can be approximated to be a function of constant pressure when radii are small (*Eqs. 31* and *49*), but functions of a constant flow when radii are large (*Eqs. 31* and *49*). This hemodynamic similarity results in similar behaviors when vessels adapt to pulsatile or mean endothelial shear stresses. When sensitivity to shear stress is too low regress (i.e., the adaptation and hemodynamics curves in Fig. 16C never intersect), remodeling to a smaller radius will never increase shear stress enough to halt regression. Similarly, endothelial shear stress can be too low to ensure stability when the imposed pressure gradient is too low or downstream resistance is too high. Furthermore, if the load to a single vessel is very low, increases in radius lead to an unbounded increase in shear stress, which in turn leads to adaptation that increases vessel radius (i.e., positive

feedback). Similarly, with two vessels in parallel, the combination of inlet pressures, vessel sensitivities, and downstream loads determine the range of stability. For instance, the range of parameter values that result in stability are smaller for downstream vessels (Level E, Fig. 22B) than the upstream vessels (Level A, Fig. 22A). Therefore, it is not surprising that the smallest vessels will became unstable first when adapting in a network (Fig. 23B). Instabilities in the smallest vessels have a cascading effect: when the radii of the smallest vessels regress, they increase the load to upstream vessels, thus decreasing their shear stresses and cause them to regress in turn.

Although adaptation to pulsatile and mean endothelial shear stress exhibit similar behavior, they differ in significant ways. Because the mechanics governing pulsatile hemodynamics differ from the mechanics governing mean pressures and flows, adaptation to pulsatile and shear stresses can be uncoupled in three ways. 1) Pulsatile pressure and mean pressure can have different values. In vivo, inlet pulse pressure can be much lower than mean pressure (e.g., 12 mmHg versus 54 mmHg) (141). In extreme conditions, such as with the implantation of a continuous-flow left-ventricular assist device (261), mean pressures and flows can be normal, while pulsatile pressures and flows can be negligible. 2) The dynamic load formed by a vascular network downstream of a vessel (i.e., load impedance, Z_L) can be very different than the static load (i.e., peripheral resistance, R_L). Pulsatile shear stress is not only impacted by the resistances of all downstream vessels, but also by their compliances (*Eq. 36*). While capillary and venous impedance are not well-characterized, models of microcirculatory networks have indicated that the choice of terminating loads can play a significant role in pulsatile

pressures and flows upstream (72). Pulsatile pressures and flows, and thus shear stresses, are impacted by pulse wave reflection and propagation (*Appendix E*). 3) While approximations of pulsatile shear stress (*Eq. 50*) are similar to mean shear stress (*Eq. 33*), they can deviate significantly in particular contexts. The approximation of pulsatile endothelial shear stress (*Eq. 50*) in a single vessel (Fig. 14) and vessels in parallel (Fig. 15B) incurs small errors, in part because the downstream load is chosen to mimic an arterial network, and pulse wave reflection is highly constrained. This approximation, however, can incur almost 50% error in pulsatile shears of vessels in the upstream vessel of two vessels in series (Fig. 15A). In this case, the pulse wave reflection at the junction of the two vessels can have a significant impact. Thus, in a situation where all three vessels in a bifurcation are adapting, adaptation to mean and pulsatile shear stresses may result in very different behavior.

Differential sensitivity to pulsatile and mean endothelial shear stress suggests a physiological relevance for different molecular mechanisms regulating adaptation to pulsatile endothelial shear stress. The present work takes a novel approach and utilizes a graphical balance point to characterize the process of structural adaption of microvessels. Such an approach was recently used to adaptation of large conductance arteries (173). Such a representation helps highlight how adaptation characterized as a stimulus-response (e.g., *Eq. 38*) is fundamentally from an assumed shear stress "set point". A set point can be a dubious assumption that may lack physiological relevance (34). A mechanical stress set point assumes a target equilibrium stress is achieved, without invoking the mechanobiology that transduces different levels of stress into a

particular radius. Although assuming equilibrium shear stress a priori in a model can inform how structure emerges, it cannot address how the equilibrium stresses emerge, nor can it address the effects of changes in mechanotransduction. Instead, we assume that endothelial shear stress governs chronic radii (*Eq. 35*), and that the equilibrium value of shear stress is a variable that emerges (from the interaction of biomechanics and mechanobiology (Fig. 17). Our approach is similar to that assumed by Liao and Kuo (127), who assumed a stimulus-response to characterize acute adaptation of coronary arterioles to various stimuli. Our adaptive equation (*Eq. 38*) relies on a "black box" sensitivity (α), of which the mechanism is not assumed. Although limited data exists of the chronic response of microvessels to pulsatile endothelial shear, endothelial cells respond differently when exposed to pulsatile or steady shear stress (218, 225). Vascular smooth muscle cell hypertrophy has been related to lower speeds of continuous-flow left ventricular assist devices (120) and changes in endothelial shape, alignment, and eNOS expression have been reported with pulsatile flows (149). Increased inflammation (136) and expression of factors linked to arterial remodeling (31) have been observed with increases in pulsatile flow. In vivo studies have reported increased expression of nitric oxide with at higher levels of pulsatility (131, 154, 167). This differential sensitivity to pulsatile and mean endothelial shear stress suggests that there is a mechanism inherent in endothelial cells allowing sensitivity to mean shear stress (β) to be different from sensitivity to pulsatile shear stress (α) in our assumed adaptive response (*Eq. 43*). It is interesting to note that it can be inferred from *Eq. 47* that if $\beta \approx \alpha\left(\Delta\tilde{P}/\Delta\bar{P}\right)(R_L/|Z_L|)^{1/4}$, microvascular responses to pulsatile and mean endothelial

shear stresses would be similar. Thus a relatively higher sensitivity to shear stress (α) can make adaptation to pulsatile shear stress significant, even when pulsatile pressure may be low compared to mean pressure.

Although the arteriolar network model is a simple approximation of the microvasculature, it reproduces measured pressures and flows. Bifurcating models are frequently used to illustrate how microvascular networks structurally adapt to mechanical stresses (71, 93, 106, 211). A bifurcating model, however, is not a true representation of the architecture of the microvascular networks. The microvasculature in most organs (71, 204) are far more interconnected and contain many collateral vessels. However, for much of the small arteries and larger arterioles, vessels do roughly follow bifurcating branching schemes (71), allowing our model to approximate portions of an arteriolar network. In addition, our bifurcating model reproduces measured mean pressures and flows from other microcirculations (Fig. 20). Our model indicates that adaptation to pulsatile endothelial shear stress will reproduce basic properties of a branching network, such as a decreasing downstream radii (Fig. 22). Although our results only apply to a small idealized portion of an arteriolar network, adaptation to mean shear stress in the same idealized network was reported to result in abnormal architecture (204), a result that is recapitulated in Fig. 23 when pulsatility is abolished.

Adaptation to low levels of pulsatility reflect conditions common to chronic disease states with low pulsatility. Given the inability to remove competing adaptive responses in vivo, model results in the present work (i.e., Fig. 23) cannot be validated experimentally in intact vasculatures. Nonetheless, results are consistent with a large

number of clinical and experimental observations. Decreased pulsatility is observed with continuous-flow ventricular assist devices (244), Fontan circulations (101) continuous-flow cardio-pulmonary bypass (125), heart failure (294), and downstream of aortic co-arctations (189). Although these conditions are diverse, they are associated with similar behaviors that manifest in the present work. Decreased microvascular perfusion and capillary rarefaction have been reported in Fontan circulations (101) and with continuous-flow cardio-pulmonary bypass (125). Increased microvascular resistance has been observed in pulmonary microvasculatures in Fontan circulations (101), and microvascular rarefaction has been noted to increase total network resistance (78). Increased incidence of arteriovenous malformations were noted in Fontan circulations (101, 295), and after implantation of continuous-flow left-ventricular assist devices (134, 268). Increased gastrointestinal bleeding, believed to be linked to arteriovenous malformation rupture, are widely observed in Fontan circulations (101, 295) and with continuous-flow left-ventricular assist devices (42, 98). Although there is enormous complexity of the clinical picture in each of these conditions, taken together, they suggest that pulsatility is playing a critical role in maintaining microvascular network stability. When pulsatility is removed (Fig. 23), our model also reproduces increased resistance, capillary rarefaction, and arteriovenous shunts characteristic of arteriovenous malformations.

Size and frequency-dependent viscosity plays a negligible role in microvascular adaptation to shear stress. Although viscosity can be assumed to be constant in larger arteries, the small size of vessels in the microcirculation relative to red blood cells leads

to large changes in viscosity. Numerous experiments have shown blood viscosity varies in the microcirculation, generally ascribed to the effect of two separate actions: the Fahreus-Lindquist effect, and phase separation (201). The effect of viscosity variation on mean flow and endothelial shear stress are well-documented (201). Pries et al. provided a widely used empirical approximation for viscosity (193, 201, 236) dependent on vessel diameter, which we implemented in our model. In general, apparent viscosity increases in the microvasculature, which increases shear stress. The increase in shear stress would be expected to increase stability of two parallel vessels, acting similarly to an increase in the imposed pressure gradient (Fig. 19). Viscosity may also be frequency-dependent in the microcirculation. Womersley reported that the effect of apparent viscosity causes the phase velocity in peripheral vessels to decrease, and thus affect local reflection at bifurcations (292). We tested the effect of Womersley's frequency-dependent viscosity (292) in our model to determine if viscosity changes with frequency play a significant role in adaptive stability (results not shown). Although the changes in apparent viscosity with both diameter and frequency contribute simulation accuracy, their inclusion or exclusion was found to have a negligible effect on the general behavior of adaptation to pulsatile endothelial shear stress.

Adaptation of venous and capillary vessels in normal circulations to pulsatility appears unlikely. Although significant levels of pulsatility reach the arterioles, in normal circulations the arterioles act to filter out pulsatility transmitted to the venous system (175). Both measurements and mathematical models of microcirculations have indicated a large decrease in pulsatility at the level of capillaries and veins (175, 193). In fact, it is

believed that this is necessary to prevent structural damage, with the prevailing theory for malperfusion seen in hypertension being damage caused by the excess pulsatility reaching the capillaries (63, 183). In addition, vasomotion plays a large role in the veins, with the majority of the measured pulsatile component of pressure and flow due to the periodic contraction and relaxation of venules (272), making it unlikely they are adapting to the pulse that are transmitted from the heart. Although venous remodeling is observed with reduced pulsatility in the pulmonary vasculature (101), conventional mathematical models that simulate structural adaptation of capillaries and venules suggest that metabolites dominate all other adaptive stimuli (106, 272). Taken together, adaptation of veins and capillaries to pulsatile endothelial shear stress is not likely to be physiologically relevant.

Future research is necessary to understand adaptation to pulsatile endothelial shear stress. With reports that low pulse pressure predicts death in heart failure patients (294) and adoption of continuous-flow left ventricular assist devices (227), the effect of pulsatile hemodynamics is becoming relevant to ever larger segments of the population. Although this work provides a mathematical basis for adaptation to pulsatile endothelial shear stress in the microcirculation, future work must explore adaptation to pulsatile endothelial shear stress in more complex networks. Vessels in the microvasculature present an intricate, interconnected network, with multiple collateral vessels and multiple competing stimuli of adaptation. Although pulsatility may enhance the stability of a bifurcating network of arterioles, the present work leads to a new question the role of pulsatile shears stress collateral vessels. In addition, interaction of this particular

adaptive response with stimuli and pulsatile endothelial shear stress remains to be explored. The present work presents a novel framework for future modeling studies by providing 1) a tractable approximation for pulsatile shear stress in the microvasculature (*Eqs. 45* and *50*), 2) an explicit relationship of the mechanics governing pulsatile endothelial stress to the mechanics governing mean shear stress (*Eqs. 29* and *33*), and 3) a physiologically-relevant adaptive rule that can be easily conceptualized as a graphical balance point (Fig. 17). Perhaps more importantly, this work has provided a justification for focusing experimental approaches to studying the effects of pulsatile shear stress. Although clinical evidence supports our model's conclusions, experimental measurements characterizing the direct effect of a chronic decrease in pulsatility in a microvasculature network is lacking. This work presents the conceptual basis for adaptation to pulsatile endothelial shear stress, demonstrating that adaptation of arterioles to pulsatile endothelial shear stress is not only possible, but is likely playing a role in maintaining structural stability of arterial networks.

5. CONCLUSIONS

Mathematical models allow replication of the physiology of chronic heart failure to provide general insights. As conventional animal models are limited, mathematical modeling allows both clarification and insights into chronic heart failure. Therefore, the purpose of this work was to: 1) develop general algebraic formulas that predict the interaction of cardiac output and venous return when systemic arterial pressure is chronically regulated, 2) integrate algebraic characterizations of the minimal closed-loop and interstitial fluid balance models to identify the primary mechanical determinants of pulmonary interstitial pressures in healthy subjects and subjects with compensated heart failure, 3) test the hypothesis that adaptation of arterioles to pulsatile endothelial shear stress can enhance structural stability of an arteriolar network, and decreasing pulsatility can increase peripheral resistance, cause rarefaction, and lead to arteriovenous shunts.

First, Guyton's cardiac output-venous return curves were quantified for chronic time periods, and thus made applicable to heart failure without multiple assumed parameters. Constraining the complexity of the closed-loop model yielded general algebraic formulas for cardiac output and systemic venous pressure. Furthermore, applying simplifying strategies yielded a novel alternative to Guyton's classical graph. Cardiac output and venous return curves can now be predicted from parameters characterizing the mechanical properties of the closed-loop system, and their interaction characterizes chronic conditions such as heart failure. The model thus provides

analytical formulas accessible to investigators, clinicians, and students that are conceptually tractable, generally applicable, and physiologically relevant.

Second, pulmonary capillary pressure, pulmonary venous pressure, and pulmonary interstitial pressure can now be found as a function of cardiac and interstitial parameters, directly relating changes in the cardiac system to the interstitium. In addition, pulmonary interstitial pressure is shown to largely be influenced by microvascular parameters. Microvascular and vascular parameters were arranged into non-dimensional terms, decreasing reliance on specific parameter values, especially for the interstitium where parameters are not well known.

Third, microvascular arterioles were found to have enhanced stability when adapting to pulsatile endothelial shear stress with a linear adaptive balance point. Pulsatile endothelial shear stress was found to exhibit behavior similar to steady shear, with stable adaptation occurring in a single vessel and two vessels in series. Adaptation to two vessels in parallel had conditional stability depending on the balance of adaptive parameters, input pressures, and the terminal load downstream of the vessel. As input pulsatility decreased into the arteriolar network, increased peripheral resistance and behavior of the network was predicted similar to that seen with capillary rarefaction and arteriovenous shunts.

By representing forces as a balance point, the complexity of each part became easier to conceptualize and understand how equilibrium emerges. Taken together, applying a physiological balance point approach to heart failure allowed clarification of the interaction of hemodynamics, blood volumes, and adaptation during heart failure.

REFERENCES

1. **Abdolrazaghi M, Navidbakhsh M, Hassani K**. Mathematical modelling and electrical analog equivalent of the human cardiovascular system. *Cardiovasc Eng* 10: 45-51, 2010.

2. **Aman J, Groeneveld ABJ, van Nieuw Amerongen GP**. Revised Starling equation predicts pulmonary edema formation during fluid loading in the critically ill with presumed hypovolemia. *Crit Care Med* 40: 2742-2742, 2012.

3. **Ando J, Yamamoto K**. Vascular mechanobiology: Endothelial cell responses to fluid shear stress. *Circ J* 73: 1983-1992, 2009.

4. **Androne AS, Hryniewicz K, Hudaihed A, Mancini D, Lamanca J, Katz SD**. Relation of unrecognized hypervolemia in chronic heart failure to clinical status, hemodynamics, and patient outcomes. *Am J Cardiol* 93: 1254-1259, 2004.

5. **Armstrong PW, Stopps TP, Ford SE, de Bold AJ**. Rapid ventricular pacing in the dog: Pathophysiologic studies of heart failure. *Circulation* 74: 1075-1084, 1986.

6. **Arquès S, Ambrosi P, Gélisse R, Luccioni R, Habib G**. Hypoalbuminemia in elderly patients with acute diastolic heart failure. *J Am Coll Cardiol* 42: 712-716, 2003.

7. **Astrand H, Rydén-Ahlgren A, Sandgren T, Länne T**. Age-related increase in wall stress of the human abdominal aorta: An in vivo study. *J Vasc Surg* 42: 926-931, 2005.

8. **Aukland K, Reed RK**. Interstitial-lymphatic mechanisms in the control of extracellular fluid volume. *Physiol Rev* 1993.

9. **Averina VA, Othmer HG, Fink GD, Osborn JW**. A new conceptual paradigm for the hemodynamics of salt-sensitive hypertension: A mathematical modeling approach. *J Physiol* 590: 5975-5992, 2012.

10. **Baba A, Dobsak P, Mochizuki S, Saito I, Isoyama T, Takiura K, Shibata M, Abe Y, Chinzei T, Vasku J, Imachi K**. Evaluation of pulsatile and nonpulsatile flow in microvessels of the bulbar conjunctiva in the goat with an undulation pump artificial heart. *Artif Organs* 27: 875-881, 2003.

11. **Baric D**. Why pulsatility still matters: a review of current knowledge. *Croat Med J* 55: 609-620, 2014.

12. **Barrett KE, Boitano S, Barman SM, Brooks H**. *Ganong's Review of Medical Physiology*. New York, NY: Mcgraw-Hill Companies, Inc., 2012.

13. **Batzel JJ, Kappel F, Timischl-Teschl S**. A cardiovascular-respiratory control system model including state delay with application to congestive heart failure in humans. *J Math Biol* 50: 293-335, 2005.

14. **Beard Da, Feigl EO**. Understanding Guyton's venous return curves. *Am J Physiol Heart Circ Physiol* 301: H629-633, 2011.

15. **Beck KC, Lai-Fook SJ**. Effect of height on alveolar liquid pressure in isolated edematous dog lung. *J Appl Physiol Respir Environ Exerc Physiol* 54: 619-622, 1983.

16. **Berger DS, Li JK, Laskey WK, Noordergraaf A**. Repeated reflection of waves in the systemic arterial system. *Am J Physiol* 264: H269-281, 1993.

17. **Bergh N, Ekman M, Ulfhammer E, Andersson M, Karlsson L, Jern S**. A new biomechanical perfusion system for ex vivo study of small biological intact vessels. *Ann Biomed Eng* 33: 1808-1818, 2005.

18. **Berne RM, Koeppen BM, Stanton BA**. *Berne & Levy Physiology*. Philadelphia, PA: Mosby/Elsevier, 2010.

19. **Beyar R, Hausknecht MJ, Halperin HR, Yin FC, Weisfeldt ML**. Interaction between cardiac chambers and thoracic pressure in intact circulation. *Am J Physiol* 253: H1240-1252, 1987.

20. **Beyar R, Kishon Y, Sideman S, Dinnar U**. Computer studies of systemic and regional blood flow mechanisms during cardiopulmonary resuscitation. *Med Biol Eng Comput* 22: 499-506, 1984.

21. **Beyar R, Sideman S**. Model for left ventricular contraction combining the force length velocity relationship with the time varying elastance theory. *Biophys J* 45: 1167-1177, 1984.

22. **Bhattacharya J, Gropper MA, Staub NC**. Interstitial fluid pressure gradient measured by micropuncture in excised dog lung. *J Appl Physiol Respir Environ Exerc Physiol* 56: 271-277, 1984.

23. **Borlaug BA, Kass DA**. Ventricular-vascular interaction in heart failure. *Heart Fail Clin* 4: 23-36, 2008.

24. **Borlaug BA, Paulus WJ**. Heart failure with preserved ejection fraction: Pathophysiology, diagnosis, and treatment. *Eur Heart J* 32: 670-679, 2011.

25. **Borlaug BA, Redfield MM**. Diastolic and systolic heart failure are distinct phenotypes within the heart failure spectrum. *Circulation* 123: 2006-2013; discussion 2014, 2011.

26. **Brengelmann GL**. A critical analysis of the view that right atrial pressure determines venous return. *J Appl Physiol* 94: 849-859, 2003.

27. **Bressack MA, Raffin TA**. Importance of venous return, venous resistance, and mean circulatory pressure in the physiology and management of shock. *Chest* 92: 906-912, 1987.

28. **Brown DJ**. Input impedance and reflection coefficient in fractal-like models of asymmetrically branching compliant tubes. *IEEE Trans Biomed Eng* 43: 715-722, 1996.

29. **Bui A, Sutalo ID, Manasseh R, Liffman K**. Dynamics of pulsatile flow in fractal models of vascular branching networks. *Med Biol Eng Comput* 47: 763-772, 2009.

30. **Burkhoff D, Tyberg JV**. Why does pulmonary venous pressure rise after onset of LV dysfunction: A theoretical analysis. *Am J Physiol Heart Circ Physiol* 265: H1819-H1828, 1993.

31. **Buschmann I, Pries A, Styp-Rekowska B, Hillmeister P, Loufrani L, Henrion D, Shi Y, Duelsner A, Hoefer I, Gatzke N, Wang H, Lehmann K, Ulm L, Ritter Z, Hauff P, Hlushchuk R, Djonov V, van Veen T, le Noble F**. Pulsatile shear and Gja5 modulate arterial identity and remodeling events during flow-driven arteriogenesis. *Development* 137: 2187-2196, 2010.

32. **Busse R, Fleming I**. Pulsatile stretch and shear stress: Physical stimuli determining the production of endothelium-derived relaxing factors. *J Vasc Res* 35: 73-84, 1998.

33. **Carlson DE, Kligman MD, Gann DS**. Impairment of blood volume restitution after large hemorrhage: a mathematical model. *Am J Physiol* 270: R1163-1177, 1996.

34. **Cecchini ABP, Melbin J, Noordergraaf A**. Set-point: Is it a distinct structural entity in biological control? *J Theor Biol* 93: 387-394, 1981.

35. **Chakko S, Woska D, Martinez H, de Marchena E, Futterman L, Kessler KM, Myerberg RJ**. Clinical, radiographic, and hemodynamic correlations in chronic congestive heart failure: conflicting results may lead to inappropriate care. *Am J Med* 90: 353-359, 1991.

36. **Chen JJS, Heldt T, Verghese GC, Mark RG**. Analytical solution to a simplified circulatory model using piecewise linear elastance function. *Comput Cardiol* 45-48, 2003.

37. **Cobelli C, Carson E**. Modeling the system. In: *Introduction to Modeling in Physiology and Medicine*. Burlington, MA: Academic Press, 2008, p. 75-157.

38. **Cobelli C, Carson E**. Models and the modeling process. In: *Introduction to Modeling in Physiology and Medicine*. Burlington, MA: Academic Press, 2008, p. 23-34.

39. **Cobelli C, Carson E**. Physiological complexity and the need for models. In: *Introduction to Modeling in Physiology and Medicine*. Burlington, MA: Academic Press, 2008, p. 7-22.

40. **Cody RJ, Covit AB, Schaer GL, Laragh JH, Sealey JE, Feldschuh J**. Sodium and water balance in chronic congestive heart failure. *J Clin Invest* 77: 1441-1452, 1986.

41. **Copetti R, Soldati G, Copetti P**. Chest sonography: A useful tool to differentiate acute cardiogenic pulmonary edema from acute respiratory distress syndrome. *Cardiovasc Ultrasound* 6: 16, 2008.

42. **Crow S, Chen D, Milano C, Thomas W, Joyce L, Piacentino V, 3rd, Sharma R, Wu J, Arepally G, Bowles D, Rogers J, Villamizar-Ortiz N**. Acquired von Willebrand syndrome in continuous-flow ventricular assist device recipients. *Ann Thorac Surg* 90: 1263-1269; discussion 1269, 2010.

43. **Crow S, Milano C, Joyce L, Chen D, Arepally G, Bowles D, Thomas W, Ortiz NV**. Comparative analysis of von Willebrand factor profiles in pulsatile and continuous left ventricular assist device recipients. *ASAIO J* 56: 441-445, 2010.

44. **Davies SW, Bailey J, Keegan J, Balcon R, Rudd RM, Lipkin DP**. Reduced pulmonary microvascular permeability in severe chronic left heart failure. *Am Heart J* 124: 137-142, 1992.

45. **Dawant B, Levin M, Popel AS**. Effect of dispersion of vessel diameters and lengths in stochastic networks. *Microvasc Res* 31: 203-222, 1986.

46. **Demirozu ZT, Radovancevic R, Hochman LF, Gregoric ID, Letsou GV, Kar B, Bogaev RC, Frazier OH**. Arteriovenous malformation and gastrointestinal bleeding in patients with the HeartMate II left ventricular assist device. *J Heart Lung Transplant* 30: 849-853, 2011.

47. **Deswal A**. Diastolic dysfunction and diastolic heart failure: Mechanisms and epidemiology. *Curr Cardiol Rep* 178-183, 2005.

48. **Dexter L, Dow JW, Haynes FW, Whittenberger JL, Ferris BG, Goodale WT, Hellems HK**. Studies of the pulmonary circulation in man at rest; Normal

variations and the interrelations between increased pulmonary blood flow, elevated pulmonary arterial pressure, and high pulmonary 'capillary" pressures. *J Clin Invest* 29: 602-613, 1950.

49. **Dongaonkar RM, Laine GA, Stewart RH, Quick CM**. Balance point characterization of interstitial fluid volume regulation. *Am J Physiol Regul Integr Comp Physiol* 297: R6-16, 2009.

50. **Dongaonkar RM, Quick CM, Stewart RH, Drake RE, Cox CS, Jr., Laine GA**. Edemagenic gain and interstitial fluid volume regulation. *Am J Physiol Regul Integr Comp Physiol* 294: R651-659, 2008.

51. **Dorrington KL, Pandit JJ**. The obligatory role of the kidney in long-term arterial blood pressure control: Extending Guyton's model of the circulation. *Anaesthesia* 64: 1218-1228, 2009.

52. **Drake RE, Adcock DK, Scott RL, Gabel JC**. Effect of outflow pressure upon lymph flow from dog lungs. *Circ Res* 50: 865-869, 1982.

53. **Drake RE, Allen SJ, Williams JP, Laine GA, Gabel JC**. Lymph flow from edematous dog lungs. *J Appl Physiol* 62: 2416-2420, 1987.

54. **Drake RE, Gabel JC**. Effect of outflow pressure on liver lymph flow in unanesthetized sheep. *Am J Physiol* 259: R780-785, 1990.

55. **Drake RE, Teague RA, Gabel JC**. Lymphatic drainage reduces intestinal edema and fluid loss. *Lymphology* 31: 68-73, 1998.

56. **Drake RE, Weiss D, Gabel JC**. Active lymphatic pumping and sheep lung lymph flow. *J Appl Physiol* 71: 99-103, 1991.

57. **Efstratiadis S, Michaels AD**. Acute hemodynamic effects of intravenous nesiritide on left ventricular diastolic function in heart failure patients. *J Card Fail* 15: 673-680, 2009.

58. **Elbers PW, Wijbenga J, Solinger F, Yilmaz A, van Iterson M, van Dongen EP, Ince C**. Direct observation of the human microcirculation during cardiopulmonary bypass: effects of pulsatile perfusion. *J Cardiothorac Vasc Anesth* 25: 250-255, 2011.

59. **Ellwein LM, Pope SR, Xie A, Batzel J, Kelley CT, Olufsen MS**. Modeling cardiovascular and respiratory dynamics in congestive heart failure. *Math Biosci* 241: 56-74, 2013.

60. **Esper RJ, Nordaby RA, Vilariño JO, Paragano A, Cacharrón JL, Machado RA**. Endothelial dysfunction: A comprehensive appraisal. *Cardiovasc Diabetol* 5: 4-4, 2006.

61. **Fauchald P**. Colloid osmotic pressures, plasma volume and interstitial fluid volume in patients with heart failure. *Scand J Clin Lab Invest* 45: 701-706, 1985.

62. **Feeley T, Frederick M, Halperin B, Rosenthal M**. Failure of the colloid oncotic-pulmonary artery wedge pressure gradient to predict changes in extravascular lung water. *Crit Care Med* 13: 1025-1028, 1985.

63. **Feihl F, Liaudet L, Waeber B**. The macrocirculation and microcirculation of hypertension. *Curr Hypertens Rep* 11: 182-189, 2009.

64. **Felker GM, Pang PS, Adams KF, Cleland JGF, Cotter G, Dickstein K, Filippatos GS, Fonarow GC, Greenberg BH, Hernandez AF, Khan S, Komajda M, Konstam Ma, Liu PP, Maggioni AP, Massie BM, McMurray JJ, Mehra M, Metra M, O'Connell J, O'Connor CM, Pina IL, Ponikowski P, Sabbah HN, Teerlink JR, Udelson JE, Yancy CW, Zannad F, Gheorghiade M**. Clinical trials of pharmacological therapies in acute heart failure syndromes lessons learned and directions forward. *Circ Heart Fail* 3: 314-325, 2010.

65. **Ferrari R, Bohm M, Cleland JG, Paulus WJ, Pieske B, Rapezzi C, Tavazzi L**. Heart failure with preserved ejection fraction: Uncertainties and dilemmas. *Eur J Heart Fail* 17: 665-671, 2015.

66. **Fletcher R**. *Practical Methods of Optimization*. New York, NY: Wiley-Interscience, 1987.

67. **Frasch HF, Kresh JY, Noordergraaf A**. Wave transmission and input impedance of a model of skeletal muscle microvasculature. *Ann Biomed Eng* 22: 45-57, 1994.

68. **Frasch HF, Kresh JY, Noordergraaf A**. Two-port analysis of microcirculation: An extension of windkessel. *Am J Physiol* 270: H376-385, 1996.

69. **Gaar KA, Taylor AE, Owens LJ, Guyton AC**. Effect of capillary pressure and plasma protein on development of pulmonary edema. *Am J Physiol* 213: 79-82, 1967.

70. **Gaehtgens P**. Pulsatile pressure and flow in the mesenteric vascular bed of the cat. *Pflugers Arch* 316: 140-151, 1970.

71. **Gan RZ, Yen RT**. Vascular impedance analysis in dog lung with detailed morphometric and elasticity data. *J Appl Physiol* 77: 706-717, 1994.

72. **Ganesan P, He S, Xu H**. Modelling of pulsatile blood flow in arterial trees of retinal vasculature. *Med Eng Phys* 33: 810-823, 2011.

73. **Gargani L, Pang PS, Frassi F, Miglioranza MH, Dini FL, Landi P, Picano E**. Persistent pulmonary congestion before discharge predicts rehospitalization in heart failure: A lung ultrasound study. *Cardiovasc Ultrasound* 13: 40-40, 2015.

74. **Gehlbach B, Geppert E**. Pulmonary manifestations of left heart failure. *Chest* 125: 669-682, 2004.

75. **Gehlbach BK**. The Cardiovascular System. In: *Handbook of Critical Care*, edited by Hall JB. London, England: Springer-Verlag, 2009, p. 15-52.

76. **Georgiopoulou VV, Kalogeropoulos AP, Borlaug BA, Gheorghiade M, Butler J**. Left ventricular dysfunction with pulmonary hypertension: Part 1: Epidemiology, pathophysiology, and definitions. *Circ Heart Fail* 6: 344-354, 2013.

77. **Godde R, Kurz H**. Structural and biophysical simulation of angiogenesis and vascular remodeling. *Dev Dyn* 220: 387-401, 2001.

78. **Greene AS, Tonellato PJ, Lui J, Lombard JH, Cowley AW, Jr.** Microvascular rarefaction and tissue vascular resistance in hypertension. *Am J Physiol* 256: H126-131, 1989.

79. **Gross JF, Intaglietta M, Zweifach BW**. Network model of pulsatile hemodynamics in the microcirculation of the rabbit omentum. *Am J Physiol* 226: 1117-1123, 1974.

80. **Guazzi M, Gatto P, Giusti G, Pizzamiglio F, Previtali I, Vignati C, Arena R**. Pathophysiology of cardiorenal syndrome in decompensated heart failure: Role of lung-right heart-kidney interaction. *Int J Cardiol* 169: 379-384, 2013.

81. **Guyton AC**. Determination of cardiac output by equating venous return curves with cardiac response curves. *Physiol Rev* 35: 123-129, 1955.

82. **Guyton AC**. The surprising kidney-fluid mechanism for pressure control--its infinite gain! *Hypertension* 16: 725-730, 1990.

83. **Guyton AC**. Kidneys and fluids in pressure regulation. Small volume but large pressure changes. *Hypertension* 19: I2-I8, 1992.

84. **Guyton AC, Abernathy B, Langston JB, Kaufmann BN, Fairchild HM**. Relative importance of venous and arterial resistances in controlling venous return and cardiac output. *Am J Physiol* 196: 1008-1014, 1959.

85. **Guyton AC, Coleman TG, Cowley AW**. A systems analysis approach to understanding long-range arterial blood pressure control and hypertension. *Circ Res* 35: 159-176, 1974.

86. **Guyton AC, Coleman TG, Granger HJ**. Circulation: Overall regulation. *Annu Rev Physiol* 34: 13-46, 1972.

87. **Guyton AC, Coleman TG, Jones CE**. *Cardiac Output and its Regulation*. London, England: W. B. Saunders, 1973.

88. **Guyton AC, Lindsey AW, Abernathy B, Richardson T**. Venous return at various right atrial pressures and the normal venous return curve. *Am J Physiol* 189: 609-615, 1957.

89. **Guyton AC, Lindsey AW, Kaufmann BN**. Effect of mean circulatory filling pressure and other peripheral circulatory factors on cardiac output. *Am J Physiol* 180: 463-468, 1955.

90. **Guyton AC, Lindsey AW, Kaufmann BN, Abernathy JB**. Effect of blood transfusion and hemorrhage on cardiac output and on the venous return curve. *Am J Physiol* 194: 263-267, 1958.

91. **Gyenge CC, Bowen BD, Reed RK, Bert JL**. Transport of fluid and solutes in the body I. Formulation of a mathematical model. *Am J Physiol* 277: H1215-1227, 1999.

92. **Habazettl H, Kukucka M, Weng Y, Kuebler W, Hetzer R, Kuppe H, Pries A**. Arteriolar blood flow pulsatility in a patient before and after implantation of an axial flow pump. *Ann Thorac Surg* 81: 1109-1111, 2006.

93. **Hacking WJ, VanBavel E, Spaan JA**. Shear stress is not sufficient to control growth of vascular networks: A model study. *Am J Physiol* 270: H364-375, 1996.

94. **Hahn RG**. Volume kinetics for infusion fluids. *Anesthesiology* 113: 470-481, 2010.

95. **Hall JE, Guyton AC**. *Guyton & Hall Physiology Review*. Philadelphia, PA: Elsevier Saunders, 2011.

96. **Hara N, Nagashima A, Yoshida T, Furukawa T, Inokuchi K**. Effect of decreased plasma colloid osmotic pressure on development of pulmonary edema in dogs. *Jpn J Surg* 11: 203-208, 1981.

97. **Harvey RC**. Narcotic agonists and antagonists. In: *Small Animal Critical Care Medicine*, edited by Silverstein KB, Hopper DCT. Saint Louis, MO: W.B. Saunders, 2009, p. 784-789.

98. **Hayes HM, Dembo LG, Larbalestier R, O'Driscoll G**. Management options to treat gastrointestinal bleeding in patients supported on rotary left ventricular assist devices: A single-center experience. *Artif Organs* 34: 703-706, 2010.

99. **Heldt T, Mukkamala R, Moody GB, Mark RG**. Cvsim: An open-source cardiovascular simulator for teaching and research. *Open Pacing Electrophysiol Ther J* 3: 45-45, 2010.

100. **Heldt T, Shim EB, Kamm RD, Mark RG**. Computational modeling of cardiovascular response to orthostatic stress. *J Appl Physiol* 92: 1239-1254, 2002.

101. **Henaine R, Vergnat M, Bacha EA, Baudet B, Lambert V, Belli E, Serraf A**. Effects of lack of pulsatility on pulmonary endothelial function in the Fontan circulation. *J Thorac Cardiovasc Surg* 146: 522-529, 2013.

102. **Henderson WR, Griesdale DEG, Walley KR, Sheel AW**. Clinical review: Guyton--the role of mean circulatory filling pressure and right atrial pressure in controlling cardiac output. *Crit Care* 14: 243-243, 2010.

103. **Hendrickson RJ, Cappadona C, Yankah EN, Sitzmann JV, Cahill PA, Redmond EM**. Sustained pulsatile flow regulates endothelial nitric oxide synthase and cyclooxygenase expression in co-cultured vascular endothelial and smooth muscle cells. *J Mol Cell Cardiol* 31: 619-629, 1999.

104. **Hiesmayr M, Jansen JRC, Versprille A**. Effects of endotoxin infusion on mean systemic filling pressure and flow resistance to venous return. *Pflugers Arch* 431: 741-747, 1996.

105. **Houstis NE, Lewis GD**. Causes of exercise intolerance in heart failure with preserved ejection fraction: Searching for consensus. *J Card Fail* 20: 762-778, 2014.

106. **Hu D, Cai D, Rangan AV**. Blood vessel adaptation with fluctuations in capillary flow distribution. *PLoS One* 7: e45444, 2012.

107. **Huang W, Kingsbury MP, Turner Ma, Donnelly JL, Flores Na, Sheridan DJ**. Capillary filtration is reduced in lungs adapted to chronic heart failure: Morphological and haemodynamic correlates. *Cardiovasc Res* 49: 207-217, 2001.

108. **Hudetz AG, Kiani MF**. The role of wall shear stress in microvascular network adaptation. *Adv Exp Med Biol* 316: 31-39, 1992.

109. **Huo Y**. Pulsatile blood flow in the entire coronary arterial tree: theory and experiment. *Am J Physiol Heart Circ Physiol* 291: H1074-H1087, 2006.

110. **Hyde RW, Wandtke JC, Fahey PJ, Utell MJ, Plewes DB, Goske M**. Lung weight in vivo measured with computed tomography and rebreathing of soluble gases. *J Appl Physiol* 67: 166-173, 1989.

111. **Intaglietta M, Richardson DR, Tompkins WR**. Blood pressure, flow, and elastic properties in microvessels of cat omentum. *Am J Physiol* 221: 922-928, 1971.

112. **Jacobsen JC, Gustafsson F, Holstein-Rathlou NH**. A model of physical factors in the structural adaptation of microvascular networks in normotension and hypertension. *Physiol Meas* 24: 891-912, 2003.

113. **Jacobsen JC, Hornbech MS, Holstein-Rathlou NH**. A tissue in the tissue: Models of microvascular plasticity. *Eur J Pharm Sci* 36: 51-61, 2009.

114. **Jellinek H, Krenn H, Oczenski W, Veit F, Schwarz S, Fitzgerald RD**. Influence of positive airway pressure on the pressure gradient for venous return in humans. *J Appl Physiol* 88: 926-932, 2000.

115. **Ji B, Undar A**. Comparison of perfusion modes on microcirculation during acute and chronic cardiac support: Is there a difference? *Perfusion* 22: 115-119, 2007.

116. **Kalogeropoulos AP, Georgiopoulou VV, Borlaug Ba, Gheorghiade M, Butler J**. Left ventricular dysfunction with pulmonary hypertension part 2: Prognosis, noninvasive evaluation, treatment, and future research. *Circ Heart Fail* 6: 584-593, 2013.

117. **Karsaj I, Soric J, Humphrey JD**. A 3-D framework for arterial growth and remodeling in response to altered hemodynamics. *Int J Eng Sci* 48: 1357-1372, 2010.

118. **Katz AM**. Ernest Henry Starling, his predecessors, and the "Law of the Heart." *Circulation* 106: 2986-2992, 2002.

119. **Katz SD**. Blood volume assessment in the diagnosis and treatment of chronic heart failure. *Am J Med Sci* 334: 47-52, 2007.

120. **Kihara S, Litwak KN, Nichols L, Litwak P, Kameneva MV, Wu Z, Kormos RL, Griffith BP**. Smooth muscle cell hypertrophy of renal cortex arteries with chronic continuous flow left ventricular assist. *Ann Thorac Surg* 75: 178-183, 2003.

121. **Klotz S, Hay I, Dickstein ML, Yi G-H, Wang J, Maurer MS, Kass Da, Burkhoff D**. Single-beat estimation of end-diastolic pressure-volume relationship: A novel method with potential for noninvasive application. *Am J Physiol Heart Circ Physiol* 291: H403-H412, 2006.

122. **Kofranek J, Matousek S, Rusz J, Stodulka P, Privitzer P, Matejak M, Tribula M**. The atlas of physiology and pathophysiology: Web-based multimedia enabled interactive simulations. *Comput Methods Programs Biomed* 104: 143-153, 2011.

123. **Koller A, Huang A**. Development of nitric oxide and prostaglandin mediation of shear stress-induced arteriolar dilation with aging and hypertension. *Hypertension* 1999.

124. **Komamura K**. Similarities and differences between the pathogenesis and pathophysiology of diastolic and systolic heart failure. *Cardiol Res Pract* 2013: 824135, 2013.

125. **Koning NJ, Vonk AB, van Barneveld LJ, Beishuizen A, Atasever B, van den Brom CE, Boer C**. Pulsatile flow during cardiopulmonary bypass preserves postoperative microcirculatory perfusion irrespective of systemic hemodynamics. *J Appl Physiol* 112: 1727-1734, 2012.

126. **Kresh JY, Izrailtyan I, Morris RJ, Wechsler AS**. Vascular determinants of univentricular support. *ASAIO J* 44: M330-M335, 1998.

127. **Kuo L, Liao JC**. Interaction between adenosine and flow-induced dilation in coronary microvascular network. *Am J Physiol Heart Circ Physiol* 272: H1571-H1581, 1997.

128. **Ky B, French B, May Khan A, Plappert T, Wang A, Chirinos JA, Fang JC, Sweitzer NK, Borlaug BA, Kass DA, Sutton MSJ, Cappola TP**. Ventricular-arterial coupling, remodeling, and prognosis in chronic heart failure. *J Am Coll Cardiol* 62: 1165-1172, 2013.

129. **Lai-Fook SJ, Rodarte JR**. Pleural pressure distribution and its relationship to lung volume and interstitial pressure. *J Appl Physiol* 70: 967-978, 1991.

130. **Laine GA, Allen SJ, Katz J, Gabel JC, Drake RE**. Effect of systemic venous pressure elevation on lymph flow and lung edema formation. *J Appl Physiol* 61: 1634-1638, 1986.

131. **Lanzarone E, Gelmini F, Tessari M, Menon T, Suzuki H, Carini M, Costantino ML, Fumero R, Luciani GB, Faggian G**. Preservation of endothelium nitric oxide release by pulsatile flow cardiopulmonary bypass when compared with continuous flow. *Artif Organs* 33: 926-934, 2009.

132. **Ledder G**. Mathematical modeling. In: *Mathematics for the Life Sciences*. New York, NY: Springer, 2013, p. 83-143.

133. **Lee JJ, Tyml K, Menkis AH, Novick RJ, McKenzie FN**. Evaluation of pulsatile and nonpulsatile flow in capillaries of goat skeletal muscle using intravital microscopy. *Microvasc Res* 48: 316-327, 1994.

134. **Letsou GV, Shah N, Gregoric ID, Myers TJ, Delgado R, Frazier OH**. Gastrointestinal bleeding from arteriovenous malformations in patients supported by the Jarvik 2000 axial-flow left ventricular assist device. *J Heart Lung Transplant* 24: 105-109, 2005.

135. **Li JK**. *Comparative Cardiovascular Dynamics of Mammals*. Boca Raton, FL: CRC Press, 1995, p. 176.

136. **Li M, Scott DE, Shandas R, Stenmark KR, Tan W**. High pulsatility flow induces adhesion molecule and cytokine mRNA expression in distal pulmonary artery endothelial cells. *Ann Biomed Eng* 37: 1082-1092, 2009.

137. **Liang F, Liu H**. A closed-loop lumped parameter computational model for human cardiovascular system. *JSME Int J, Ser C* 48: 484-493, 2005.

138. **Liao S, von der Weid PY**. Lymphatic system: An active pathway for immune protection. *Semin Cell Dev Biol* 1-7, 2015.

139. **Lim E, Chan GSH, Dokos S, Ng SC, Latif LA, Vandenberghe S, Karunanithi M, Lovell NH**. A cardiovascular mathematical model of graded head-up tilt. *PLoS One* 8: e77357, 2013.

140. **Lipowsky HH, Kovalcheck S, Zweifach BW**. The distribution of blood rheological parameters in the microvasculature of cat mesentery. *Circ Res* 43: 738-749, 1978.

141. **Lipowsky HH, Zweifach BW**. Network analysis of microcirculation of cat mesentery. *Microvasc Res* 7: 73-83, 1974.

142. **Lohmeier TE, Iliescu R**. Lowering of blood pressure by chronic suppression of central sympathetic outflow: Insight from prolonged baroreflex activation. *J Appl Physiol* 2012.

143. **Lu D, Kassab GS**. Role of shear stress and stretch in vascular mechanobiology. *J R Soc Interface* 8: 1379-1385, 2011.

144. **Lu K, Clark JW, Ghorbel FH, Ware DL, Bidani A**. A human cardiopulmonary system model applied to the analysis of the Valsalva maneuver. *Am J Physiol Heart Circ Physiol* 281: H2661-2679, 2001.

145. **Maas JJ, Geerts BF, van den Berg PCM, Pinsky MR, Jansen JRC**. Assessment of venous return curve and mean systemic filling pressure in postoperative cardiac surgery patients. *Crit Care Med* 37: 912-918, 2009.

146. **Magder S**. Central venous pressure: A useful but not so simple measurement. *Crit Care Med* 34: 2224-2227, 2006.

147. **Magder S, Bafaqeeh F**. The clinical role of central venous pressure measurements. *J Intensive Care Med* 22: 44-51, 2015.

148. **Magder S, Veerassamy S, Bates JHT**. A further analysis of why pulmonary venous pressure rises after the onset of LV dysfunction. *J Appl Physiol* 106: 81-90, 2009.

149. **Malek AM, Alper SL, Izumo S**. Hemodynamic shear stress and its role in atherosclerosis. *JAMA* 282: 2035-2042, 1999.

150. **Mallamaci F, Benedetto FA, Tripepi R, Rastelli S, Castellino P, Tripepi G, Picano E, Zoccali C**. Detection of pulmonary congestion by chest ultrasound in dialysis patients. *JACC Cardiovasc Imaging* 3: 586-594, 2010.

151. **Mantero S, Pietrabissa R, Fumero R**. The coronary bed and its role in the cardiovascular system: A review and an introductory single-branch model. *J Biomed Eng* 14: 109-116, 1992.

152. **Mardel SN, Simpson SH, Kelly S, Wytch R, Beattie TF, Menezes G**. Validation of a computer model of haemorrhage and transcapillary refill. *Med Eng Phys* 17: 215-218, 1995.

153. **Margaris KN, Black RA**. Modelling the lymphatic system: Challenges and opportunities. *J R Soc Interface* 9: 601-612, 2012.

154. **Mathie RT, Ohri SK, Keogh BE, Williams J, Siney L, Griffith TM**. Nitric oxide activity in patients undergoing cardiopulmonary bypass. *J Thorac Cardiovasc Surg* 112: 1394-1395, 1996.

155. **Milkiewicz M, Brown M, Egginton S, Hudlicka O**. Association between shear stress, angiogenesis, and VEGF in skeletal muscles in vivo. *Microcirculation* 8: 229-241, 2001.

156. **Miller WL, Mullan BP**. Understanding the heterogeneity in volume overload and fluid distribution in decompensated heart failure is key to optimal volume management: role for blood volume quantitation. *JACC Heart failure* 2: 298-305, 2014.

157. **Milne EN, Pistolesi M, Miniati M, Giuntini C**. The radiologic distinction of cardiogenic and noncardiogenic edema. *AJR Am J Roentgenol* 144: 879-894, 1985.

158. **Miserocchi G, Negrini D, Del Fabbro M, Venturoli D**. Pulmonary interstitial pressure in intact in situ lung: Transition to interstitial edema. *J Appl Physiol* 74: 1171-1177, 1993.

159. **Miserocchi G, Negrini D, Gonano C**. Direct measurement of interstitial pulmonary pressure in in situ lung with intact pleural space. *J Appl Physiol* 69: 2168-2174, 1990.

160. **Mitzner W, Robotham JL**. Distribution of interstitial compliance and filtration coefficient in canine lung. *Lymphology* 12: 140-148, 1979.

161. **Mohiuddin MW, Laine G, Quick CM**. Increase in pulse wavelength causes the systemic arterial tree to degenerate into a classical windkessel. *Am J Physiol Heart Circ Physiol* 293: H1164-1171, 2007.

162. **Moochhala S, Wu J, Lu J**. Hemorrhagic shock: An overview of animal models. *Front Biosci* 14: 4631-4639, 2009.

163. **Morgan JP, Delnero PF, Zheng Y, Verbridge SS, Chen J, Craven M, Choi NW, Diaz-Santana A, Kermani P, Hempstead B, Lopez JA, Corso TN, Fischbach C, Stroock AD**. Formation of microvascular networks in vitro. *Nat Protoc* 8: 1820-1836, 2013.

164. **Mulvany MJ**. Determinants of vascular structure. *J Cardiovasc Pharmacol* 19 Suppl 5: S1-6, 1992.

165. **Najjar SS, Schulman SP, Gerstenblith G, Fleg JL, Kass Da, O'Connor F, Becker LC, Lakatta EG**. Age and gender affect ventricular-vascular coupling during aerobic exercise. *J Am Coll Cardiol* 44: 611-617, 2004.

166. **Nakano T, Tominaga R, Morita S, Masuda M, Nagano I, Imasaka K, Yasui H**. Impacts of pulsatile systemic circulation on endothelium-derived nitric oxide release in anesthetized dogs. *Ann Thorac Surg* 72: 156-162, 2001.

167. **Nakano T, Tominaga R, Nagano I, Okabe H, Yasui H**. Pulsatile flow enhances endothelium-derived nitric oxide release in the peripheral vasculature. *Am J Physiol Heart Circ Physiol* 278: H1098-H1104, 2000.

168. **Nakata M, Tatsumi E, Tsukiya T, Taenaka Y, Nishimura T, Nishinaka T, Takano H, Masuzawa T, Ohba K**. Augmentative effect of pulsatility on the wall shear stress in tube flow. *Artif Organs* 23: 727-731, 1999.

169. **Neal M, Bassingthwaighte J**. Subject-specific model estimation of cardiac output and blood volume during hemorrhage. *Cardiovasc Eng* 7: 97-120, 2007.

170. **Negrini D, Ballard ST, Benoit JN**. Contribution of lymphatic myogenic activity and respiratory movements to pleural lymph flow. *J Appl Physiol* 76: 2267-2274, 1994.

171. **Negrini D, Del Fabbro M**. Subatmospheric pressure in the rabbit pleural lymphatic network. *J Physiol* 520 Pt 3: 761-769, 1999.

172. **Negrini D, Moriondo A**. Pleural function and lymphatics. *Acta Physiol (Oxf)* 207: 244-259, 2013.

173. **Nguyen PH, Coquis-Knezek SF, Mohiuddin MW, Tuzun E, Quick CM**. The complex distribution of arterial system mechanical properties, pulsatile hemodynamics, and vascular stresses emerges from three simple adaptive rules. *Am J Physiol Heart Circ Physiol* 308: H407-415, 2015.

174. **Nguyen TL**. *Lymphatic functional adaptations to prolonged changes in mechanical stimuli* (Dissertation). College Station, TX: Department of Veterinary Physiology and Pharmacology, Texas A&M University, 2013.

175. **Nichols WW, O'Rourke MF**. *McDonald's Blood Flow in Arteries: Theoretical, Experimental, and Clinical Principles*. New York, NY: Oxford University Press Inc., 2005.

176. **Niedziela J, Hudzik B, Rozentryt P, Niedziela N, Ociessa A, Nowak J, Gasior M**. Calculated colloid osmotic pressure as an independent risk factor of mortality in chronic heart failure (Abstract). Florence, Italy: Heart Failure 2016 and the 3rd World Congress on Acute Heart Failure. *Eur J Heart Fail* 18, S1: 246, 2016.

177. **Niimi H, Komai Y, Yamaguchia S**. Blood flow regulation in the cerebral microvasculature with an arcadal network: A numerical simulation. *Indian J Exp Biol* 45: 41-47, 2007.

178. **Nilsson J, Riedel S**. *Electric Circuits*. Upper Saddle River, NJ: Pearson Prentice Hall, 2008.

179. **Nishida Y, Tandai-Hiruma M, Kemuriyama T, Hagisawa K**. Long-term blood pressure control: Is there a set-point in the brain? *J Physiol Sci* 62: 147-161, 2012.

180. **Nishinaka T, Tatsumi E, Nishimura T, Shioya K, Ohnishi H, Taenaka Y, Takano H**. Change in vasoconstrictive function during prolonged nonpulsatile left heart bypass. *Artif Organs* 25: 371-375, 2001.

181. **Noumi B, Teruya S, Salomon S, Maurer MS**. Blood volume measurements in patients with heart failure and a preserved ejection fraction: Implications for diagnosing anemia. *Congest Heart Fail* 17: 14-18, 2011.

182. **O'Neill WW, Kleiman NS, Moses J, Henriques JP, Dixon S, Massaro J, Palacios I, Maini B, Mulukutla S, Dzavik V, Popma J, Douglas PS, Ohman M**. A prospective, randomized clinical trial of hemodynamic support with Impella 2.5 versus intra-aortic balloon pump in patients undergoing high-risk percutaneous coronary intervention: The PROTECT II study. *Circulation* 126: 1717-1727, 2012.

183. **O'Rourke MF, Safar ME**. Relationship between aortic stiffening and microvascular disease in brain and kidney: Cause and logic of therapy. *Hypertension* 46: 200-204, 2005.

184. **Ogilvie RI, Zborowska-Sluis D**. Effect of chronic rapid ventricular pacing on total vascular capacitance. *Circulation* 85: 1524-1530, 1992.

185. **Olansen JB, Clark JW, Khoury D, Ghorbel F, Bidani A**. A closed-loop model of the canine cardiovascular system that includes ventricular interaction. *Comput Biomed Res* 33: 260-295, 2000.

186. **Olszewski WL**. Contractility patterns of normal and pathologically changed human lymphatics. *Ann N Y Acad Sci* 979: 52-63; discussion 76-59, 2002.

187. **Olufsen MS, Ottesen JT, Tran HT, Ellwein LM, Lipsitz LA, Novak V**. Blood pressure and blood flow variation during postural change from sitting to standing: model development and validation. *J Appl Physiol* 99: 1523-1537, 2005.

188. **Otto S, Day T**. *A Biologist's Guide to Mathematical Modeling in Ecology and Evolution*. Princeton, NJ: Princeton University Press, 2007.

189. **Owens GK, Reidy MA**. Hyperplastic growth response of vascular smooth muscle cells following induction of acute hypertension in rats by aortic coarctation. *Circ Res* 57: 695-705, 1985.

190. **Oyre S, Pedersen E, Ringgaard S, Boesiger P, Paaske W**. In vivo wall shear stress measured by magnetic resonance velocity mapping in the normal human abdominal aorta. *Eur J Vasc Endovasc Surg* 13: 263-271, 1997.

191. **Paeme S, Moorhead KT, Chase JG, Lambermont B, Kolh P, D'Orio V, Pierard L, Moonen M, Lancellotti P, Dauby PC, Desaive T**. Mathematical multi-scale model of the cardiovascular system including mitral valve dynamics. Application to ischemic mitral insufficiency. *Biomed Eng Online* 10: 86, 2011.

192. **Palladino JL, Noordergraaf A**. Functional requirements of a mathematical model of the heart. *Conf Proc IEEE Eng Med Biol Soc* 2009: 4491-4494, 2009.

193. **Pan Q, Wang R, Reglin B, Cai G, Yan J, Pries AR, Ning G**. A one-dimensional mathematical model for studying the pulsatile flow in microvascular networks. *J Biomech Eng* 136: 011009, 2014.

194. **Parker JC, Guyton AC, Taylor AE**. Pulmonary interstitial and capillary pressures estimated from intra-alveolar fluid pressures. *J Appl Physiol Respir Environ Exerc Physiol* 44: 267-276, 1978.

195. **Permutt S**. Effect of interstitial pressure of the lung on pulmonary circulation. *Med Thorac* 22: 118-131, 1965.

196. **Pirkle JC, Jr., Gann DS**. Restitution of blood volume after hemorrhage: mathematical description. *Am J Physiol* 228: 821-827, 1975.

197. **Platz E, Lattanzi A, Agbo C, Takeuchi M, Resnic FS, Solomon SD, Desai AS**. Utility of lung ultrasound in predicting pulmonary and cardiac pressures. *Eur J Heart Fail* 14: 1276-1284, 2012.

198. **Prewitt RM, McCarthy J, Wood LD**. Treatment of acute low pressure pulmonary edema in dogs: Relative effects of hydrostatic and oncotic pressure, nitroprusside, and positive end-expiratory pressure. *J Clin Invest* 67: 409-418, 1981.

199. **Price RJ, Skalak TC**. Circumferential wall stress as a mechanism for arteriolar rarefaction and proliferation in a network model. *Microvasc Res* 47: 188-202, 1994.

200. **Pries AR, Cornelissen AJ, Sloot AA, Hinkeldey M, Dreher MR, Hopfner M, Dewhirst MW, Secomb TW**. Structural adaptation and heterogeneity of normal and tumor microvascular networks. *PLoS Comput Biol* 5: e1000394, 2009.

201. **Pries AR, Secomb TW**. Microvascular blood viscosity in vivo and the endothelial surface layer. *Am J Physiol Heart Circ Physiol* 289: H2657-2664, 2005.

202. **Pries AR, Secomb TW**. Origins of heterogeneity in tissue perfusion and metabolism. *Cardiovasc Res* 81: 328-335, 2009.

203. **Pries AR, Secomb TW, Gaehtgens P**. Relationship between structural and hemodynamic heterogeneity in microvascular networks. *Am J Physiol* 270: H545-553, 1996.

204. **Pries AR, Secomb TW, Gaehtgens P**. Structural adaptation and stability of microvascular networks: Theory and simulations. *Am J Physiol* 275: H349-360, 1998.

205. **Pries AR, Secomb TW, Gaehtgens P**. Structural autoregulation of terminal vascular beds: Vascular adaptation and development of hypertension. *Hypertension* 33: 153-161, 1998.

206. **Pries AR, Secomb TW, Gessner T, Sperandio MB, Gross JF, Gaehtgens P**. Resistance to blood flow in microvessels in vivo. *Circ Res* 75: 904-915, 1994.

207. **Pruitt BA, Moncrief JA, Mason AD**. Efficacy of buffered saline as the sole replacement fluid following acute measured hemorrhage in man. *J Trauma* 7: 767-782, 1967.

208. **Punnoose L, Burkhoff D, Rich S, Horn EM**. Right ventricular assist device in end-stage pulmonary arterial hypertension: Insights from a computational model of the cardiovascular system. *Prog Cardiovasc Dis* 55: 234-243, 2012.

209. **Quick CM, Berger DS, Noordergraaf A**. Apparent arterial compliance. *Am J Physiol Heart Circ Physiol* 274: H1393-H1403, 1998.

210. **Quick CM, Venugopal AM, Gashev AA, Zawieja DC, Stewart RH**. Intrinsic pump-conduit behavior of lymphangions. *Am J Physiol Regul Integr Comp Physiol* 292: R1510-1518, 2007.

211. **Quick CM, Young WL, Leonard EF, Joshi S, Gao E, Hashimoto T**. Model of structural and functional adaptation of small conductance vessels to arterial hypotension. *Am J Physiol Heart Circ Physiol* 279: H1645-1653, 2000.

212. **Radovancevic B, Vrtovec B, de Kort E, Radovancevic R, Gregoric ID, Frazier OH**. End-organ function in patients on long-term circulatory support with continuous- or pulsatile-flow assist devices. *J Heart Lung Transplant* 26: 815-818, 2007.

213. **Raven PB, Chapleau MW**. Blood pressure regulation XI: Overview and future research directions. *Eur J Appl Physiol* 114: 579-586, 2014.

214. **Reddi B**. Venous excess: A new approach to cardiovascular control and its teaching. *J Appl Physiol* 98: 356-364, 2004.

215. **Redfield MM, Jacobsen SJ, Burnett JC, Jr., Mahoney DW, Bailey KR, Rodeheffer RJ**. Burden of systolic and diastolic ventricular dysfunction in the community: Appreciating the scope of the heart failure epidemic. *JAMA* 289: 194-202, 2003.

216. **Reisner AT, Heldt T**. A computational model of hemorrhage and dehydration suggests a pathophysiological mechanism: Starling-mediated protein trapping. *Am J Physiol Heart Circ Physiol* 304: H620-631, 2013.

217. **Reneman RS, Arts T, Hoeks AP**. Wall shear stress–an important determinant of endothelial cell function and structure–in the arterial system in vivo. *J Vasc Res* 2006.

218. **Resnick N, Yahav H, Shay-Salit A, Shushy M, Schubert S, Zilberman LC, Wofovitz E**. Fluid shear stress and the vascular endothelium: for better and for worse. *Prog Biophys Mol Biol* 81: 177-199, 2003.

219. **Roger VL, Weston SA, Redfield MM, Hellermann-Homan JP, Killian J, Yawn BP, Jacobsen SJ**. Trends in heart failure incidence and survival in a community-based population. *JAMA* 292: 344-350, 2004.

220. **Roselli RJ, Tack G, Harris TR**. A model of fluid, erythrocyte, and solute transport in the lung. *Ann Biomed Eng* 25: 46-61, 1997.

221. **Rothe CF**. Reflex control of veins and vascular capacitance. *Physiol Rev* 63: 1281-1342, 1983.

222. **Rothe CF**. Physiology of venous return. An unappreciated boost to the heart. *Arch Intern Med* 146: 977-982, 1986.

223. **Rothe CF**. Mean circulatory filling pressure: Its meaning and measurement. *J Appl Physiol* 74: 499-509, 1993.

224. **Rothe CF, Gersting JM**. Cardiovascular interactions: An interactive tutorial and mathematical model. *Adv Physiol Educ* 26: 98-109, 2002.

225. **Safar ME, Lacolley P**. Disturbance of macro- and microcirculation: Relations with pulse pressure and cardiac organ damage. *Am J Physiol Heart Circ Physiol* 293: H1-7, 2007.

226. **Salotto AG, Muscarella LF, Melbin J, Li JK, Noordergraaf A**. Pressure pulse transmission into vascular beds. *Microvasc Res* 32: 152-163, 1986.

227. **Sansone F, Zingarelli E, Flocco R, Dato GMA, Parisi F, Punta G, Forsennati PG, Bardi GL, del Ponte S, Patanè F, Casabona R**. Pulsed or continuous flow in long-term assist devices: A debated topic. *Transplant Rev (Orlando)* 26: 241-245, 2012.

228. **Scallan J, Huxley V, Korthuis R**. *Capillary Fluid Exchange: Regulation, Functions, and Pathology*. San Rafael, CA: Morgan & Claypool Life Sciences, 2010.

229. **Schmid-Schonbein GW**. Microlymphatics and lymph flow. *Physiol Rev* 70: 987-1028, 1990.

230. **Schwartzenberg S, Redfield MM, From AM, Sorajja P, Nishimura RA, Borlaug BA**. Effects of vasodilation in heart failure with preserved or reduced ejection fraction implications of distinct pathophysiologies on response to therapy. *J Am Coll Cardiol* 59: 442-451, 2012.

231. **Scott MC, Winters ME**. Congestive heart failure. *Emerg Med Clin North Am* 33: 553-562, 2015.

232. **Secomb TW, Beard Da, Frisbee JC, Smith NP, Pries AR**. The role of theoretical modeling in microcirculation research. *Microcirculation* 15: 693-698, 2008.

233. **Seki J**. Flow pulsation and network structure in mesenteric microvasculature of rats. *Am J Physiol* 266: H811-821, 1994.

234. **Sezai A, Shiono M, Orime Y, Nakata K, Hata M, Iida M, Kashiwazaki S, Kinoshita J, Nemoto M, Koujima T, Furuichi M, Eda K, Hirose H, Yoshino T, Saitoh A, Taniguchi Y, Sezai Y**. Major organ function under mechanical support: Comparative studies of pulsatile and nonpulsatile circulation. *Artif Organs* 23: 280-285, 1999.

235. **Sezai A, Shiono M, Orime Y, Nakata K, Hata M, Nemoto M, Saitoh T, Sezai Y**. Comparison studies of major organ microcirculations under pulsatile- and nonpulsatile-assisted circulations. *Artif Organs* 20: 139-142, 1996.

236. **Shafer I, Nancollas R, Boes M, Sieminski AL, Geddes JB**. Stability of a microvessel subject to structural adaptation of diameter and wall thickness. *Math Med Biol* 28: 271-286, 2011.

237. **Shim EB, Sah JY, Youn CH**. Mathematical modeling of cardiovascular system dynamics using a lumped parameter method. *Jpn J Physiol* 54: 545-553, 2004.

238. **Shishido T, Hayashi K, Shigemi K, Sato T, Sugimachi M, Sunagawa K**. Single-beat estimation of end-systolic elastance using bilinearly approximated time-varying elastance curve. *Circulation* 102: 1983-1989, 2000.

239. **Skalak TC, Price RJ**. The role of mechanical stresses in microvascular remodeling. *Microcirculation* 3: 143-165, 1996.

240. **Smaje LH, Fraser PA, Clough G**. The distensibility of single capillaries and venules in the cat mesentery. *Microvasc Res* 20: 358-370, 1980.

241. **Smith B, Geoffrey Chase J, Shaw G, Nokes R**. Experimentally verified minimal cardiovascular system model for rapid diagnostic assistance. *Control Eng Pract* 13: 1183-1193, 2005.

242. **Smith BW, Chase JG, Nokes RI, Shaw GM, Wake G**. Minimal haemodynamic system model including ventricular interaction and valve dynamics. *Med Eng Phys* 26: 131-139, 2004.

243. **Soucy KG, Koenig SC, Giridharan GA, Sobieski MA, Slaughter MS**. Defining pulsatility during continuous-flow ventricular assist device support. *J Heart Lung Transplant* 32: 581-587, 2013.

244. **Soucy KG, Koenig SC, Giridharan GA, Sobieski MA, Slaughter MS**. Rotary pumps and diminished pulsatility: Do we need a pulse? *ASAIO J* 59: 355-366, 2013.

245. **Starfinger C, Chase J, Hann C, Shaw G, Lambermont B, Ghuysen A, Kolh P, Dauby P, Desaive T**. Model-based identification and diagnosis of a porcine model of induced endotoxic shock with hemofiltration. *Math Biosci* 216: 132-139, 2008.

246. **Starling EH**. *The Linacre lecture on the law of the heart: Given at Cambridge, 1915*. London, UK: Longmans, Green and Co., 1918.

247. **Starling MR, Walsh RA, Dell'Italia LJ, Mancini GB, Lasher JC, Lancaster JL**. The relationship of various measures of end-systole to left ventricular maximum time-varying elastance in man. *Circulation* 76: 32-43, 1987.

248. **Staub C, Taylor AE**. *Edema*. New York, NY: Raven Press Books, Ltd., 1984.

249. **Stein L, Beraud JJ, Morissette M, Luz PD, Weil MH, Shubin H**. Pulmonary edema during volume infusion. *Circulation* 52: 483-489, 1975.

250. **Steinberg BA, Zhao X, Heidenreich PA, Peterson ED, Bhatt DL, Cannon CP, Hernandez AF, Fonarow GC**. Trends in patients hospitalized with heart failure and preserved left ventricular ejection fraction: Prevalence, therapies, and outcomes. *Circulation* 126: 65-75, 2012.

251. **Stepp DW, Nishikawa Y, Chilian WM**. Regulation of shear stress in the canine coronary microcirculation. *Circulation* 100: 1555-1561, 1999.

252. **Stergiopulos N, Meister JJ, Westerhof N**. Evaluation of methods for estimation of total arterial compliance. *Am J Physiol* 268: H1540-1548, 1995.

253. **Stewart RH, Geissler HJ, Allen SJ, Laine GA**. Protein washdown as a defense mechanism against myocardial edema. *Am J Physiol Heart Circ Physiol* 279: 1864-1868, 2000.

254. **Suga H, Sagawa K**. Mathematical interrelationship between instantaneous ventricular pressure-volume ratio and myocardial force-velocity relation. *Ann Biomed Eng* 1: 160-181, 1972.

255. **Sugimachi M, Sunagawa K, Uemura K, Kamiya A, Shimizu S, Inagaki M, Shishido T**. Estimated venous return surface and cardiac output curve precisely predicts new hemodynamics after volume change. *Conf Proc IEEE Eng Med Biol Soc* C: 5205-5208, 2010.

256. **Sunagawa K, Sagawa K, Maughan WL**. Ventricular interaction with the loading system. *Ann Biomed Eng* 12: 163-189, 1984.

257. **Sunagawa K, Sagawa K, Maughan WL**. Ventricular interaction with the vascular system in terms of pressure-volume relationships. In: *Ventricular/Vascular Coupling*, edited by Yin FC. New York, NY: Springer New York, 1987, p. 210-239.

258. **Tachibana H, Cheng HJ, Ukai T, Igawa A, Zhang ZS, Little WC, Cheng CP**. Levosimendan improves LV systolic and diastolic performance at rest and during exercise after heart failure. *Am J Physiol Heart Circ Physiol* 288: H914-922, 2005.

259. **Tavill AS**. Protein-losing enteropathy. *J Clin Path* 24: 45-54, 1971.

260. **Taylor AE, Parker JC, Kvietys PR, Perry MA**. The pulmonary interstitium in capillary exchange. *Ann N Y Acad Sci* 384: 146-165, 1982.

261. **Thalmann M, Schima H, Wieselthaler G, Wolner E**. Physiology of continuous blood flow in recipients of rotary cardiac assist devices. *J Heart Lung Transplant* 24: 237-245, 2005.

262. **Thorneloe KS, Cheung M, Bao W, Alsaid H, Lenhard S, Jian MY, Costell M, Maniscalco-Hauk K, Krawiec JA, Olzinski A, Gordon E, Lozinskaya I, Elefante L, Qin P, Matasic DS, James C, Tunstead J, Donovan B, Kallal L, Waszkiewicz A, Vaidya K, Davenport EA, Larkin J, Burgert M, Casillas LN, Marquis RW, Ye G, Eidam HS, Goodman KB, Toomey JR, Roethke TJ, Jucker BM, Schnackenberg CG, Townsley MI, Lepore JJ, Willette RN**. An orally active TRPV4 channel blocker prevents and resolves pulmonary edema induced by heart failure. *Sci Transl Med* 4: 159ra148, 2012.

263. **Tominaga R, Smith W, Massiello A, Harasaki H, Golding LA**. Chronic nonpulsatile blood flow. III. Effects of pump flow rate on oxygen transport and utilization in chronic nonpulsatile biventricular bypass. *J Thorac Cardiovasc Surg* 111: 863-872, 1996.

264. **Townsley MI, Fu Z, Mathieu-Costello O, West JB**. Pulmonary microvascular permeability. Responses to high vascular pressure after induction of pacing-induced heart failure in dogs. *Circ Res* 77: 317-325, 1995.

265. **Townsley MI, Pitts VH, Ardell JL, Zhao Z, Johnson WH, Jr.** Altered pulmonary microvascular reactivity to norepinephrine in canine pacing-induced heart failure. *Circ Res* 75: 347-356, 1994.

266. **Townsley MI, Snell KS, Ivey CL, Culberson DE, Liu DC, Reed RK, Mathieu-Costello O**. Remodeling of lung interstitium but not resistance vessels in canine pacing-induced heart failure. *J Appl Physiol* 87: 1823-1830, 1999.

267. **Tsuruta H, Sato T, Shirataka M, Ikeda N**. Mathematical model of cardiovascular mechanics for diagnostic analysis and treatment of heart failure: Part 1. Model description and theoretical analysis. *Med Biol Eng Comput* 32: 3-11, 1994.

268. **Tuzun E, Chorpenning K, Liu MQ, Bonugli K, Tamez D, Lenox M, Miller MW, Fossum TW**. The effects of continuous and intermittent reduced speed modes on renal and intestinal perfusion in an ovine model. *ASAIO J* 60: 19-24, 2014.

269. **Uemura K, Sugimachi M, Kawada T, Kamiya A, Jin Y, Kashihara K, Sunagawa K**. A novel framework of circulatory equilibrium. *Am J Physiol Heart Circ Physiol* 286: H2376-H2385, 2004.

270. **Ursino M**. Interaction between carotid baroregulation and the pulsating heart: A mathematical model. *Am J Physiol* 275: H1733-1747, 1998.

271. **Ursino M, Antonucci M, Belardinelli E**. Role of active changes in venous capacity by the carotid baroreflex: Analysis with a mathematical model. *Am J Physiol* 267: H2531-2546, 1994.

272. **Ursino M, Colantuoni A, Bertuglia S**. Vasomotion and blood flow regulation in hamster skeletal muscle microcirculation: A theoretical and experimental study. *Microvasc Res* 56: 233-252, 1998.

273. **Valparaiso AP, Vicente D, Bograd B, Elster E, Davis T**. Modeling acute traumatic injury. *J Surg Res* 194: 220-232, 2015.

274. **van der Worp HB, Howells DW, Sena ES, Porritt MJ, Rewell S, O'Collins V, Macleod MR**. Can animal models of disease reliably inform human studies? *PLoS Med* 7: e1000245, 2010.

275. **Van Gieson EJ, Murfee WL, Skalak TC, Price RJ**. Enhanced smooth muscle cell coverage of microvessels exposed to increased hemodynamic stresses in vivo. *Circ Res* 92: 929-936, 2003.

276. **Vanlier J, Tiemann Ca, Hilbers PaJ, van Riel NaW**. Parameter uncertainty in biochemical models described by ordinary differential equations. *Math Biosci* 246: 305-314, 2013.

277. **Varon J, Acosta P**. *Handbook of Critical and Intensive Care Medicine*. Houston, TX: Springer, 2010.

278. **Versprille A, Jansen JRC, Drop A, Hulsmann AR**. Mean systemic filling pressure as a characteristic pressure for venous return. *Pflugers Arch* 405: 226-233, 1985.

279. **Volpicelli G, Skurzak S, Boero E, Carpinteri G, Tengattini M, Stefanone V, Luberto L, Anile A, Cerutti E, Radeschi G, Frascisco MF**. Lung ultrasound predicts well extravascular lung water but is of limited usefulness in the prediction of wedge pressure. *Anesthesiology* 121: 320-327, 2014.

280. **Voss B, Krane M, Jung C, Brockmann G, Braun S, Gunther T, Lange R, Bauernschmitt R**. Cardiopulmonary bypass with physiological flow and pressure curves: Pulse is unnecessary! *Eur J Cardiothorac Surg* 37: 223-232, 2010.

281. **Wallace CR, Hamilton WF**. Study of spontaneous congestive heart failure in the dog. *Circ Res* XI: 301-315, 1968.

282. **Webster L**. Colloid osmotic pressure: Theoretical aspects and background. *Clin Perinatol* 9: 505-521, 1982.

283. **Weil MH, Henning RJ, Morissette M, Michaels S**. Relationship between colloid osmotic pressure and pulmonary artery wedge pressure in patients with acute cardiorespiratory failiure. *Am J Med* 64: 643-650, 1978.

284. **West JB**. Influence of hydrostatic pressure on the pulmonary circulation. *Jpn Heart J* 7: 350-368, 1966.

285. **Westerhof N, Bosman F, De Vries CJ, Noordergraaf A**. Analog studies of the human systemic arterial tree. *J Biomech* 2: 121-143, 1969.

286. **Westerhof N, Lankhaar JW, Westerhof BE**. The arterial windkessel. *Med Biol Eng Comput* 47: 131-141, 2009.

287. **Westerhof N, Stergiopulos N, Noble MIM**. Comparative Physiology. In: *Snapshots of Hemodynamics*. Boston, MA: Springer US, 2005, p. 155-160.

288. **Whyte JJ, Laughlin MH**. The effects of acute and chronic exercise on the vasculature. *Acta Physiol (Oxf)* 199: 441-450, 2010.

289. **Wiig H, Swartz MA**. Interstitial fluid and lymph formation and transport: Physiological regulation and roles in inflammation and cancer. *Physiol Rev* 92: 1005-1060, 2012.

290. **Wilson JR, Douglas P, Hickey WF, Lanoce V, Ferraro N, Muhammad A, Reichek N**. Experimental congestive heart failure produced by rapid ventricular pacing in the dog: Cardiac effects. *Circulation* 75: 857-867, 1987.

291. **Witte MH, Dumont AE, Clauss RH, Rader B, Levine N, Breed ES**. Lymph circulation in congestive heart failure: Effect of external thoracic duct drainage. *Circulation* 39: 723-733, 1969.

292. **Womersley JR**. Oscillatory flow in arteries: The constrained elastic tube as a model of arterial flow and pulse transmission. *Phys Med Biol* 2: 178-187, 1957.

293. **Yee A, Bosworth KA, Conway DE, Eskin SG, McIntire LV**. Gene expression of endothelial cells under pulsatile non-reversing vs steady shear stress; Comparison of nitric oxide production. *Ann Biomed Eng* 36: 571-579, 2008.

294. **Yildiran T, Koc M, Bozkurt A, Sahin DY, Unal I, Acarturk E**. Low pulse pressure as a predictor of death in patients with mild to advanced heart failure. *Tex Heart Inst J* 37: 284-290, 2010.

295. **Yin Z, Wang Z, Zhu H, Zhang R, Wang H, Li X**. Experimental study of effect of Fontan circuit on pulmonary microcirculation. *Asian Cardiovasc Thorac Ann* 14: 183-188, 2006.

296. **Young JF, Luecke RH, Pearce BA, Lee T, Ahn H, Baek S, Moon H, Dye DW, Davis TM, Taylor SJ**. Human organ/tissue growth algorithms that include obese individuals and black/white population organ weight similarities from autopsy data. *J Toxicol Environ Health A* 72: 527-540, 2009.

297. **Younis BA, Berger SA**. A turbulence model for pulsatile arterial flows. *J Biomech Eng* 126: 578-578, 2004.

298. **Zamir M**. *The Physics of Pulsatile Flow*. New York, NY: Springer, 2000.

299. **Zheng X, Xie C**. A viscoelastic model of blood capillary extension and regression: Derivation, analysis, and simulation. *J Math Biol* 68: 57-80, 2014.

300. **Zoccali C, Torino C, Tripepi R, Tripepi G, D'Arrigo G, Postorino M, Gargani L, Sicari R, Picano E, Mallamaci F**. Pulmonary congestion predicts cardiac events and mortality in ESRD. *J Am Soc Nephrol* 24: 639-646, 2013.

301. **Zocchi L**. Physiology and pathophysiology of pleural fluid turnover. *Eur Respir J* 20: 1545-1558, 2002.

302. **Zongtao Y, Huishan W, Zengwei W, Hongyu Z, Minhua F, Xinmin L, Nanbin Z, Hongguang H**. Experimental study of nonpulsatile flow perfusion and structural remodeling of pulmonary microcirculation vessels. *Thorac Cardiovasc Surg* 58: 468-472, 2010.

303. **Zweifach BW**. Quantitative studies of microcirculatory structure and function. II. Direct measurement of capillary pressure in splanchnic mesenteric vessels. *Circ Res* 34: 858-866, 1974.

APPENDIX A

The minimal closed-loop model illustrated in Fig. 2 is characterized by the standard equations characterizing peripheral resistances, cardiac ventricles, and vascular compartments of the systemic and pulmonary systems (*Eqs. A1-A13*). Model equations are all linear functions, illustrated graphically in Fig. 1.

Systemic		**Pulmonary**		**Component**
(*A1*)	$VR = (P_{sa} - P_{sv})/R_s$	(*A2*)	$CO = (P_{pa} - P_{pv})/R_p$	**Peripheral Resistances**
(*A3*)	$P_{eslv} = E_{maxlv}(V_{oeslv} - V_{oeslv})$	(*A4*)	$P_{esrv} = E_{maxrv}(V_{oesrv} - V_{oesrv})$	**Cardiac Ventricles**
(*A5*)	$P_{edlv} = E_{minlv}(V_{edlv} - V_{oedlv})$	(*A6*)	$P_{edrv} = E_{minrv}(V_{edrv} - V_{oedrv})$	
(*A7*)	$CO = HR(V_{eslv} - V_{edlv})$	(*A8*)	$CO = HR(V_{esrv} - V_{edrv})$	
(*A9*)	$V_{sa} = V_{osa} + C_{sa}P_{sa}$	(*A10*)	$V_{pa} = V_{opa} + C_{pa}P_{pa}$	**Vascular Compart-ments**
(*A11*)	$V_{sv} = V_{osv} + C_{sv}P_{sv}$	(*A12*)	$V_{pv} = V_{opv} + C_{pv}P_{pv}$	
(*A13*)	$V_B = V_{sa} + V_{sv} + V_{pa} + V_{pv}$			
(*A14*)	$P_{eslv} = \kappa P_{sa} \cong P_{sa}$	(*A15*)	$P_{esrv} = \kappa P_{pa} \cong P_{pa}$	**Approx-imations**
(*A16*)	$P_{edlv} \cong P_{pv}$	(*A17*)	$P_{edrv} \cong P_{sv}$	

Equations A14-A17 represent common approximations. The parameter α is an assumed constant, representing the ratio of P_{es} to P_{sa} (256),

$$\kappa = \frac{E_a}{R_s\, HR}, \qquad (A18)$$

where E_a is the "effective arterial elastance". E_a has been approximated by R_sHR (256), and thus κ=1. For simplifying presentation of results, κ is assumed to have the value 1 in

the present work. Simultanously solving *Eqs. A1-A17* for *CO*, P_{sv}, P_{pa}, P_{pv} and V_B yields equilibrium values CO^*, P_{sv}^*, P_{pa}^*, P_{pv}^* and V_B^*.

$$CO^* = \frac{HR\left(E_{minlv}\Delta V_{olv}+E_{maxrv}\Delta V_{orv}+P_{sa}\left(\frac{E_{maxrv}}{E_{minrv}}-\frac{E_{minlv}}{E_{maxlv}}\right)\right)}{E_{minlv}+E_{maxlv}+R_pHR+\frac{E_{maxrv}HR\,R_S}{E_{minrv}}} \tag{A19}$$

$$P_{sv}^* = \frac{P_{sa}\left(E_{maxrv}+E_{minlv}+HR\,R_p-\frac{HR\,R_SE_{minlv}}{E_{maxlv}}\right)+HRR_S(E_{minlv}\Delta V_{olv}+E_{maxrv}\Delta V_{orv})}{E_{minlv}+E_{maxlv}+R_pHR+\frac{E_{maxrv}HR\,R_S}{E_{minrv}}} \tag{A20}$$

$$P_{pa}^* =$$

$$\frac{\Delta V_{orv}\left(E_{minlv}+R_pHR\right)-E_{minlv}\Delta V_{olv}\left(1+\frac{R_SHR}{E_{minrv}}\right)+P_{sa}\left(\frac{E_{minlv}}{E_{maxlv}}+\frac{E_{minlv}+HR\,R_p}{E_{minrv}}+\frac{E_{maxrv}HR\,R_S}{E_{maxlv}E_{minrv}}\right)}{E_{minlv}+E_{maxlv}+R_pHR+\frac{E_{maxrv}HR\,R_S}{E_{minrv}}} \tag{A21}$$

$$P_{pv}^* = \frac{E_{minlv}\left(\begin{matrix}E_{maxrv}\Delta V_{orv}+\frac{P_{sa}}{E_{maxlv}}\left(\frac{E_{maxrv}}{E_{minrv}}(E_{maxlv}+E_{minrv}+R_SHR)+R_pHR\right)\\ -\Delta V_{olv}\left(R_pHR+E_{maxrv}\left(1+\frac{R_SHR}{E_{minrv}}\right)\right)\end{matrix}\right)}{E_{minlv}+E_{maxlv}+R_pHR+\frac{E_{maxrv}HR\,R_S}{E_{minrv}}} \tag{A22}$$

$$V_B^* =$$

$$\frac{\left[\begin{matrix}E_{maxrv}\Delta V_{orv}\left(C_{pv}E_{minlv}+C_{pa}\left(E_{minlv}+R_pHR\right)-C_{sv}R_SHR\right)+V_{otot}\left(E_{minlv}+R_pHR+\frac{E_{maxrv}\left(E_{minrv}+R_SHR\right)}{E_{minrv}}\right)\\ -E_{minlv}\Delta V_{olv}\left(C_{sv}R_SHR-C_{pa}\left(1+\frac{R_SHR}{E_{minrv}}\right)-C_{pv}\left(R_pHR+E_{maxrv}\left(1+\frac{R_SHR}{E_{minrv}}\right)\right)\right)\\ +P_{sa}\left(\begin{matrix}\left(C_{sv}+C_{sa}\right)\left(E_{maxrv}+E_{minlv}+R_pHR\right)+\frac{C_{sv}E_{minlv}R_SHR}{E_{maxlv}}+\frac{C_{pv}E_{maxrv}R_SHR}{E_{minrv}}\\ +C_{pa}E_{maxrv}\left(\frac{E_{minlv}}{E_{maxlv}}+\frac{E_{minlv}+HR\,R_p}{E_{minrv}}+\frac{E_{minlv}HR\,R_S}{E_{maxlv}E_{minrv}}\right)+\\ C_{pv}E_{minlv}\left(\frac{E_{maxrv}}{E_{minrv}}+\frac{E_{maxrv}+HR\,R_p}{E_{maxlv}}+\frac{E_{maxrv}HR\,R_S}{E_{maxlv}E_{minrv}}\right)\end{matrix}\right)\end{matrix}\right]}{E_{minlv}+E_{maxlv}+R_pHR+\frac{E_{maxrv}HR\,R_S}{E_{minrv}}} \tag{A23}$$

APPENDIX B

Although mathematical models have characterized the ventricular end-diastolic pressure-volume relationship with a linear function (100, 256), as in *Eq. A5*, the end-diastolic pressure (P_{ed}) is typically represented as an exponential function of end diastolic volume (V_{ed}),

$$P_{ed} = \alpha V_{ed}^{\beta}, \qquad (B1)$$

Empirical parameters α and β were determined from measured ventricular pressure-volume relationships. Figure 5A illustrates a nonlinear end-diastolic pressure-volume relationship (dashed curve) for healthy subjects (121). To reduce the error associated with approximating *Eq. B1* with a single line, it can be approximated by two contiguous lines. In this case, the slope (E_{min}) and intercept (V_{oed}) are assigned different values, depending on whether the ventricular filling volume is large or small. For the present work, P_{ed} was explicitly related to parameters E_{min1} and V_{oed1} when V_{ed} is less than some volume $V,'$and E_{min2} and V_{oed2} when V_{ed} is greater than or equal to $V.'$

$$P_{ed} = \begin{cases} E_{min1}(V_{ed} - V_{oed1}), & V_{ed} < V' \\ E_{min2}(V_{ed} - V_{oed2}), & V_{ed} \geq V' \end{cases} \qquad (B2)$$

Equation B2 thus is a "piecewise linear" representation of *Eq. B1* (solid lines, Fig. 5A). The result of describing the end-diastolic pressure-volume relationship as piecewise linear is to cause the cardiac function curve to plateau at higher ventricular filling pressures (Fig. 5B). For Figs. 3-5, specific parameter values for E_{min1}, E_{min2}, V_{oed1} and V_{oed2} had to be determined for each ventricle. Values for left ventricle α and β have been

reported for normal subjects (121) and well as for HFrEF and HFpEF conditions (57). For the right ventricle, α and β were calculated according to the validated method described in Klotz et al. (121) based on reported values (208) to maintain consistency with the left ventricle, and were assumed unchanged in heart failure phenotypes. In each case, the values of parameters were found by minimizing the error between *Eq. B1* and *Eq. B2* using the Nelder-Mead simplex algorithm in MatLab™. Parameters were fit over the range of end-diastolic volumes 0-160 mL, 0-160 mL, and 0-250 mL, which allowed for typical end-diastolic pressures for the normal, HFpEF, and HFrEF phenotypes, respectively. Resulting parameter values are listed in Table 1.

APPENDIX C

The lumped model illustrated in Fig. 6 is characterized by the standard equations describing peripheral resistances, cardiac ventricles, and vascular compartments of the systemic and pulmonary systems (*Eqs. C1-C10*) as well as standard equations describing the pulmonary interstitium (*Eqs. C11-C15*). Model equations are linear functions, illustrated graphically in Fig. 6. Parameter values are defined in Table D1.

Systemic		***Pulmonary***		***Component***
		(*C1*)	$Q = (P_{pa} - P_{cp})/R_{pa}$	***Peripheral Resistances***
(*C2*)	$Q = (P_{sa} - P_{sv})/R_s$	(*C3*)	$Q = (P_{cp} - P_{pv})/R_{pv}$	
(*C4*)	$V_{sa} = V_{osa} + C_{sa}P_{sa}$	(*C5*)	$V_{pa} = V_{opa} + C_{pa}P_{pa}$	***Vascular Compart.***
(*C6*)	$V_{sv} = V_{osv} + C_{sv}P_{sv}$	(*C7*)	$V_{pv} = V_{opv} + C_{pv}P_{pv}$	
(*C8*)	$Q = \frac{HRP_{pv}}{E_{minlv}} - \frac{HRP_{sa}}{E_{maxlv}} + \Delta V_{olv}HR$	(*C9*)	$Q = \frac{HRP_{sv}}{E_{minrv}} - \frac{HRP_{pa}}{E_{maxrv}} + \Delta V_{orv}HR$	***Cardiac Ventricles***
(*C10*)	$V_B = V_{sa} + V_{sv} + V_{pa} + V_{pv}$			***Conservation of mass***
(*C11*)	$V = V_B + V_{ip}$			
		(*C12*)	$Q_{lp} = \frac{P_{ip} + P_{pp} - P_{sv}}{R_{lp}}$	***Interstitial Flow***
		(*C13*)	$Q_{mp} = K_{fp}[(P_{cp} - P_{ip}) - \propto \sigma(C_{cp} - C_{ip})]$	
		(*C14*)	$Q_{ip} = Q_{mp} = Q_{lp}$	
		(*C15*)	$V_{ip} = P_{ip}C_p + V_{op}$	***Interstitial Compart.***

APPENDIX D

Estimation of oncotic pressures. Parameters were found for both a 20 kg canine and 70 kg human for each of the heart failure and normal conditions from multiple previously published models. The pulmonary osmotic pressure difference across the blood and interstitial spaces ($\Delta\Pi_p$) for all conditions was calculated according to Dongaonkar et. al. (49), assuming,

$$\Delta\Pi_p = \nu\sigma(C_{cp} - C_{ip}), \qquad (D1)$$

where σ is the pulmonary reflection coefficient and ν as an experimentally derived parameter allowing expression of pulmonary colloid osmotic pressure as protein concentration between the capillaries and interstitium (C_{cp}, C_{ip}, respectively).

Piecewise linear relationship. Although many of our chosen parameters may vary with pressures and volumes (179), for the purposes of our model, they are assumed to be constant. However, pulmonary interstitial compliance (49) and end-diastolic ventricular elastance (E_{minlv}, E_{minrv}) are reported to be particularly sensitive to changes in volume. Therefore, the piecewise linear relationship for pulmonary interstitial compliance (194) and end-diastolic ventricular elastance (*Appendix B*) as reported in the previous models was applied to our model.

Canine parameter set. Parameter values for characterizing the vascular compartments for the normal condition were obtained from Beyar et al. (19, 20). Parameter values for the interstitial compartment were obtained from Dongaonkar et al. (49). For the HFrEF condition, parameters values were obtained from Tsuruta (267).

Because interstitial parameters are commonly reported per 100g of tissue weight, parameters for the canine interstitial compartment were converted to standard SI units by assuming a weight of 146 g for the lungs (110) according to the method described in detail by Gyenge (91). Because limited data exits, interstitial lung parameters were in general assumed to be unchanged for HFrEF, which is supported by experimental studies (266). The microvascular filtration coefficient was assumed to have a fourfold decrease, following the average of measured studies (107, 264).

Human parameter set. Parameters for the vascular compartment were obtained from the model of the lumped vascular system (Table 1). Because inadequate parameter measurements of the interstitium in humans exist, interstitial parameters were in general assumed to be similar to measurements made in animal models. Parameters for the interstitial compartment were converted to standard SI units by assuming a weight of 1136 g for the lungs (296) as described in detail by Gyenge (91). However, values for R_{lp} and K_{fp} are poorly characterized, and a large variation in parameter values are reported among animal models (49). They were therefore calculated by assuming measured normal capillary pressure (P_{cp}) (48), systemic venous pressure (P_{sv}) (75), pulmonary interstitial pressure (P_{ip}) (248), and lymphatic flow (Q_{ip}) (291) through the interstitial compartment using *Eqs. C12* and *C13*. Values obtained for these parameters were found to be within reported ranges from animal models. Vascular parameter values for heart failure were obtained from Table 1 for heart failure preserved ejection fraction (HFpEF) and heart failure reduced ejection fraction (HFrEF). The microvascular filtration

coefficient was assumed to have a fourfold decrease, following the average of measured studies (107, 264).

Non-dimensional Terms	Para-meters	Canine		Human		
		Normal (19, 21, 49, 194)	**HFrEF** (19, 21, 49, 194, 258)	**Normal** (49) (Table 1)	**HFpEF** (49) (Table 1)	**HFrEF** (49) (Table 1)
J_{pn}	$\frac{P_{pp}}{P_{sa}}$	0.20	0.21	0.18	0.19	0.23
R_i	$K_{fp}R_{lp}$	11.2	2.80	0.93	0.23	0.23
Δo_{pn}	$\frac{\Delta o\Pi_p}{P_{sa}}$	-0.05	-0.34	-0.07	-0.06	-0.07
C_{pn}	$\frac{C_p}{C_{tot}}$	0.49 (l) 6.50 (h)	0.49 (l) 6.50 (h)	0.29 (l) 3.95 (h)	0.29 (l) 3.95 (h)	0.29 (l) 3.95 (h)
EE_{lv}	$\frac{E_{maxlv}}{E_{minlv}}$	56.34 (l) 4.14 (h)	2.20 (l) 1.53 (h)	25 (l) 0.31 (h)	5.68 (l) 0.31 (h)	8.26 (l) 0.41 (h)
E_{alv}	$\frac{R_sHR}{E_{maxlv}}$	0.74	2.26	0.82	0.83	1.99
Q_{ol}	$\frac{R_sHR\Delta V_{lv}}{P_{sa}}$	.44 (l) 1.3 (h)	0.79 (l) 1.95 (h)	0.47 (l) 2.68 (l)	0.63 (l) 3.7 (h)	1.17 (l) 4.12 (h)
EE_{rv}	$\frac{E_{maxrv}}{E_{minrv}}$	16.67 (l) 4.53 (h)	16.67 (l) 4.53 (h)	16.67 (l) 3.72 (h)	16.67 (l) 3.72 (h)	16.67 (l) 1.67 (h)
E_{arv}	$\frac{R_{pa}HR}{E_{maxrv}}$	0.50	0.89	0.115	0.41	0.25
Q_{or}	$\frac{R_{pa}HR\Delta V_{rv}}{P_{sa}}$	0.04 (l) 1.15 (h)	0.07 (l) 0.13 (h)	0.04 (l) 0.03 (h)	0.11 (l) 0.10 (h)	0.08 (l) 0.15 (h)
R_a	$\frac{R_{pa}}{R_s}$	0.11	0.11	0.08	0.16	0.14
R_v	$\frac{R_{pv}}{R_s}$	0.02	0.02	0.009	0.02	0.017
C_{san}	$\frac{C_{sa}}{C_{tot}}$	0.01	0.01	0.01	0.01	0.01
C_{svn}	$\frac{C_{sv}}{C_{tot}}$	0.80	0.80	0.62	0.62	0.62
C_{pan}	$\frac{C_{pa}}{C_{tot}}$	0.03	0.03	0.03	0.03	0.03
C_{pvn}	$\frac{C_{pv}}{C_{tot}}$	0.06	0.06	0.05	0.05	0.05

Table D1. Non-dimensionalized parameter values for the vascular and interstitial compartments were calculated from measured values.

APPENDIX E

Pulsatile pressures and flows were modeled using the one-dimensional periodic solution for the wave equation as described in detail in Westerhof et al. (285). Briefly, pressures and flows were modeled using the periodic solution to the Navier-Stokes equation for a thick-walled, linearly elastic vessel assuming Newtonian blood flow. Radial forces, rotational flows, body forces, and entrance phenomena were assumed to be negligible. The 1-D momentum balance then reduces as below,

$$-\frac{dP}{dz} = R'Q + L'\frac{dQ}{dt}. \quad (E1)$$

The transmural pressure (P) is related to the axial flow through resistance (R') and inertance (L') per unit length as a function of axial position z and time t. Conservation of mass requires that volume stored in vessel segment with compliance per unit length (C') vessel be equal to the reduction in flow (Q) along the vessel's axial position (285),

$$-\frac{dQ}{dz} = C'\frac{dP}{dt}. \quad (E2)$$

The values of L', R', C', are simple functions (285):

$$R = R'l = \frac{8\mu l}{\pi r^4}, \quad (E3)$$

$$C = C'l = \frac{dV}{dP} \approx \frac{3\pi r^2(r+h)^2 l}{Eh(2r+h)}, \quad (E4)$$

$$L = L'l = \frac{\rho l}{\pi r^2}. \quad (E5)$$

Resistance (R) is assumed to be a function of the dynamic viscosity of blood (μ), radius (r), and vessel length (l). Compliance (C) is the change in volume per change in inlet pressure, and can be approximated by r, l, wall thickness (h), and elastic modulus (E).

Inertance (L) is related to blood inertia, and is a function of r, l and blood density (ρ). Values of R, L and C are assumed to be constant over time, although in vivo slight variations occur with oscillating pressures.

To solve for pulsatile pressures ($\tilde{P}$) and flows ($\tilde{Q}$), inlet pressure is assumed to be periodic. Following standard practice for pulsatile hemodynamics, the inlet pressure to a vessel segment ($\tilde{P}_{in}$) can be represented by a simple oscillating function $\left|\tilde{P}_{in}\right|e^{i\omega t}$, with a magnitude $\left|\tilde{P}_{in}\right|$, time ($t$), and angular frequency (ω). The term i is equal to $\sqrt{-1}$. *Equations E1* and *E2* can be solved analytically to obtain solutions for pulsatile pressures ($\tilde{P}$) and flows ($\tilde{Q}$) in a vessel as a function of time (t), position (z), and angular frequency (ω) (16, 298),

$$\tilde{P}(t,z,\omega) = \left|\tilde{P}_{in}\right|e^{i\omega t}\left(P_f e^{-\frac{\omega z}{c_{ph}}} + P_b e^{\frac{\omega z}{c_{ph}}}\right), \quad (E6)$$

$$\tilde{Q}(t,z,\omega) = \left|\tilde{P}_{in}\right|e^{i\omega t}\frac{1}{Z_o}\left(P_f e^{-\frac{\omega z}{c_{ph}}} - P_b e^{\frac{\omega z}{c_{ph}}}\right), \quad (E7)$$

where Z_o is the characteristic impedance of the vessel, defined as,

$$Z_o = \frac{\sqrt{R+i\omega L}}{\sqrt{i\omega C}}, \quad (E8)$$

c_{ph} the phase velocity, defined as,

$$c_{ph} = \frac{i\omega l}{\sqrt{i\omega C(R+iwL)}}. \quad (E9)$$

P_f and P_b are the forward- and backward-travelling pressure waves in the vessel. Vessel input impedance (Z_{in}) can be calculated from *Eq. E6* and *Eq. E7* as,

$$Z_{in} = Z(0,\omega) = \frac{\tilde{P}(0,\omega)}{\tilde{Q}(0,\omega)}. \quad (E10)$$

The impedance at the vessel end of the vessel (i.e., $z=l$) is equal to the load impedance,

$$Z(l,\omega) = \frac{\tilde{P}(t,l,\omega)}{\tilde{Q}(t,l,\omega)} = Z_L, \tag{E11}$$

The input impedance of the vessel can be expressed as a function of impedance at vessel end (Z_L),

$$Z_{in} = Z(0,\omega) = \frac{\tilde{P}(t,z,\omega)}{\tilde{Q}(t,z,\omega)} = \frac{\cos\left[\frac{l\omega}{c_{ph}}\right] + i\frac{Z_o}{Z_L}\sin\left[\frac{l\omega}{c_{ph}}\right]}{Z_L\cos\left[\frac{l\omega}{c_{ph}}\right] + iZ_o\sin\left[\frac{l\omega}{c_{ph}}\right]}, \tag{E12}$$

Solutions for P_f and P_b in each vessel segment can be found by simultaneously solving *Eqs. E7, E8, E12* and *E13*. Assuming the term,

$$\Delta\tilde{P} = \left|\tilde{P}_{in}\right| e^{i\omega t}, \tag{E13}$$

is the total pressure difference across the vessel segment and a terminal load, as in Fig. 14C, the pressure drop across a single vessel ($\tilde{P}_{in} - \tilde{P}_{out}$) with a terminal load Z_L can be expressed as,

$$\tilde{P}_{in} - \tilde{P}_{out} = \tilde{P}(t,0,\omega) - \tilde{P}(t,l,\omega) = \Delta\tilde{P}\left(1 - \frac{Z_L}{Z_L\cosh\frac{R}{Z_o} + Z_o\sinh\frac{R}{Z_o}}\right). \tag{E14}$$

Pulsatile shear stress. By definition, the frictional force acting along a short segment of vessel, dz, is the wall shear stress, τ, multiplied by the surface area of the lumen, $2\pi rdz$. Typically, the frictional force along a segment of a vessel is expressed as the pressure drop, $R'Qdz$, multiplied by the cross-sectional area of the vessel, πr^2. Setting these two forces equal results in an equivalence, which is an alternative expression of Hagen-Poiseuille's Law,

$$R'Q = \tau\frac{2}{r}, \tag{E15}$$

Substituting *Eq. E15* into *Eq. E1* and solving for τ,

$$\tau = \left(\frac{dP}{dz} - L' \frac{dQ}{dt}\right)\frac{r}{2}. \qquad (E16)$$

Integrating down the length of a segment of vessel with inlet pressure ($\tilde{P}_{in}$) and outlet pressure ($\tilde{P}_{out}$) yields an expression for the average shear stress in vessel segment,

$$\tau = \left(\tilde{P}_{in} - \tilde{P}_{out}\right)\frac{r}{2l} - L' \frac{dQ}{dt}\frac{r}{2l}. \qquad (E17)$$

This formulation of shear stress includes the effect of blood inertia and in this case, P_{in} and P_{out} can be functions of time (i.e., oscillatory).

APPENDIX F

Mathematical models that characterize pulsatile hemodynamics in arterial networks must specify all boundary conditions, including the terminal ends of the smallest vessels in a bifurcating network. Although the downstream of terminal vessels could be assumed to have a constant pressure, much more realistic results can be obtained by assuming a load impedance (Z_L) as in Fig. 14B, that specifies a pressure-flow relationship. This load can be chosen to mimic the pressure-flow relationship formed by downstream vessels. Two forms of terminal loads have been commonly used (28, 109). One is purely resistive, (R_L), that represents the ratio of mean pressure to mean flow,

$$Z_L = R_L. \qquad (F1)$$

The other is a three-element Windkessel (68),

$$Z_L = Z_o + \frac{R_L}{1+i\omega R_L C_L}, \qquad (F2)$$

that is a function of characteristic impedance (Z_o), as well as a total downstream resistance and a compliance (C_L). To characterize the load formed by a microvascular network in a form that is amenable to algebraic manipulation, we developed a new terminal load, equal to a constant parameter (k) multiplied by the characteristic impedance of the first vessel in the network downstream,

$$Z_L = kZ_o = \frac{R_L}{\sqrt{i\omega R_L C_L}}. \qquad (F3)$$

To determine which form of Z_L best fit our network model, calculated input impedance at each level of the five-level bifurcating network (Table 5) assuming *Eqs. E3, E4, E11*

and *E12* was compared with the magnitude and phase of each of the loads. Parameter values for R_L, C_L, and Z_o were calculated from the bifurcating tree, with Z_o assumed to be the characteristic impedance of a vessel of level A. Input impedance magnitude and phase were found to be most similar to characteristic impedance (*Eq. F3*), especially at higher frequencies (Fig. F1), a finding supported by previous studies (67). *K* was determined by taking the magnitude of the ratio of input impedance to the characteristic impedance for the first 10 frequencies, and found to be .48, .50 and .49 for vessels of level A, B and C, respectively.

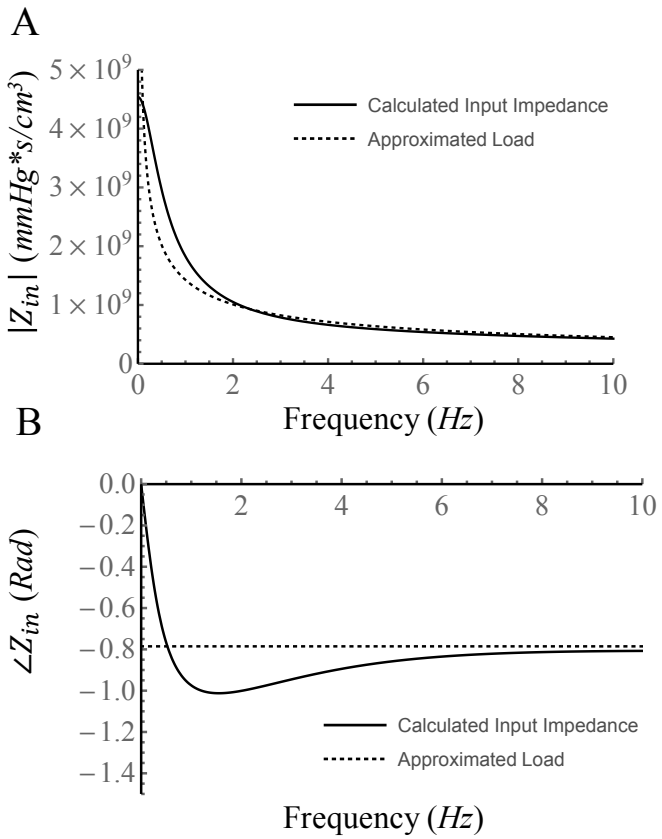

Figure F1. A) Input impedance magnitude ($|Z_{in}|$) of the five level fractal tree (Table 1) at level A closely matches the magnitude of vessel characteristic impedance multiplied by a constant (*Eq. F3*). B) Although approximated phase ($\angle Z_{in}$) varies slightly at lower frequencies, at heart rate and high frequencies it closely approximates calculated input impedance phase.

However, regardless of load chosen, $|\tilde{\tau}|$ behaves similarly in the microcirculation (Fig. B2). However, Eq. *F3* best reproduces the shear stress assuming *Eq. 45*.

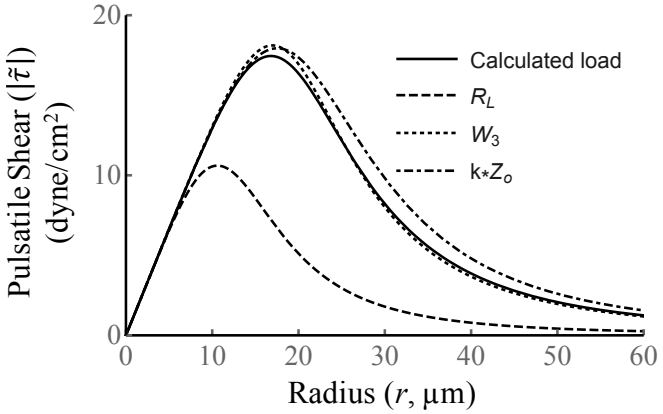

Figure F2. Pulsatile endothelial shear ($|\tilde{\tau}|$) in a single vessel terminated with a load impedance as in Fig. 1B behaves similarly regardless of terminating load, although with a purely resistive load, $|\tilde{\tau}|$ is much lower. The approximation of terminal load characterized by *Eq. F3* yields the most accurate representation.